



POLITECNICO DI TORINO
DIPARTIMENTO DI ELETTRONICA E TELECOMUNICAZIONI

Master of Science in Mechatronic Engineering

Master of Science Thesis

Modelling and development of an engine airpath coordinated control structure

Identification and control related to EGR and VGT actuation systems

Supervisors

Prof. Stefano Alberto Malan
Dr. Loris Ventura, Engineer

Candidate

Alessandro Veca
Student ID 296392

ACADEMIC YEAR 2022-2023

Abstract

Aim of this dissertation is the improvement of a benchmark standard airpath control logic, adopted on a 3-litre, four cylinders diesel engine, with a new control architecture, based on the gain scheduling control technique. Thesis work demonstrates the effectiveness of the control logic, highlighting the performance improvement that the exploitation of such schemes offers. Motivating purpose of the work lays behind the enforcement of stricter pollutant emissions requirements, along with the technological need for constantly developing more efficient solutions for the improvement of engine performance. The work is divided into three main steps.

- Identification of the mathematical models, representing the physical behaviour of the airpath.
- Development of a tailored gain scheduling control architecture, based on engine models obtained at previous step.
- Validation of the control results, refinement and comparison with benchmark experimental control logic.

These general procedures are applied to the Exhaust Gas Recirculation valve, also known as EGR, and to the Variable Geometry Turbocharger, referred to as VGT. Engine operating range, defined by engine rotation speed and load, is split into twenty subregions.

System identification is performed basing on simulated engine airpath plant, developed on GT-Power environment; inputs to the system are EGR and VGT actuators positions and outputs are air mass flow rate at intake manifold and boost pressure. SISO identifications are performed, one per each actuator and each subregion.

Adopted model families for identification purposes are ARX, ARMAX, OE and state-space (SS): among these, state-space models are selected as the most adequate to represent the plant. Gain scheduling control technique involves the development of several compensators of the same family, with coefficients that vary depending on engine map region.

Twelve out of twenty identified models are chosen so as to be the basis of the gain scheduling logic, with a view to avoiding repetitions. These models are referred to as Control Engine Operating Points, or CEOPs, and are screened basing on similarities between identified SS models. The design of the control logic is performed through PI compensators: one per each of the twelve CEOPs is designed, via an iterative gains tuning, both for the EGR and the VGT actuation logics. Discerning the most fitting controller in each engine operating situation is done via engine mapping: each engine current state is assigned to the most adequate controller model. Three assignment procedures are proposed and illustrated: *vicinity mapping*, *affinity mapping* and *k-means clustering*.

Concerning PI compensators, a range of anti-windup architectures is studied and compared, with a view to preventing saturation phenomena. Among these, *conditional integration* anti-windup scheme achieving faster desaturation response is equipped on both

the two controllers. Filters are applied to obtain a milder VGT action and to counteract sudden scheduled gain switches.

Testing is performed adopting different engine cycles, progressively spanning from calm to aggressive, and a fine tuning of the control parameters is performed. A thorough evaluation of the obtained control performances and a comparison with the benchmark standard control directly provided by the engine ECU manufacturer is done, highlighting the tracking improvement that is achieved via the designed control architecture. Controller design and validation is performed progressively enriching the operativity range of the control action, assessing its strength and limitations.

A gain scheduling controller, with feedforward actuations mapped values and injected fuel quantity derivative correction, equipped with *conditional integration* anti-windup architecture and actuation low-pass is eventually adopted, being the best one to address each presented control issue.

Future studies concerning the introduction of alternative control logics, as well as in-depth analyses on different engine mappings and choices of operating points are outlined throughout the work.

Acknowledgements

I have always believed that when you embark on a journey with the right people by your side, every effort turns into joy and every step becomes lighter. This thesis represents the last step of a beautiful path and the beginning of a new one. Therefore, I want to express my gratitude to those who have accompanied me so far, allowing me to appreciate the views, igniting my passion and lending a hand when I needed directions.

I would first of all thank Professor Malan and Loris Ventura, who have supported me through every detail, both technical and non-technical, of this work, with their kindness, patience and great expertise.

A sincere thanks goes to my friends and family members, for having always given me an advice and a smile throughout these years. I would particularly thank Antonio, for the many insightful suggestions he has given me, when I needed a hand, as well as for having shared with me this university path.

Eventually, I want express my gratitude to my parents, who have provided me with countless opportunities to learn, grow and become the person I am today. And thanks to my sister, Carlotta, who in spite of the challenges life has presented, is always there for me. Do never give up, as even when it rains incessantly, the sun will eventually shine again on the path.

Contents

| | |
|---|-----------|
| List of Tables | 9 |
| List of Figures | 10 |
| 1 Introduction | 17 |
| 1.1 Problem definition | 17 |
| 1.1.1 System identification | 18 |
| 1.1.2 Control logics overview | 18 |
| 1.1.3 Validation criteria | 19 |
| 1.2 Engine considered actuators | 19 |
| 1.2.1 The EGR | 19 |
| 1.2.2 The VGT | 20 |
| 1.3 Chapters synopsis | 21 |
| 2 The Internal Combustion Engine | 23 |
| 2.1 Technical specifications | 23 |
| 2.2 The exhaust gas recirculation valve | 25 |
| 2.3 The variable geometry turbocharger | 26 |
| 2.4 GT-Suite modelling environment | 26 |
| 2.5 SimuLink coupling | 28 |
| 3 Engine Operating Points | 31 |
| 3.1 Operating points selection | 31 |
| 3.2 Operating points recognition | 33 |
| 3.2.1 Mapping for control purposes | 34 |
| 3.3 Control points association | 35 |
| 3.3.1 Vicinity mapping | 36 |
| 3.3.2 Affinity mapping | 36 |
| 3.3.3 K-means clustering | 39 |
| 3.4 Results analogies and purpose | 42 |
| 4 System Identification | 45 |
| 4.1 The identification variables | 45 |
| 4.2 Step testing | 46 |
| 4.3 The identification signal | 49 |
| 4.4 Models overview | 51 |

| | | |
|----------|---|------------|
| 4.4.1 | The ARX model | 51 |
| 4.4.2 | The ARMAX model | 52 |
| 4.4.3 | The OE model | 53 |
| 4.4.4 | State-space model | 55 |
| 4.5 | Decoupled identification process and results | 55 |
| 4.5.1 | EGR identification | 58 |
| 4.5.2 | VGT identification | 63 |
| 4.6 | Identification summary and prospects | 65 |
| 5 | Control | 67 |
| 5.1 | Control EOPs selection | 67 |
| 5.1.1 | The ARMAX case | 72 |
| 5.1.2 | The state-space case | 73 |
| 5.2 | Median CEOPs selection | 80 |
| 5.3 | Benchmark selection | 81 |
| 5.4 | Benchmark single controller design | 83 |
| 5.4.1 | Control requirements | 83 |
| 5.4.2 | Used networks and control design | 84 |
| 5.4.3 | EGR control on benchmark EOP | 85 |
| 5.4.4 | VGT control on benchmark EOP | 86 |
| 5.5 | Control performance on EOP n. 15 | 87 |
| 5.5.1 | Test sequences outline | 88 |
| 5.5.2 | Tracking - Calm test sequence | 89 |
| 5.5.3 | Tracking - Moderate test sequence | 90 |
| 5.5.4 | Tracking - Aggressive test sequence | 91 |
| 5.5.5 | Tracking - Pedal-given test sequence | 93 |
| 5.6 | Results and additional control components | 94 |
| 6 | Anti-windup Architectures | 97 |
| 6.1 | Baseline architecture | 98 |
| 6.2 | Moving average smoothing | 100 |
| 6.3 | Zeroing activation thresholds | 102 |
| 6.4 | Conditional integration | 104 |
| 6.5 | Generalized form architecture | 106 |
| 6.6 | Performance correlation | 110 |
| 7 | Gain Scheduling Control | 113 |
| 7.1 | Four CEOPs gain-scheduling | 114 |
| 7.1.1 | Affinity <i>vs</i> vicinity mapping: performance comparison | 120 |
| 7.2 | Whole engine map gain-scheduling | 125 |
| 7.3 | Preliminary testing | 128 |
| 7.4 | Fuel injected quantity correction and filters refinement | 131 |
| 7.4.1 | Tracking - Pedal-given test sequence | 134 |
| 7.4.2 | Tracking - Actuators limits test sequence | 136 |
| 7.4.3 | Tracking - WHTC test sequence | 137 |
| 7.5 | Results overview and assessment | 140 |

List of Tables

| | | |
|------|--|-----|
| 2.1 | Engine main specifications | 23 |
| 4.1 | EGR step test outputs variation assessment | 48 |
| 4.2 | VGT step test outputs variation assessment | 49 |
| 4.3 | ARX identification on case n. 2 - Validation metrics report | 58 |
| 4.4 | ARMAX identification on case n. 2 - Validation metrics report | 59 |
| 4.5 | OE identification on case n. 2 - Validation metrics report | 60 |
| 4.6 | SS identification on case n. 2 - Validation metrics report | 61 |
| 4.7 | Selected models identification on EGR case n. 2 - Validation metrics | 63 |
| 4.8 | Selected models identification on EGR case n. 10 - Validation metrics | 63 |
| 4.9 | Selected models identification on VGT case n. 2 - Validation metrics report | 64 |
| 4.10 | Selected models identification on VGT case n. 10 - Validation metrics report | 65 |
| 5.1 | Initial EOPs and corresponding replacements. Control EOPs are in bold | 72 |
| 5.2 | $K_{P,EGR}$ gains for original models and replacing CEOPs, for continuous domain SS model family | 74 |
| 5.3 | Fit percentages for $CEOP_8$ and $CEOP_{med}$ on SS models | 80 |
| 5.4 | Order 2 SS models EGR benchmarks with respect to EOP n. 15; case 16, using its own model, would yield an 88.3% correlation performance | 82 |
| 5.5 | Order 2 SS models VGT benchmarks with respect to EOP n. 15 | 83 |
| 5.6 | Plant models and proportional and integral gains of EGR and VGT controllers, for benchmark case n. 15, featuring 1800 <i>rpm</i> and 6.76 <i>bar</i> | 87 |
| 6.1 | Boolean decisional logic of baseline anti-windup architecture | 99 |
| 6.2 | Boolean decisional logic of baseline anti-windup architecture | 102 |
| 7.1 | The four CEOPs, chosen to build the prototype gain-scheduling controller | 115 |
| 7.2 | The four CEOPs, gain-scheduling and plant transfer functions for EGR controller | 115 |
| 7.3 | The four CEOPs, gain-scheduling and plant transfer functions for VGT controller | 116 |

List of Figures

| | | |
|------|--|----|
| 2.1 | Engine model air-path scheme | 25 |
| 2.2 | Exhaust gas recirculation valve, courtesy of DENERG, Politecnico di Torino | 25 |
| 2.3 | A variable geometry turbocharger, courtesy of DENERG, Politecnico di Torino | 26 |
| 2.4 | GT-Power environment engine modelling | 28 |
| 2.5 | Interface blocks for smimulations environments coupling; to the left, SimuLink-as-Lead interface block; to the right, GT-as-Lead one | 29 |
| 3.1 | The 126 tested EOPs | 32 |
| 3.2 | Selected EOPs, in red, with highlighted twenty subregions subdivision. Numbering of the selected EOPs is shown | 33 |
| 3.3 | EOP recognition, <i>engine speed</i> = 1400 rpm, <i>BMEP</i> = 3.5 bar | 34 |
| 3.4 | Engine map design and usage through GT-Power - SimuLink coupling | 35 |
| 3.5 | CEOPs recognition, <i>engine speed</i> and <i>BMEP</i> values uniformly spanned across engine map, using <i>vicinity</i> mapping. CEOPs are numbered following same numbering of EOPs. | 36 |
| 3.6 | Assignment of the current engine state (ω_c, p_c), in green, to a CEOP that is not the closest, following an <i>affinity</i> principle | 37 |
| 3.7 | CEOPs recognition, <i>engine speed</i> and <i>BMEP</i> values uniformly spanned across engine map, improved method | 38 |
| 3.8 | K-means clustering different outcomes, with $k = 12$ clusters, applied $n = 9$ times, with different initial centroids guesses. EOPs connected by black lines belong to the same cluster | 40 |
| 3.9 | Average of k-means clustering nine outcomes with different initial centroids guesses. Thicker lines indicate two EOPs are more prone to belong to same cluster | 41 |
| 3.10 | Average of k-means clustering outcomes with different initial centroids guesses, filtered to obtain exactly twelve CEOPs. Thicker lines indicate two EOPs are more prone to belong to same cluster. Blue points represent a possible CEOPs choice and capital letters indicate main interest areas | 41 |
| 3.11 | Average of k-means clustering nine outcomes with different initial centroids guesses, filtered so as to obtain exactly twelve CEOPs. EOPs vicinity is taken into account in clustering process and thicker lines indicate two EOPs are more prone to belong to same cluster. Blue points represent a possible CEOPs choice | 42 |
| 4.1 | SimuLink standardized step signal generation | 47 |
| 4.2 | An EGR sample step test, EGR valve opens from 20 to 50% of its total size | 47 |

| | | |
|------|---|----|
| 4.3 | Normalized constant amplitude identification series; 1, 0.5 and 0 correspond to upper threshold, benchmark and lower threshold normalized valve position values. Starting value and a signal re-initialization are circled in red | 51 |
| 4.4 | ARX model in simulation form. Credits [33] | 52 |
| 4.5 | ARMAX model in simulation form. Credits [33] | 53 |
| 4.6 | OE model in simulation form. Credits [33] | 53 |
| 4.7 | ARMAX model in prediction form (bottom part) and physical system (top part). Credits [33] | 54 |
| 4.8 | SS model block scheme. Adapted from [31] | 55 |
| 4.9 | Engine map highlighting the EOPs over which a detailed identification procedure is provided for the four highlighted points | 57 |
| 4.10 | EGR control action and \dot{m}_{air} response in case n. 2 | 61 |
| 4.11 | ARX model with $n_k = 1$, $n_a = n_b = 2$, EGR control action variation and \dot{m}_{air} variation in case n. 2 - comparison with validation dataset | 62 |
| 4.12 | SS model with $n_k = 1$, $n = 2$, VGT control action and <i>IMAP</i> response in case n. 2 - comparison with validation dataset | 64 |
| 5.1 | EOPs mutual relationships, for both EGR (top) and VGT (bottom) models, exponential linewidth. Thicker lines representing high affinity between two points | 69 |
| 5.2 | Chosen control EOPs and mutual relationships, for both EGR (top) and VGT (bottom) models. Thicker lines representing high affinity between two points. A four point cluster is highlighted in green | 71 |
| 5.3 | Chosen CEOPs, replacing original EOPs; replacement is shown by black lines | 72 |
| 5.4 | Continuous ARMAX zeros-poles map of the eight replaced original EOPs and their replacing CEOPs | 73 |
| 5.5 | Continuous SS zeros-poles map of the eight replaced original EOPs and their replacing CEOPs, [0; 50] axes range | 75 |
| 5.6 | Continuous SS magnitude Bode plot of the eight replaced original EOPs and their replacing CEOPs | 76 |
| 5.7 | Continuous SS phase Bode plot of the eight replaced original EOPs and their replacing CEOPs | 77 |
| 5.8 | Continuous SS Nichols plot of the eight replaced original EOPs and their replacing CEOPs | 78 |
| 5.9 | Superimposed continuous SS Bode magnitude plots of the twenty original EOPs and replacing CEOPs | 79 |
| 5.10 | EOPs and benchmark point, case n. 15, in blue, at 1800 <i>rpm</i> and 6.76 <i>bar</i> | 82 |
| 5.11 | Nichols chart on EGR controller n. 15, highlighting the subsequent controller refinements | 86 |
| 5.12 | Nichols chart on VGT controller n. 15, highlighting the subsequent controller refinements | 87 |
| 5.13 | Mapped target boost pressure, obtained from <i>BMEP</i> and engine speed, in turn coming from GT-Power | 88 |
| 5.14 | Assessment test sequences: from left to right and from top to bottom, in order, calm, moderate, aggressive and pedal-given engine cycles | 89 |
| 5.15 | Control performance, with EGR and VGT mapped values, on calm test sequence, see 5.14 | 90 |

| | | |
|------|---|-----|
| 5.16 | Control performance, with EGR and VGT controllers, on calm test sequence, see 5.14 | 90 |
| 5.17 | Control performance, with EGR and VGT mapped values, on moderate test sequence, see 5.14 | 91 |
| 5.18 | Control performance, with EGR and VGT controllers, on moderate test sequence, see 5.14 | 91 |
| 5.19 | Control performance, with EGR and VGT mapped values, on aggressive test sequence, see 5.14 | 92 |
| 5.20 | Control performance, with EGR and VGT controllers, on aggressive test sequence, see 5.14 | 92 |
| 5.21 | Control performance, with EGR and VGT controllers, on aggressive test sequence, see 5.14; EGR controller gain is reduced and averaged engine speed is fed | 93 |
| 5.22 | Control performance, with EGR and VGT mapped values, on pedal-given test sequence, see 5.14 | 93 |
| 5.23 | Control performance, with EGR and VGT mapped values, on pedal-given test sequence, see 5.14; averaged engine speed values are fed | 94 |
| 5.24 | Control performance, with EGR and VGT controllers, on pedal-given test sequence, see 5.14; EGR controller gain is reduced and averaged engine speed is fed | 94 |
| 6.1 | VGT controller scheme, with anti-windup architecture and standardized VGT fixed point | 98 |
| 6.2 | Anti-windup architecture, defined through boolean operators, here represented for the VGT control | 98 |
| 6.3 | <i>IMAP</i> target <i>vs</i> actual value, <i>IMAP</i> error and rack position, <i>without</i> using anti-windup architecture on VGT | 99 |
| 6.4 | <i>IMAP</i> target <i>vs</i> actual value, <i>IMAP</i> error with and without anti-windup and rack position, when using baseline anti-windup architecture on VGT | 100 |
| 6.5 | <i>IMAP</i> target <i>vs</i> actual value and rack position, without and with AW baseline architecture | 100 |
| 6.6 | Anti-windup architecture, with moving average on target error, here represented for the VGT control | 101 |
| 6.7 | <i>IMAP</i> target <i>vs</i> actual value, <i>IMAP</i> error in with and without anti-windup and rack position, anti-windup architecture with moving average, on VGT control | 101 |
| 6.8 | <i>IMAP</i> target <i>vs</i> actual value and rack position, anti-windup architecture with moving average, on VGT control | 102 |
| 6.9 | Anti-windup architecture, with 10^{-4} bar activation threshold on target error variation, represented for the VGT control | 103 |
| 6.10 | <i>IMAP</i> target <i>vs</i> actual value, <i>IMAP</i> error in with and without anti-windup and valve position, when using anti-windup architecture on VGT, with 10^{-4} bar activation thresholds | 103 |
| 6.11 | <i>IMAP</i> target <i>vs</i> actual value and rack position, when using anti-windup architecture on VGT, with 10^{-4} bar activation thresholds | 104 |
| 6.12 | Anti-windup architecture through conditional integration, represented for the VGT control | 105 |

| | | |
|------|--|-----|
| 6.13 | Anti-windup decisional logic in conditional integration, represented for the VGT control | 105 |
| 6.14 | <i>IMAP</i> target <i>vs</i> actual value, <i>IMAP</i> error in with and without anti-windup and rack position, with conditional integration anti-windup architecture applied on VGT controller | 106 |
| 6.15 | <i>IMAP</i> target <i>vs</i> actual value and rack position, with conditional integration anti-windup architecture applied on VGT controller | 106 |
| 6.16 | Anti-windup generalized form architecture, represented for the VGT control; $\Gamma(s) = G(s) = 1 + s$. Circled block is the actuation saturation | 108 |
| 6.17 | <i>IMAP</i> target <i>vs</i> actual value, <i>IMAP</i> error with built-in anti-windup and rack position, with general anti-windup architecture applied on VGT controller | 109 |
| 6.18 | <i>IMAP</i> target <i>vs</i> actual value and rack position, with general anti-windup architecture applied on VGT controller | 109 |
| 6.19 | <i>IMAP</i> target <i>vs</i> actual value, without anti-windup and with the five different anti-windup architectures | 110 |
| 7.1 | The four selected CEOPs, filled in black, chosen among the twelve CEOPs, in blue; benchmark point n. 15 is highlighted in filled red dot | 114 |
| 7.2 | EGR zeros and poles of the four selected benchmark plants, [0; 60] axes range | 116 |
| 7.3 | VGT zeros and poles of the four selected benchmark plants, [0; 50] axes range. CEOP n. 8 features an additional high frequency zero | 117 |
| 7.4 | $K_{P,EGR}$ in four points mapping, <i>vicinity vs affinity mapping</i> , with labelled CEOPs numbers | 117 |
| 7.5 | VGT PI control scheme, with four points gain-scheduling and command for integral anti-windup | 118 |
| 7.6 | Control performance, with EGR and VGT gain-scheduled controllers, on four points vicinity mapping, on aggressive test sequence, see 5.14 | 119 |
| 7.7 | Scheduled EGR gains variation on four points vicinity mapping, in parallel with target and actual air (left) and EGR command (right), on aggressive sequence, see 5.14 | 119 |
| 7.8 | Control performance, with EGR and VGT gain-scheduled controllers, on four points affinity mapping, on aggressive test sequence, see 5.14 | 120 |
| 7.9 | Scheduled EGR gains variation on four points affinity mapping, in parallel with target and actual air (left) and EGR command (right), on aggressive test sequence, see 5.14 | 120 |
| 7.10 | Tracking performance on EGR valve; target air flow is compared to benchmark control on EOP n. 15 and to four CEOPs controller, with <i>standard</i> and <i>affinity</i> mapping, on aggressive test sequence, see 5.14 | 121 |
| 7.11 | Enlargement - Tracking performance on EGR valve; target air flow <i>vs</i> benchmark control on EOP n.15 <i>vs</i> four CEOPs controller, <i>standard</i> and <i>affinity</i> mapping, on aggressive test sequence, see 5.14 | 122 |
| 7.12 | Control performance, with EGR and VGT gain-scheduled controllers, on four points affinity mapping, VGT command is post-filtered, on aggressive test sequence, see 5.14 | 123 |
| 7.13 | Scheduled EGR gains variation on four points affinity mapping, VGT command is filtered, in parallel with target and actual air (left) and EGR command (right), on aggressive test sequence, see 5.14 | 123 |

| | | |
|------|---|-----|
| 7.14 | Tracking performance on EGR valve; target air flow is compared to benchmark control on EOP n. 15 and to four CEOPs controller, with <i>standard</i> and <i>affinity</i> mapping and VGT post-filtering on <i>affinity</i> mapping, on aggressive test sequence, see 5.14 | 124 |
| 7.15 | Enlargement - Tracking performance on EGR valve; target air flow <i>vs</i> benchmark control on EOP n. 15 <i>vs</i> four CEOPs controller, <i>standard</i> and <i>affinity</i> mapping and VGT post-filtering on <i>affinity</i> mapping, on aggressive test sequence, see 5.14 | 125 |
| 7.16 | $K_{I,EGR}$ and $K_{P,EGR}$ gain-scheduling maps, through <i>affinity</i> mapping | 126 |
| 7.17 | $K_{I,VGT}$, to the left, and $K_{P,VGT}$, to the right, gain-scheduling maps, through <i>affinity</i> mapping | 127 |
| 7.18 | Assessment test sequences: from left to right and from top to bottom, in order, aggressive test sequence, moderate pedal-given engine cycle, actuator limits pedal-given engine cycle and WHTC engine cycle | 128 |
| 7.19 | Air mass flow rate tracking performance, with EGR and VGT gain-scheduled controllers, on whole map affinity mapping, VGT command is post-filtered, on WHTC test sequence, see 7.18 for reference | 129 |
| 7.20 | Boost pressure tracking performance, with EGR and VGT gain-scheduled controllers, on whole map affinity mapping, VGT command is post-filtered, on WHTC test sequence, see 7.18 for reference | 130 |
| 7.21 | EGR valve position command with EGR and VGT gain-scheduled controllers, on whole map affinity mapping, VGT command is filtered, on WHTC test sequence, see 7.18 for reference | 130 |
| 7.22 | VGT rack position command, with EGR and VGT gain-scheduled controllers, on whole map affinity mapping, VGT command is filtered, on WHTC test sequence, see 7.18 for reference | 131 |
| 7.23 | Derivative of fuel injected quantity, marked by letter <i>B</i> , is used as a correcting term in EGR control action | 132 |
| 7.24 | Comparison between control architectures equipped with A, A-B, A-C and A-B-C; A, B, C standing for mapped control, injected fuel derivative contribution and PI controller, respectively. Target air and <i>IMAP</i> values are highlighted with dotted line and ECU experimental values are marked in red | 133 |
| 7.25 | Enlargement: comparison between control architectures equipped with A, A-B, A-C and A-B-C; A, B, C standing for mapped control, injected fuel derivative contribution and PI controller, respectively. Target air and <i>IMAP</i> values are highlighted with dotted line and ECU experimental values are marked in red | 134 |
| 7.26 | Air tracking performance, to the left, followed by <i>IMAP</i> tracking, to the right. Gain-scheduling controllers are based on whole map affinity mapping and performance is assessed on pedal-given test sequence, for $t = 10 - 400$ s, see 7.18 for reference | 134 |
| 7.27 | EGR control action, to the left, followed by VGT one, to the right. Gain-scheduling controllers are based on whole map affinity mapping and performance is assessed on pedal-given test sequence, for $t = 10 - 400$ s, see 7.18 for reference | 135 |

| | | |
|------|---|-----|
| 7.28 | Air tracking performance, to the left, followed by <i>IMAP</i> tracking, to the right. Gain-scheduling controllers are based on whole map affinity mapping and performance is assessed on actuators limits test sequence, for $t = 520 - 620$ s, see 7.18 for reference | 136 |
| 7.29 | EGR control action, to the left, followed by VGT one, to the right. Gain-scheduling controllers are based on whole map affinity mapping and performance is assessed on actuators limits test sequence, for $t = 520 - 620$ s, see 7.18 for reference | 137 |
| 7.30 | Air mass flow rate tracking performance, with EGR and VGT gain-scheduled controllers, on whole map affinity mapping, VGT command is post-filtered, on WHTC test sequence, see 7.18 for reference | 138 |
| 7.31 | Boost pressure tracking performance, with EGR and VGT gain-scheduled controllers, on whole map affinity mapping, VGT command is post-filtered and derivative of injected fuel correction is inserted, on WHTC test sequence, see 7.18 for reference | 138 |
| 7.32 | EGR valve position command with EGR and VGT gain-scheduled controllers, on whole map affinity mapping, VGT command is filtered and derivative of injected fuel correction is inserted, on WHTC test sequence, see 7.18 for reference | 139 |
| 7.33 | VGT rack position command, with EGR and VGT gain-scheduled controllers, on whole map affinity mapping, VGT command is filtered, on WHTC test sequence, see 7.18 for reference | 139 |

Chapter 1

Introduction

The enforcement of stricter pollutant emissions requirements, along with the technological need for constantly developing new, more efficient, solutions for the improvement of engine overall performance, has pushed the application of a wide variety of control architectures, whose scope is tackling this problem. Jointly, this issue has forced the testing of numerous system identification techniques, playing a key role in providing a tailored set equations, upon which the control architecture is built.

1.1 Problem definition

Aim of the dissertation is the improvement of a benchmark control logic, adopted on a 3-litre, four cylinders diesel engine, with a new control architecture, based on the gain-scheduling control technique. The control scheme is applied to targeted engine areas, and specifically to the engine airpath. Thesis work demonstrates the effectiveness of the control logic, thus highlighting the degree of development that the exploitation of such technologies offers. The construction of the replacing control logic takes place in three main steps, here outlined.

- Identification of the mathematical models, representing the physical behaviour of the engine airpath over the engine map, *i.e.* the engine operating space
- Development of a tailored control architecture, based on the engine models obtained at previous step.
- Validation of the control results, further refinement, and comparison with benchmark control logic.

Target of the engineer is, therefore, to identify and assess a model that is then used as a basis for control purposes. The extraction of a valuable model characterization, as well as a reliable control logic, strongly depends on a proper engine airpath model, on which to design both identification and control. This point is addressed employing a digital twin of the engine, developed on GT-Power and MatLab/SimuLink environment. The presented general procedure is here specifically applied to engine valve actuators of the Exhaust Gas

Re-circulation, also known as EGR, and to the Variable Geometry Turbocharger, or VGT. It is, in any case, worth to mention that the chain *identification-control-validation* procedure is general and widely applied in numerous automotive subsystems, *e.g.* suspensions, torque-related ABS and ESP systems, hybrid powertrain control, as well as in other engineering fields. Main technologies involved in the execution of the afore-mentioned three core points, building the thesis framework, are illustrated.

1.1.1 System identification

Airpath modelling, intended as the extraction of mathematical relationships that interconnect the studied variables, in an attempt to control them, can be performed through various routes, ranging from the attainment of direct engine physical equations [6], to more complex models, such as those coming from neural networks identification [12]. It is evident that the selection of a model that adequately fits the true engine dynamics, yet at the same time being reasonably simple, is not trivial, consequently much effort has to be made on the design of the proper modelling procedure. First attempts in this direction have been the evaluation of a physics-derived engine airpath set of equations, yielding an accurate, yet at times cumbersome mathematical description of the former [11][15][16][17][26]. An example for this is given by Wahlström [18], providing an eight-state definition of the engine airpath. However complex, the proposed model is highly descriptive and it entails a rich representation of most of the variables involved in the engine operation.

Subsequent steps are the usage of system identification techniques, whose main contribution is the simplification of the whole physical engine model, and its compression into a simple set of either linear or non-linear equations [1][2][15][16][19][23]. Such techniques rely only on input-output data measurements on a real engine, *i.e.* collected on a test bank, and on *a priori* information on the model dynamics: their outcome is the exploitation of such data to extract and tune an engine mathematical description, that is tailored for control purposes. One last model assessment is obtained through extensive usage of neural networks [12][29], that replace the more standardized state equations stemming from classical system identification techniques. Here, input and output engine data are fed to a network forest, that is trained, validated and, when necessary, pruned, so as to obtain a reasonable estimate of the engine parameters.

1.1.2 Control logics overview

Discerning a control architecture that provides, at the same time, trustworthy and predictable results and an easy tuning is essential. Concerning this, several control schemes are enumerated, starting from the classical PID control scheme, widely applied in the automotive field [7][11][21][22], and ranging to general state feedback control [2][11][19], to model predictive control, or MPC, aimed at the minimization of a proper cost function, to fulfill a set of requirements over a given time horizon, in the best possible way [15][20][22][23][24][25][27].

Less conventional control schemes, such as artificial neural network control, have been applied to airpath control, so as to enhance engine performance and to avoid, or at least to limit, either response overshoots or lags, such as tail effects [12]. Along with neural

networks, Lyapunov control design has been taken on by Jankovic [8] sharing targets, such as fast output response to the given command variables, and control law simplicity, a point that is crucial, bearing in mind that each step a controller processes has then to be replicated on an actual engine. Decoupled control is proposed by Hui [10], that decomposes the system into a double-input-double-output, or DIDO, adopting two different integrators, and treating uncertainty and other effects as a total disturbance. A different procedure is followed by Wahlström [18], that aims at highlighting the system non-linear dynamics, providing an elaborate eight-states model of the airpath, where *e.g.* heat losses and other non-linearities, as well as coupled behaviours, are taken into account. One last example is the gain scheduling controller, proposed by Seungwoo [7], managing non-linearities between control inputs and outputs. Gain scheduling, used in tuning of PID controllers and state-feedback control, is the core control logic adopted in the dissertation.

Control logics, however presented separately, may work together so as to boost tracking performance of the output variables, for this reason a number of additional blocks are added to the starting control scheme, *e.g.* anti-windup architectures and pre- and post-filtering techniques, to smooth reference signals as well as control actuations.

1.1.3 Validation criteria

The results obtained from identification and control of the valves actuation is validated at each procedural step. Identification quality is defined in terms of performance indicators, such as root mean-square errors, Akaike's information criterion [13] and others. The building and validation of the selected control architecture is performed in a step-by-step manner, through well-defined iterations.

A first controller, based on a *single* identified model, is tested on the engine simulation environment: this serves as first comparison basis; its validation is performed comparing the control outcome to a feedforward valves mapped control.

Then, control architecture is progressively enriched with gain-scheduling techniques, and more linear controllers are exploited, one per each engine functioning area. This latter control model, comprehensive of further devices, such as filters and anti-windup structures, is eventually compared to a *benchmark* standard control, that sets a reference for the quality outcome of the whole work.

1.2 Engine considered actuators

In this section, the two studied valves, EGR and VGT, are presented, and an overview of their functioning principles is given. A full engine airpath description is provided in Chapter 2.

1.2.1 The EGR

Exhaust gases re-circulation forces a fraction, being in conventional diesel engines from ca. 10 to 15%, but stretching up to 50% in non-conventional applications, of the exhaust gases to go back into the cylinders, to mix with fresh air and start a new engine cycle. Exhaust gases are low in oxygen, compared to fresh air originally entering the cylinders,

and are therefore not prone to formation of NO_x noxious compounds [19]. The EGR valve has therefore an edge over previous engine architectures not adopting it, and has become mandatory for newly registered vehicles.

Valve behaviour is non-linear, the reasons for this being essentially two:

- Due to valve design, a small variation in opening, when the inlet orifice is almost closed, will yield a noticeable increase in flow area; conversely, the same opening enlargement, when the inlet is already wide opened, will bring no major changes in flow area, reaching the valve choking.
- Formation of whirls occurs when gases mixture exits the valve, as there is an abrupt transition from a smaller to a wider cross section area.

The valve intrinsic non-linearity is the main reason for the application of gain-scheduling PID controllers, to achieve desired target tracking performance.

The EGR valves feature a double scope, that is here listed:

- Heat rejection reduction, resulting from lower peak combustion temperatures and consequent lower thermal exchange between chamber surfaces [3].
- Minor reduction of chemical dissociation, positively affecting the energy conversion efficiency.

In gasoline engines, EGR valve has the additional advantage of reducing throttle losses, coming from the need for opening the throttle plate further, resulting in a higher inlet manifold pressure.

EGR device is generally not used at both idle and high loads. The reason for the former being unstable combustion, causing engine wearing, and for the latter being the lower peak power input, that is a direct consequence of the lower density of the intake charge, when mixed with exhaust gases; further reference to this point is given in Chapter 3.

1.2.2 The VGT

Variable geometry turbocharger is a common feature in most diesel engines, and consists of a rotor, placed in the exhaust manifold, able to generate torque through the exhaust gases. Such torque is then given, through a connecting crankshaft, to a compressor, raising the inlet mixture pressure. The variable geometry, intended as a variable aspect ratio that is altered depending on engine conditions, is reached through adjustable vanes, in turn regulated by the opening/closing of a damper. The aspect ratio variation has an influence on the amount of produced torque, and can be therefore tuned to achieve the best possible performance.

VGT dynamics are non-linear, due to the non-uniform aspect ratio change; furthermore, the valve functioning partially overlaps with EGR dynamics, resulting in the coupled behaviour of the two of them [4][17].

VGT systems are mostly built in two versions, for light-duty and heavy-duty engines, with the former featuring rotating turbine vanes and the latter featuring a change in blades

effective width. VGTs are mostly produced by OEMs, due to their required levels of precision and coordination.

1.3 Chapters synopsis

The final part of the introductory chapter is devoted to the description of the thesis content, divided into chapters that underline the work roadmap.

Chapter 2 offers a preliminary description of the engine operating principles. A piecewise description of the internal combustion engine is given, and an in-depth analysis of the examined actuators is performed. Following that, Chapter 3 targets the engine map subdivision into smaller areas, with a view to building a dedicated control algorithm for each operating subregion. In this chapter, more partitioning criteria are assessed, laying a basis for the implementation of the subsequent work steps.

Chapter 4 investigates the choice of a fitting model for each engine operating area via *system identification*. Engine input-output data are collected, using a customized identification signal, whose description is provided. Chapter concludes with the evaluation of fitting performance of the identified model families to the fed data.

The selection of the engine regions on which to build the controllers are issued in Chapter 5. Here, the selected regions are chosen following affinity criteria. Subsequently, compensators are built basing on a requirements set, and their theoretical and practical performance are assessed. Chapter 6 deals with the critical challenge of *anti-windup*, emerging in case of actuators saturation. Several anti-windup architectures are proposed and compared, and the obtained results are exploited to improve control performance. Last Chapter, 7, describes the development of a gain-scheduling PID-based controller. This constitutes the macroscopic outcome of the thesis work. Ensuing steps are the progressive refinement of control variables, the addition of custom-fit logics to tackle specific engine areas, and the pre- and post-filtering of actuation commands.

Chapter 7 comes to an end with a thorough evaluation of the obtained control performances, and a comparison with a benchmark control, highlighting the advance made with the development of this control logic.

Chapter 2

The Internal Combustion Engine

This chapter describes the engine model that is adopted for the scope of this dissertation, along with the schemes that are used in order to properly represent it in the simulation environment. Coupling with SimuLink environment, employed to build the control architectures, is illustrated.

2.1 Technical specifications

Studied engine is a 3-litre Euro VI diesel turbocharged, four cylinder component, produced by a leading engine manufacturer and mounted mainly on light and heavy-duty vehicles. The engine is endowed with HP-EGR, pneumatically actuated VGT, intercooler and EGR cooler[1], that will be investigated in the next lines. Engine maximum generated power is 129 kW at 3500 rpm and maximum torque 430 Nm; further details are provided in Table 2.1.

| | |
|-----------------------|---------------------------|
| Engine type | Euro VI diesel engine |
| Number of cylinders | 4 |
| Displacement | 2998 cm ³ |
| Bore x stroke | 95.8x104 mm |
| Rod length | 160 mm |
| Compression ratio | 17.5 : 1 |
| Valves per cylinder | 4 |
| Turbocharger | VGT type |
| Fuel injection system | High Pressure Common Rail |

Table 2.1: Engine main specifications

The engine is mounted on an engine bank, in Politecnico di Torino, where on-engine experiments are run and data are collected; data can be collected either directly through engine sensors, placed on the engine, or through the ECU. ICE main components scheme

is modelled as in Figure 2.1; here an inlet pipe can be seen, from which the gases enter the engine, followed by a compressor, sharing its shaft with a turbine, placed on the outlet pipe of the engine. The compressor is closely followed by an intercooler, that aims at cooling the previously compressed gases, counteracting the compression heat; the intercooler, moreover, allows the gas to become denser, enabling the usage of more fuel. To this regard, for mechanical assembly reasons, intercooler pipes length changes from on-vehicle mounted engine and test bank mounting scheme.

The last component is followed by a pipe junction: the exhaust gas re-circulation (EGR) pipe streams into the intake manifold together with the cooled compressed gases. The mixture, at this point, is ready to enter the intake manifold. It is wise to mention that no reservoir, acting as a capacitor and whose scope is to provide a pressure boost when needed, e.g. either at low *rpm* or when switching on the engine, was present, since the engine already has a turbocharger. This latter engineering choice was indeed adopted on elder car models and is now fallen into disuse.

Air mixture is then brought into the cylinders through the intake valves and the compression phase heats it. When almost at the top dead centre, fuel is injected through an injector, in form of a fine spray, and it gets burnt due to the high temperature and pressure reached by the mixture. Ignition is spontaneous, occurring without the need for a spark. The exhaust stroke forces the spent mixture out of the combustion chamber, through the exhaust manifold that is cascaded after the cylinders. In the following pipe, a flow split takes place: part of the gases are brought to the turbine and then out through an outlet pipe, part of them are recirculated via an exhaust gas re-circulation (EGR) valve. After going past the valve, gases are led into an EGR cooler and then back into the cycle, with the cooled compressed intake gases.

The engine turbine is a variable-geometry turbocharger, whose scope is reached with the use of adjustable vanes, that are located inside the turbine housing, between inlet and rotor, affecting flow of gases towards the turbine blades. The usage of such vanes has benefits on the aspect ratio of the turbine, that needs to noticeably vary from low engine speeds to high engine speeds.

If the aspect ratio were too large, the turbo would fail to create boost at low speeds; the other way round, if the aspect ratio were too small, the turbo would choke the engine at high speeds, leading to high exhaust manifold pressures, as well as high pumping losses and ultimately lower power output. If the turbine geometry is altered, the turbo aspect ratio is varied with a view to maintaining it at its optimum. This is a clear reason why, when correctly tuned, VGTs guarantee a minimal lag amount, a low boost threshold and high efficiency when engine speed increases.

An Exhaust Flow Valve, also known as EFV, is eventually placed at the outlet pipe of the turbine; regulation of this valve is demanded to the EGR actuation itself, through a non-linear mapped relationship, to increase the amount of recirculated gases.

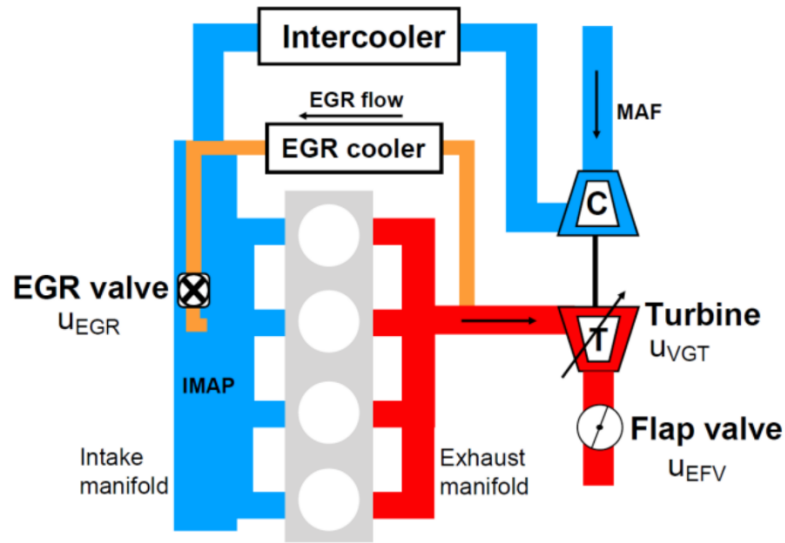


Figure 2.1: Engine model air-path scheme

2.2 The exhaust gas recirculation valve

An exhaust recirculation valve, to be equipped on diesel engines, is reported in Figure 2.2, providing two different views of the valve. EGR is accomplished through a poppet valve, using the linear sliding motion of a piston inside a seat to open and close the passageways. Valve name refers to the gate movement, sliding longitudinally within the valve body as the air flows perpendicularly to the spool. Valve actuation takes place in the housing behind the valve, to the left of Figure 2.2a. Valve intake, to the right in 2.2b, and valve exhaust, placed perpendicularly to piston movement, are visible in the same figure.



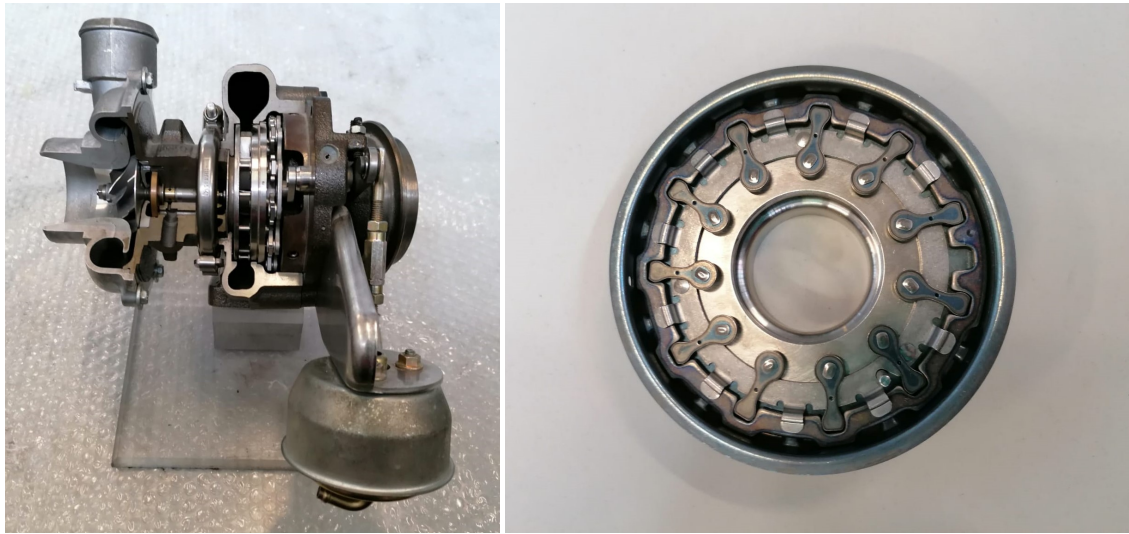
(a) Lateral view

(b) Detail - Valve intake

Figure 2.2: Exhaust gas recirculation valve, courtesy of DENERG, Politecnico di Torino

2.3 The variable geometry turbocharger

An example of variable geometry turbocharger is given in Figure 2.3, showing the whole mechanism of the actuation, provided by a rod. The rod pulls the inner rim of the stator of the turbine, from which the movement is transferred to the stator vanes, whose orientation changes, allowing less or more air to radially enter the vanes. The vanes of the turbine rotate in unison, relative to their hub, to vary pitch and cross-sectional area. The described mechanical distinctive features of the VGT make it slower than the EGR valve.



(a) Front view

(b) Detail - Rack position variation mechanism

Figure 2.3: A variable geometry turbocharger, courtesy of DENERG, Politecnico di Torino

2.4 GT-Suite modelling environment

The development of a reliable control logic is performed on virtual environment, with the help of specific modelling tools. Modelling of the engine plant is done on GT-Power, industry standard engine performance simulation, an FEM analysis application that is used by practically all major engine manufacturers, as well as vehicle Original Equipment Manufacturers, also known as OEMs. The software is developed by Gamma Technologies. For what concerns this last point, a further model is built on SimuLink environment, using the Powertrain Blockset toolbox, provided by MathWorks. This model is a simplified version of the GT-Power more complex one and is intended to help, on a preliminary basis, the user understanding the main involved variables, within the EGR and VGT control framework, as well as in the more general engine principles understanding one.

The GT-Power adopted simulation scheme is described in Figure 2.4, where, from top to bottom, five key model units are labelled, as here reported.

- A. Cylinders, injection valves and intake and exhaust manifolds.

- B. EGR valve actuator
- C. Turbocharger, with highlighted common shaft.
- D. VGT valve actuator
- E. SimuLink-GT-Power interface.

The engine plant follows closely the architecture proposed in Section 2.1: gases to be combusted first enter the compressor stage, then through the intercooler and then they enter the cylinder intake manifold, before entering the actual cylinders. Cylinders are described separately, so as to make the model as realistic as possible. The engine crank train is placed right to the side of the cylinders and is used to evaluate engine speed and torques (*e.g.* brake torque, inertial torques, such as crankshaft torque and piston/rod torque). Exhaust gases are collected through the exhaust manifold and then their recirculation is enabled through an EGR valve, followed by another intercooler. Output product of the plant is gases that are not recirculated: this part is therefore led through a turbine, whose crankshaft is connected to the compressor. Exhaust gases then go through an exhaust flap and are dissipated in the atmosphere.

GT-Power architecture models pipe objects as finite element components, where heat dissipation is taken into account through Colburn model; pressure drop is modelled via friction coefficients. To further enhance realism of the simulation, specific components, such as the intercooler after the compressor, are modelled through two pipes, connected in series, one before the heat exchange block and one after it. GT-Power model base relies on the most classical physical equations describing engine components linking, among others, pressure ratios, corrected air mass flows, enthalpy variations. The model is however largely enriched, extensively using mapped values, in order to derive a more precise and accurate physical behaviour. Performance correlation of the model has been studied in previous works on the same topic; correlation quality, in terms of affinity between the GT-Power simulation behaviour and that of the real engine, being run on test-bank, is given for reference [30].

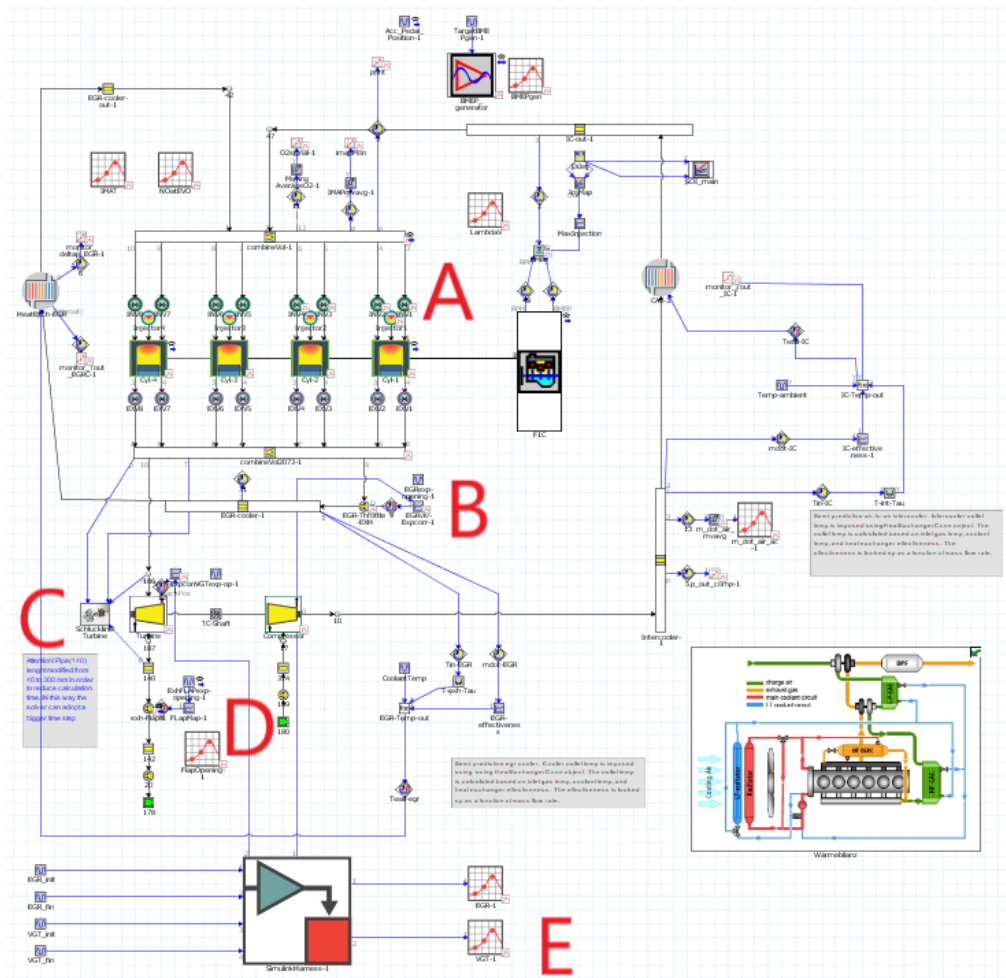


Figure 2.4: GT-Power environment engine modelling

2.5 SimuLink coupling

Engine control logic and actuators control logics are built in SimuLink environment, being the software widely adopted both in OEMs and in automotive control systems development in general[1][5]. This allows for the usage of a variety of complex control algorithms and patterns, that can be easily exported to GT-Power via code generation, through a dedicated block that interconnects the two platforms. Within the workflow, the connection between the two environments takes place when a signal is requested and then sent from SimuLink to GT-Power. A Model-in-the-Loop (MiL) procedure has thus been followed to test the designed control logics.

Simulation environment offers two alternative ways to propagate signals from SimuLink to GT-Power and *viceversa*. A first one, the *run-from-SimuLink* block, enables the simulation run from SimuLink: this option is mostly chosen to launch single simulations and is used for parameters tuning, when extensive simulation on a single study case is needed.

The second alternative is the *run-from-GT* block; this latter option allows the execution of multiple different simulations in a row and can be used for extensive results collection, once the implemented simulation is deemed as trustworthy. Blocks are eventually illustrated in Figure 2.5.



Figure 2.5: Interface blocks for smimulations environments coupling; to the left, SimuLink-as-Lead interface block; to the right, GT-as-Lead one

SimuLink-as-Lead block is marked in ochre; GT-as-Lead block is indicated in violet. Both the blocks rely on the very same input-output signals.

Chapter 3

Engine Operating Points

This chapter focuses on the choice of Engine Operating Points (EOPs) along the modelling and identification work and the control of the engine. A method to choose the EOPs is presented, and more ways to properly choose a set of Control Engine Operating Points (CEOPs), starting from the previously chosen EOPs are described.

Engine control systems set a control action, *i.e.* the actuation signal needed to operate an actuator, according to the actual and/or desired engine state imposed by the driver through the pedal position. At a macroscopic level, the state of the engine is characterized in terms of engine speed and load. The load is usually associated to the injected fuel quantity or to the torque. For practical use, as well as simulation simplicity, the torque can be replaced by the *BMEP*. Each engine operating point is therefore uniquely identified by the following quantities.

- Engine speed, expressed in *rpm*, rounds per minute;
- Brake Mean Effective Pressure, or *BMEP*, expressed in *bar*.

BMEP is an effective quantity to compare relative potential of differently sized engines, as long as they run on the same sort of fuel. Such value is essentially the average pressure forcing down the pistons inside the cylinders, providing the measured torque output, therefore this term is also referenced as engine *load*.

3.1 Operating points selection

The following section investigates the choice of the EOPs, and the importance of their distribution across the map, in order to extract as representative as possible a discretization of the engine system.

Common vehicle engines are tested on a benchmark of ca. 100-400 stationary operating points, so as to collect a valid and exhaustive set of data. Such experiments are referred to as stationary, since along the test engine is not moved from its current state, defined by each single EOP. If needed, number of tests can go up to one thousand EOPs, depending on the engine type and usage. Among these points, a given amount of them is chosen, to

represent the engine behaviour over the whole speed and load ranges. Again, this number can vary considerably according to the engine type and performance requirements [28].

Starting point of the procedure is the engine baseline calibration, *i.e.* the steady-state set of points that define engine behaviour. In this work, the baseline engine map comprises 126 points that have been assessed at the test bed within the premises of Politecnico di Torino. EOPs set is shown in Figure 3.1.

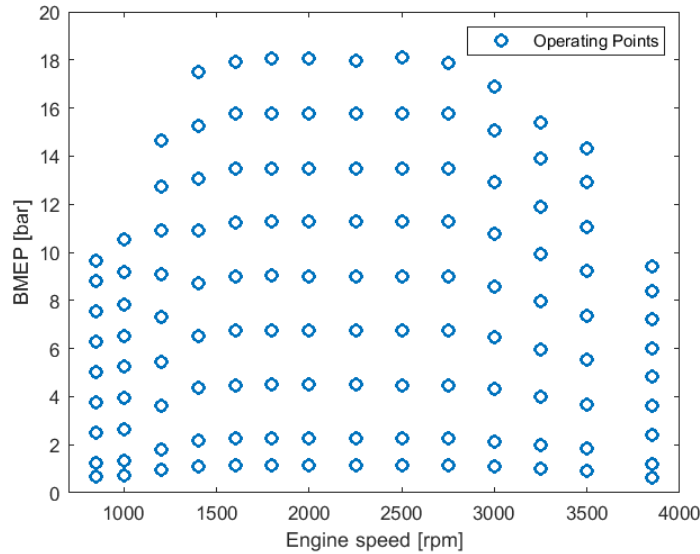


Figure 3.1: The 126 tested EOPs

Among these points, only some of them are chosen as candidates as the engine control logic pillars. To this extent, particular attention is paid in equally spacing the points, as well as in excluding specific map areas, as here described.

- Full load curve, thus upper engine operating curve is avoided. Its points are considered as edge cases and are therefore examined only as a particular operating condition, not discussed in this work.
- Points below 2 *bar* are excluded, the reason for this being they are rarely visited in real engine cycles and their relatively lower importance for identification purposes.
- A limited amount of points in the low engine speed, low *BMEP* region is chosen, needing them to be treated separately as part of the idle speed control system, or with dedicated strategies.

Remaining engine map area is subdivided in twenty subregions, that are regularly spaced across the engine map, each 650 *rpm* and each 3.75 *bar*. Engine behaviour is not expected to vary significantly in such intervals; besides, dealing with a limited amount of EOPs makes the identification and control issue more tractable. A point per each of interval is

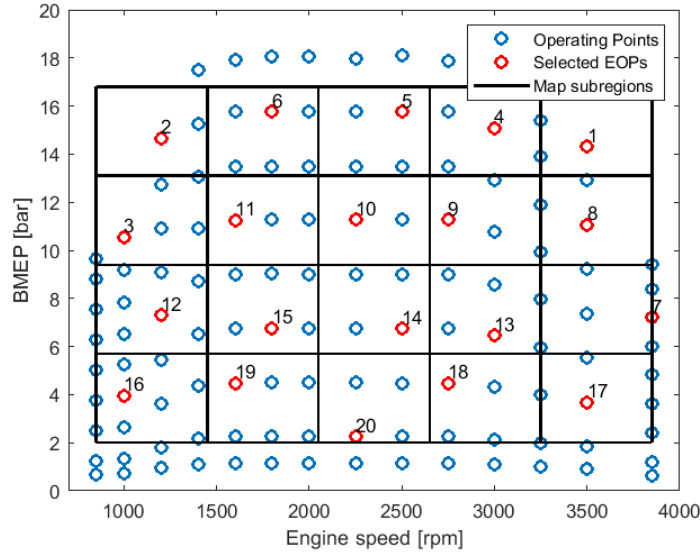


Figure 3.2: Selected EOPs, in red, with highlighted twenty subregions subdivision. Numbering of the selected EOPs is shown

chosen, according to the previous requirements. Outcome is shown in Figure 3.2, where the numbering of the EOPs that is going to be followed throughout the dissertation is given.

Figure 3.2 highlights the *ratio* followed to partition the engine map. Apart from selecting one point per each interval, an attempt has been made to select points so that they are not perfectly aligned on x or y axes. Point at 3850 *rpm* and 7.21 *bar* is on the edge of a map subregion so as not to be aligned with its upper and lower neighbors, already at 3500 *rpm*.

Further five additional points, lying on the outside of the region defined in Section 3.1, are described. Their study is performed for the sake of completeness, since the engine ECU, through either fuses or PTOs (Protection Thermal Overload) may already detect the points and take the necessary countermeasures, so as not to damage the engine components. This topic largely refers to states leading to high in-cylinder pressure or high engine speeds. A second set of points is chosen in the low *BMEP* low engine speed area, to define engine behaviour when close to idling. Again, these points are not considered for control purposes as a dedicated control logic spots the idling occurrence, that consequently weighs the opening and closing of EGR and VGT valves. Outcome of an identification process does indeed bring results that are comparable to that of EOP n. 16, illustrated in Section 7.2.

3.2 Operating points recognition

Engine operating point recognition comes in handy when targeting the control logic for a specific engine running situation: given input engine speed and *BMEP*, that are in turn

dependent on the accelerator pedal position, given by the driver, an operating point among the twenty selected ones is chosen. This procedure is done thanks to an engine mapping, that is integrated within SimuLink. The EOP choice is performed minimising the distance between the current point and the twenty selected EOPs. Given the different measurement units and order of magnitude of engine speed and $BMEP$, the two engine map axes, as well as the current engine rpm and $BMEP$ parameters, are normalized: this allows for an equal weighing of the distance of the current engine point, to the two quantities defining the engine map. A first example of EOP recognition on a sample engine point is given in Figure 3.3, where the current engine state is shown. The current engine state does not correspond, in general, to any of the twenty EOPs and can lay anywhere on the engine map. Core strength of the map is to trace the current engine state back to an EOP, whose corresponding airpath mathematical model, that operates in that region, is known.

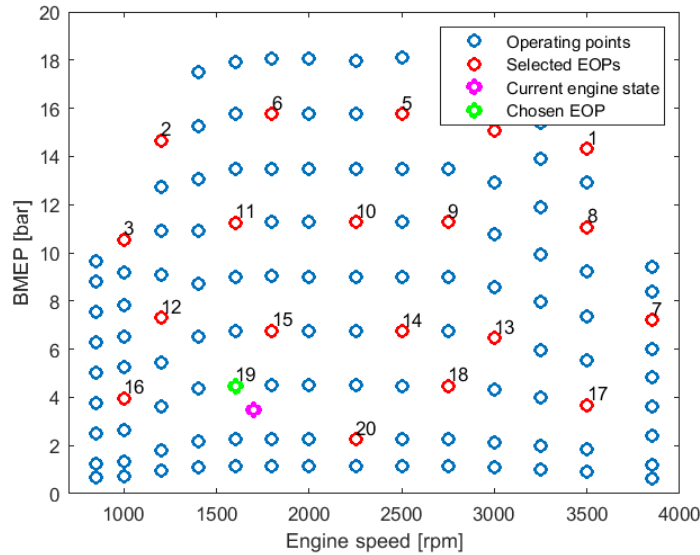


Figure 3.3: EOP recognition, $engine\ speed = 1400\ rpm$, $BMEP = 3.5\ bar$

3.2.1 Mapping for control purposes

This brief subsection illustrates how the described principles of this chapter are practically included into simulation environment. This is performed via GT-SimuLink coupling, already introduced in Section 2.5. The engine map assigning any engine current state to a tailored control action is built through a MatLab function, where equally spaced engine speed and $BMEP$ are fed, so as to link each of them to a specific EOP. A correlation of each point of the map to an EOP is then obtained and the outcome of such algorithm is eventually represented through a block in SimuLink environment. Bridging SimuLink with GT-Power simulation, the engine speed and $BMEP$ coming from the GT can access SimuLink and enter the map, producing as output the case number, that will correspond to a tailored model-based control for the current engine state. Graphical representation of the process can be seen in Figure 3.4

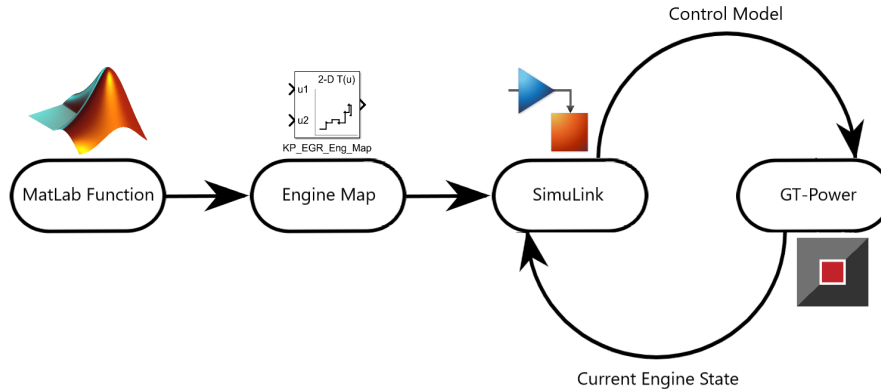


Figure 3.4: Engine map design and usage through GT-Power - SimuLink coupling

3.3 Control points association

Out of the twenty selected EOPs, many of them are likely to share noticeably similar physical behaviours and, thus, mathematical models, as it will be described in Section 5.1. From this arises the necessity to screen the set of EOPs, so that no redundant model descriptions occur when characterising the airpath behaviour. The screened remaining points are subsequently used to build on them the valve controllers and are therefore referred to as the subset of the Control Engine Operating Points, or CEOPs. This section stems from the need to recognise, from time to time, what the closest CEOP is to the current engine state.

However providing a comprehensive insight into control operating points and their selection in Chapter 5, it is deemed as necessary to introduce here the algorithm that associates the current engine state to a $CEOP_j$. This helps the reader having a full comprehension of the engine mapping procedure, that is essential to in turn thoroughly comprehend the following chapters.

The problem of choosing the best CEOP, given an engine state and, so, a couple *engine speed-load*, adds a new degree of complexity in the EOP choice. To better focus on this, key issues and logic flow of the studied problem is given.

- Engine is in a given state, characterised by a couple (ω_c, p_c) of engine speed and *BMEP*.
- Each EOP_i is univocally associated and replaced, because of model affinity, with a corresponding $CEOP_j$.
- Current state (ω_c, p_c) has to be associated to a $CEOP_j$ among the set of twelve CEOPs, so as to provide the system with a tailored control logic.

The problem, as outlined in the bullet points, is now tackled via three different solutions, namely the CEOPs association based on *vicinity* between current engine state and the CEOPs, the association based on *affinity* between current engine state and the CEOPs and a further associative method, defined via *k-means clustering* technique. The three methodologies are illustrated in the next subsections.

3.3.1 Vicinity mapping

Most fitting $CEOP_j$ recognition, given current engine state, is initially performed in the exact same way as in Section 3.2, however with the smaller CEOPs set. Assignment procedure is based on the euclidean distance between the current engine state to the twelve CEOPs. The CEOP with the smallest distance from the current state is chosen to represent it. For this reason, this process is named *vicinity* mapping.

A simulation performed on a set of twelve chosen CEOPs, among the starting twenty EOPs is proposed in Figure 3.5. The Figure describes the assignment of each point of the engine map to each control operating point.

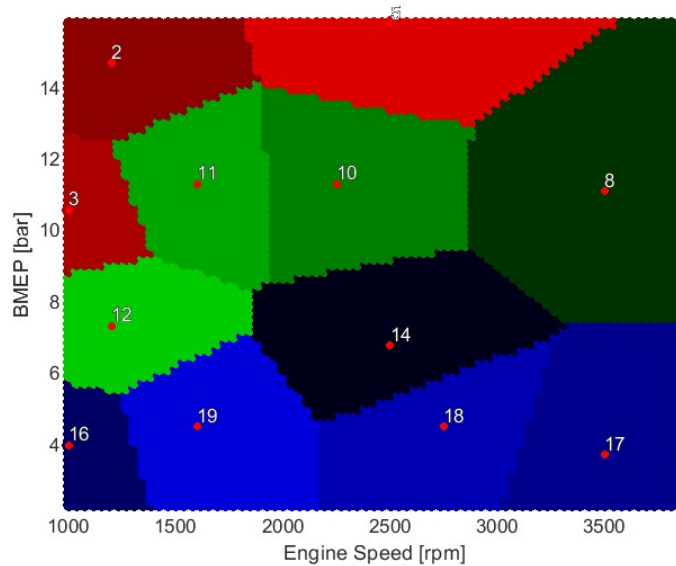


Figure 3.5: CEOPs recognition, *engine speed* and *BMEP* values uniformly spanned across engine map, using *vicinity* mapping. CEOPs are numbered following same numbering of EOPs.

From Figure 3.5, it is evident that engine map is subdivided through lines that are equidistant from two different control points. When the engine current state falls inside a given coloured region, it is assigned to the CEOP that is in the centre of that region.

3.3.2 Affinity mapping

The direct link of the current engine state to the closest $CEOP_j$ among the CEOPs set, as described in *vicinity mapping* is, however, not always fully satisfactory. Indeed, this may

force unintended associations of the current engine state to a $CEOP_j$ whose model is not adequate to describe the current engine dynamics.

This situation occurs when, for vicinity reasons, the current engine state (ω_c, p_c) is associated to a $CEOP_j$, because the association to its corresponding EOP_i is no longer possible, as this has been removed and replaced by another $CEOP_k$, whose mathematical model is similar. The generated inaccuracy is treating the current engine state with a control model, the one of $CEOP_j$, that is not the best one to describe that specific couple (ω_c, p_c) . Most descriptive model for that current engine state would in that case be $CEOP_k$. The situation is visually described in Figure 3.6.

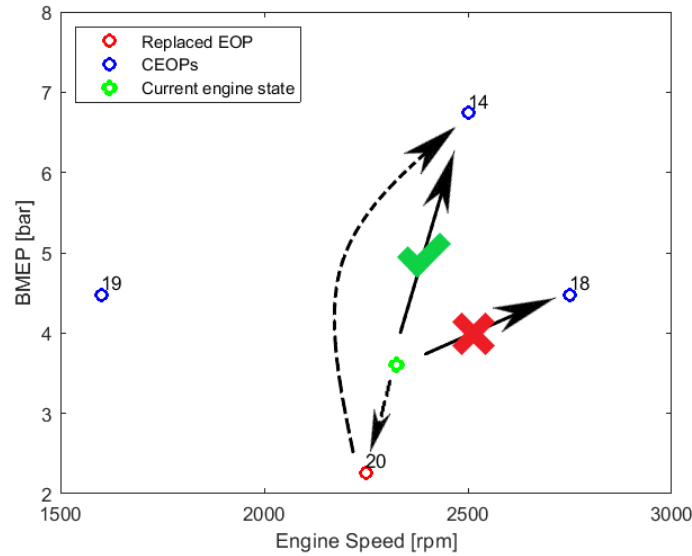


Figure 3.6: Assignment of the current engine state (ω_c, p_c) , in green, to a CEOP that is not the closest, following an *affinity* principle

In Figure 3.6 the current engine state is assigned to $CEOP_{14}$, however being closer to $CEOP_{18}$. This happens because EOP_{20} , the closest point to the current engine state, is replaced, for affinity reasons, with $CEOP_{14}$. The current engine state should therefore be treated not with the control law of the *closest* CEOP, but with the CEOP that *replaced* the original discarded EOP_{20} .

This process will be referred to as *affinity mapping*. Followed algorithm is below schematized; method can be divided essentially in two steps.

- Step 1: (ω_c, p_c) is assigned to the closest EOP_i out of the original twenty EOPs set.
- Step 2a: if assigned EOP_i has been discarded and replaced by a different $CEOP_k$, another assignment procedure is performed, this time within the CEOPs subset. The euclidean distance of (ω_c, p_c) to the $CEOP_k$ that replaced EOP_i found in Step 1 is decreased by a given factor; at this point, closest CEOP is chosen.
- Step 2b: if assigned EOP_i has not been discarded, its $CEOP_i$ is directly chosen.

The described procedure outcome is graphically reported in mapping in Figure 3.7. To obtain the mapping, a divisive factor $d = 1.4$ has been used to compute the distance of the current state from the replacing $CEOP_k$. This means that, once computing the distances of the current state from all the CEOPs, the distance to the $CEOP_k$ replacing the closest original EOP_i is divided by a factor 1.4. The value of the divisive factor d is chosen in an iterative way, so as to provide a sufficient differentiation from *vicinity mapping* algorithm, at the same time not exasperating the *affinity* current state-CEOP matching.

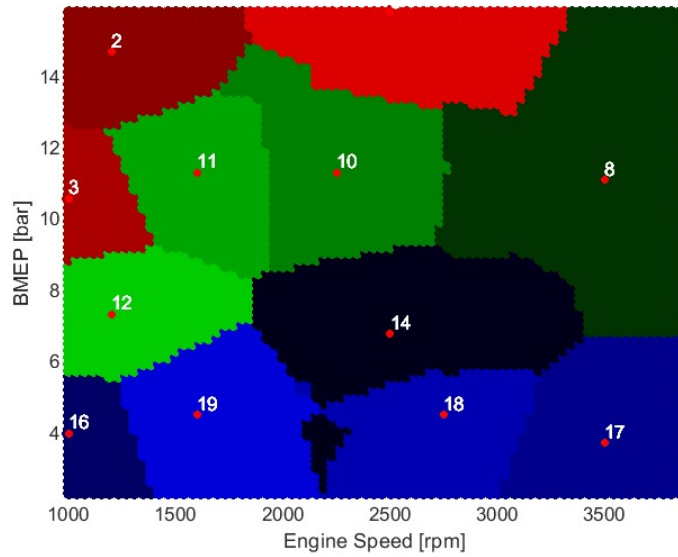


Figure 3.7: CEOPs recognition, *engine speed* and *BMEP* values uniformly spanned across engine map, improved method

Figure 3.7 shows how frontier cases between one CEOP and the other are differently treated, depending on the way the replacement between original EOPs and CEOPs subsets has been performed. The introduced nonlinear frontiers between one CEOP and the other should be helpful in giving each engine current state the most fitting control model, depending on its affinity to an EOP or the other. Examples of the assignment of an area to a zone or the other is the region between 2000 and 2500 *rpm*, per 4 *bar*, where an assignment to the upper $CEOP_{14}$ is performed, however the region being geometrically closer to $CEOP_{18}$ and $CEOP_{19}$, to its right and to its left. Former discarded EOP laying in that area had been, indeed, replaced by the upper $CEOP_{14}$.

In Section 7.1 a comparison in terms of control tracking performance between *vicinity* and *affinity mapping* is made, revealing that the latter mapping has an edge over the standard one in terms of tracking speed and yields, in specific situations, a more consistent response.

3.3.3 K-means clustering

An alternative way to perform a screening and mapping between the twenty selected EOPs and their corresponding CEOPs is here proposed. The technique, *k-means clustering*, is based on affinities between characteristic traits of each EOP. These characteristic features are the outcomes of identification process carried on in Chapter 4. Identification process associates to every EOP a transfer function, a mathematical model linking an input - the valve actuation - to an output, being the specific target variables. Shape in terms of zeros, poles and gain of the transfer functions is considered as input of the clustering algorithm.

K-means clustering is, consequentially, applied to the twenty corresponding identified state-space models of the EOPs. The principle upon which k-means clustering runs is that of *unsupervised learning*. Algorithm splits the EOPs set into smaller groups, without needing any *a priori* labelling of the EOPs. The algorithm can be essentially divided into two iteratively repeated refinement steps, here described.

- Data assignment step, during which each datum is assigned to a centroid, basing on its euclidean distance to all of them. Point is assigned to the centroid from which distance is minimum.
- Centroid update step, a re-computation of the centroids is performed, so that the overall distance of the centroids from all the data is as low as possible: centroids are therefore chosen as the barycentres of the newly defined clusters.

The two steps are repeated until either a maximum number of iterations is reached, or the algorithm reaches convergence, thus the centroids update step gives no more noticeable changes from one iteration to the other.

The algorithm, taking as input only the EOP models data and the number of clusters to operate with, is then applied. Fed data are zeros, poles and gain of the twenty state-space models. Imaginary roots are taken as their modulus and a further indicator is added, to remind that this has been done. No corresponding damping is considered, being the model with imaginary roots only one.

Lastly, clustering is repeated for a given number of times (Fig. 3.8), due to the random choice of the initial centroids. The outcome of such tests is a links matrix A_{links} , where each $A_{links\ i,j}$ element corresponds to the times EOP_i has been clustered together with EOP_j , out of the total performed iterations of the algorithm. The matrix, divided by nine, is an effective tool to see, on average, how many times two EOPs have been clustered together (Fig. 3.9). A_{links} is then filtered, its non-empty elements being progressively decreased by one, until there is only twelve links remaining, while the rest of the matrix is zero. At that point, results are plotted (Fig. 3.10) and CEOPs are manually chosen basing on the graph. CEOPs choice is performed selecting, when possible, EOPs sharing the most links with the others of the same cluster and then trying to maintain an equally spaced CEOPs presence. EOPs that share no links are always chosen as CEOPs.

An overview of k-means algorithm application, on the EOPs set, is given in Figure 3.8, 3.9 and 3.10, starting from a set of $n = 9$ tests, each starting from a random initial centroids selection, and asking for a subdivision into twelve clusters.

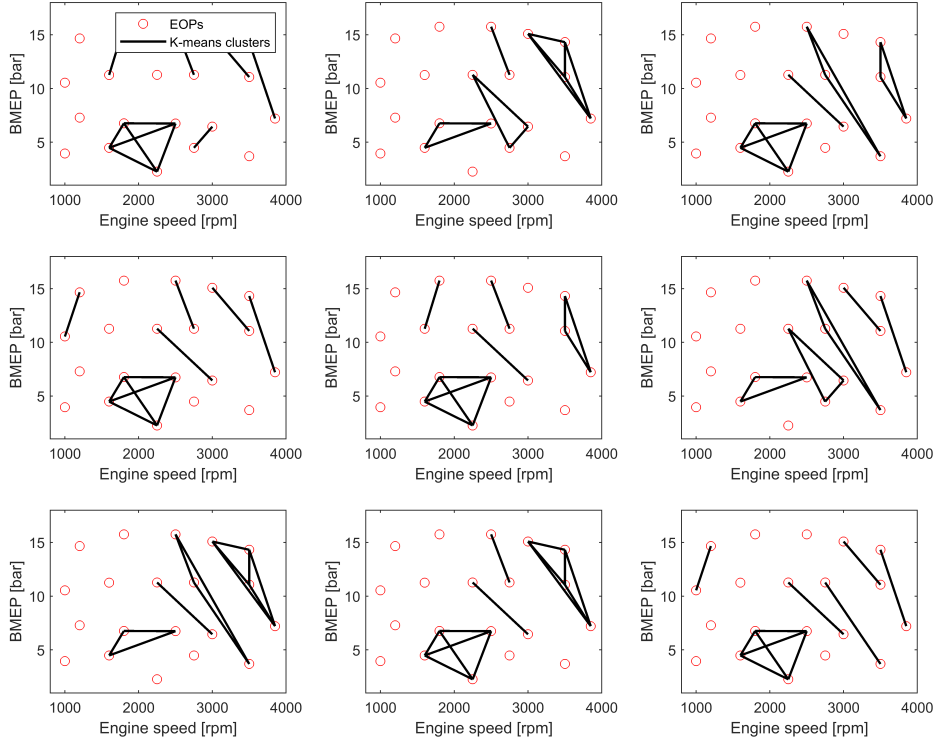


Figure 3.8: K-means clustering different outcomes, with $k = 12$ clusters, applied $n = 9$ times, with different initial centroids guesses. EOPs connected by black lines belong to the same cluster

From Figure 3.8 it is possible to observe how the different initial centroid guesses affect the final clustering outcome; in spite of this, specific patterns are still recognizable, an example being the set of clustered points marked with letter "A" in the high $BMEP$ - high engine speed area, or the one at low $BMEP$ - medium engine speed, marked with "C". Points to the left, corresponding to low engine speed region, marked with "B", are mostly separated and not clustered between themselves, however being close one to the other. Physical reasons for this are provided in Chapter 7.

Figure 3.9, an average between the nine previous outcomes, helps understanding what points have been clustered together more often, indicating there is a higher degree of similarity between their respective models. New feature, with respect to *vicinity* and *affinity mapping*, is that here CEOPs association is done considering *only* model similarity, thus without any spatial knowledge on the position of the operating points.

Final Figure, 3.10, filters Figure 3.9, with a view to highlighting what the effective chosen CEOPs are. Eventual outcome of the cluster is not far from the division proposed

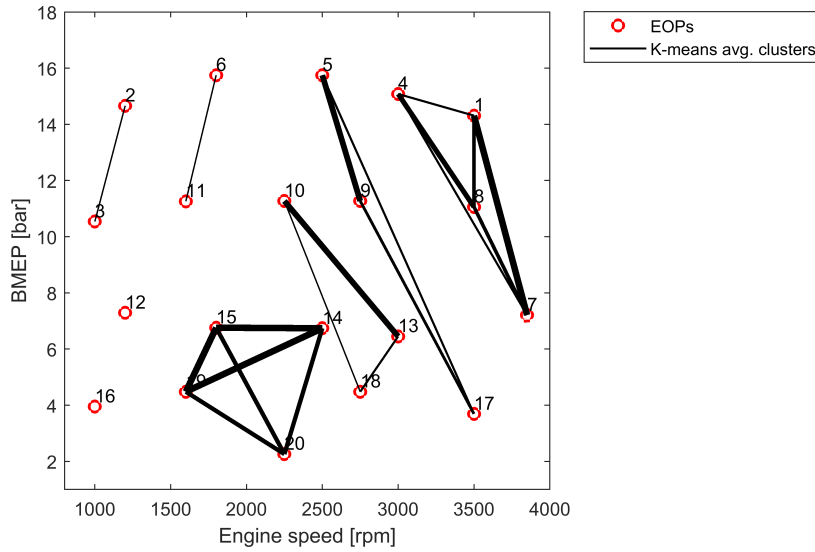


Figure 3.9: Average of k-means clustering nine outcomes with different initial centroids guesses. Thicker lines indicate two EOPs are more prone to belong to same cluster

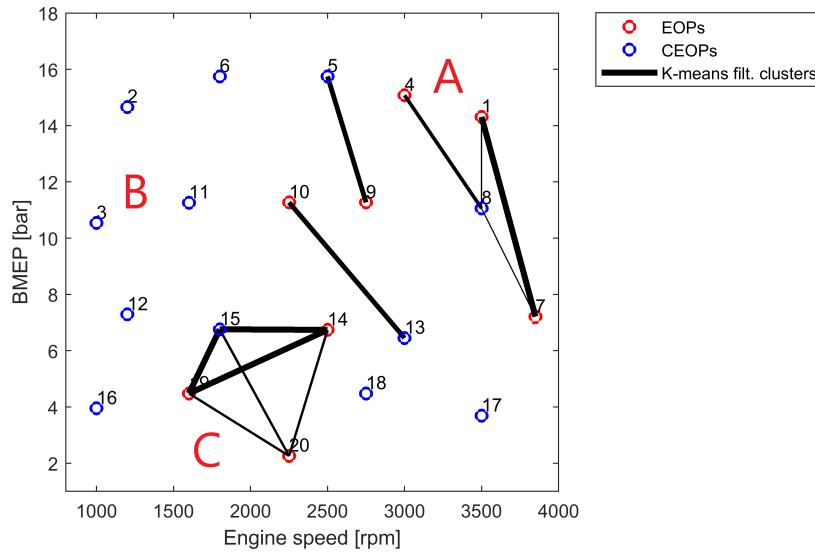


Figure 3.10: Average of k-means clustering outcomes with different initial centroids guesses, filtered to obtain exactly twelve CEOPs. Thicker lines indicate two EOPs are more prone to belong to same cluster. Blue points represent a possible CEOPs choice and capital letters indicate main interest areas

in Section 5.1 and introduces a further insight on their selection, as in this case the CEOPs decision is *unsupervised*, thus only demanded to a mathematical procedure.

A second test has been carried out, with a view to noting if clustering would change when adding to the EOPs features a further indicator, being the engine speed and $BMEP$ of the examined point. Inputs to the clustering algorithm are, hence, both zeros, poles and gain of the model and the point (ω, p) where the model has been obtained. Each feature is equally weighted before starting the clustering algorithm and the quantities are normalized with respect to their maximum element. A contribution of $\frac{1}{3}$ is therefore given by the engine state (ω, p) . This encourages the clustering between *near* points, as well as affine ones, and can therefore be considered as an improvement of the previous algorithm, as now an eye on the physical meaning of the EOPs is kept. Results of this process can be seen in Figure 3.11.

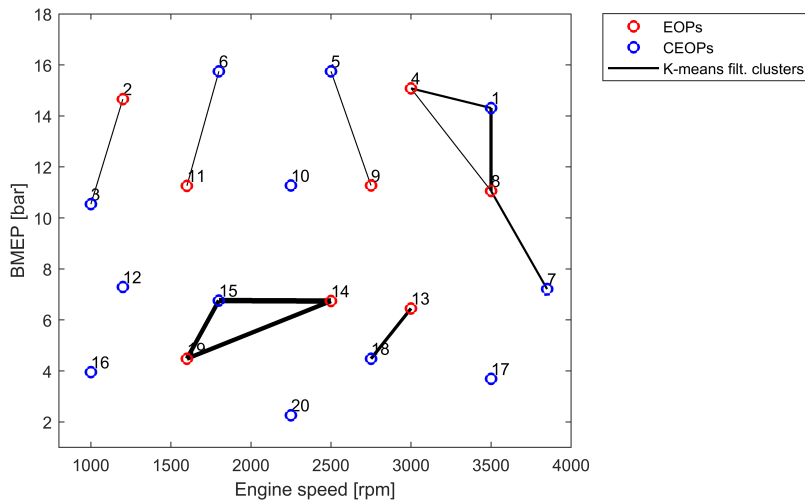


Figure 3.11: Average of k-means clustering nine outcomes with different initial centroids guesses, filtered so as to obtain exactly twelve CEOPs. EOPs vicinity is taken into account in clustering process and thicker lines indicate two EOPs are more prone to belong to same cluster. Blue points represent a possible CEOPs choice

Figure 3.11 demonstrates that, when vicinity between EOPs is considered, a more similar outcome to that of the control points recognition is obtained.

3.4 Results analogies and purpose

EOPs identified in Figure 3.2 are used for identification purposes in Chapter 4. Core idea is that, thanks to the peculiar subdivision into equally spaced subregions, identification will develop models whose characteristics vary regularly from one region to the other.

Concerning the further selection of a subset of CEOPs, to be use throughout the development of a control logic, the three presented methods, *vicinity mapping*, *affinity mapping* and *k-means clustering*, offer valuable alternatives to partition the engine map into regions where engine behaves similarly. *Vicinity mapping* is the most standardized algorithm; it is

based on the assumption that, if two engine states are close in terms of engine speed and load, they behave similarly. Engine mapping for control purposes is easy and immediate. *Affinity mapping* is an extension of the previous concept and it encloses the possibility to refer the current engine state to a control law that is *better*, however not the *closest* one. Last given example is based on *k-means clustering*. This idea aims at assigning the current engine state to a control law, basing on an unsupervised map partitioning technique, defined from affinity between engine models.

The process of partitioning the engine map is crucial, with a view to choosing the most fitting control action to any engine state, henceforth improving overall control performance. This matter is specifically brought on in Chapters 5 and 7.

Further developments on this topic may be pursued, especially by looking at tracking control performances when switching from one mapping to the other. Relying on the clustering outcome rather than on *vicinity* or *affinity mapping* and making a comparison between the different tracking performances is an additional and yet to be tested step.

Chapter 4

System Identification

4.1 The identification variables

Scope of this part of the thesis work is to understand the behaviour of the system outputs depending on the given control inputs, being the EGR and VGT valve positions. A thorough system identification will enable, in the next steps, the proper control of the system dynamics.

As mentioned in Chapter 1, the two considered engine airpath inputs are

- Exhaust Gas Re-circulation (EGR) valve position, expressed in opening percentage;
- Variable Geometry Turbocharger (VGT) rack position, again expressed as opening percentage.

Two output quantities are measured; their value is obtained thanks to monitors in GT-Power environment:

- $IMAP$, intake manifold pressure;
- \dot{m}_{air} , air mass flow rate in intake manifold.

A third variable, O_2 percentage concentration inside intake manifold, is also collected, being proportional to NOx emissions.

System identification will proceed on parallel tracks, considering the EGR and VGT dynamics as decoupled one from the other; the identified model is going to be, in this case, linear. As in reality the two dynamics do intertwine themselves, this being a direct consequence of their acting on the very same fluids, non-linearities emerge, and must be tackled so as to better fit a control action. The application of filters, as well as other techniques to deal with this issue will be tackled in Chapters 5 and 6.

Specifically, a first identification process is performed considering a Single Input Single Output, or SISO system, whose input is, at turn, EGR and VGT valve position. When system input is EGR, the measured output is \dot{m}_{air} . Opposedly, when system input is VGT

valve, the considered output is *IMAP*. The identification process is performed on all the engine operating points defined in Chapter 3, Figure 3.2. In this dissertation, for the sake of simplicity, only four points will be reported and fully commented. The four points are chosen so that they represent a spectrum of engine conditions that is as wide as possible.

4.2 Step testing

The first section of the identification process is aimed at defining the amplitude of the steps to be given to the two considered valves, EGR and VGT positions.

Key idea is that, if the output dynamic is not sufficiently excited, then the system is identified as unresponsive to the input variable change. *Viceversa*, if the output dynamic is overexcited, this can result in a nonlinear behaviour, that is not fitted adequately by the identified models.

From this comes the importance of the exploitation of the variation range of EGR/VGT aperture to which a linearly varying output target quantity corresponds. In other words, the identification output must vary within a linear range when stimulated by an input variation. These preliminary identification requirements are well in accord with previous studies on the same topic [2][15][16][23]. A last fundamental step that gives robustness to the whole identification process is the usage of an upper and a lower threshold for the actuators positions that are centered in the target EGR and VGT mapped values, selected directly by the engine ECU and measured during on-bank test phase. This is particularly important, so as to be sure to effectively lie within the *linearity* range between input and output.

Step testing process is carried out on GT-Suite environment, on the exact same engine plant that has been defined in Chapter chapter 3; here, signals are generated by a tailored SimuLink scheme, that is depicted in Figure 4.1. An input step, whose initial and final value will be iteratively modified, is sent to the engine valves, and output signals variations are collected. Aim of this section is to tune the lower and upper (or *initial* and *final*) values of the input signals, to obtain a noticeable, however not excessive, variation of the target output quantities. Such variation must lay within 5 and 10%, and is defined as in Equation 4.2

$$\delta = \frac{y_{fin} - y_{in}}{y_{in}} \cdot 100$$

(4.1)

where y represents the time-to-time considered output value.

As it is possible to see from Figure 4.1, the signal initial and final values are chosen by the user acting on GT-Power variables, and are therefore rapidly modifiable, without

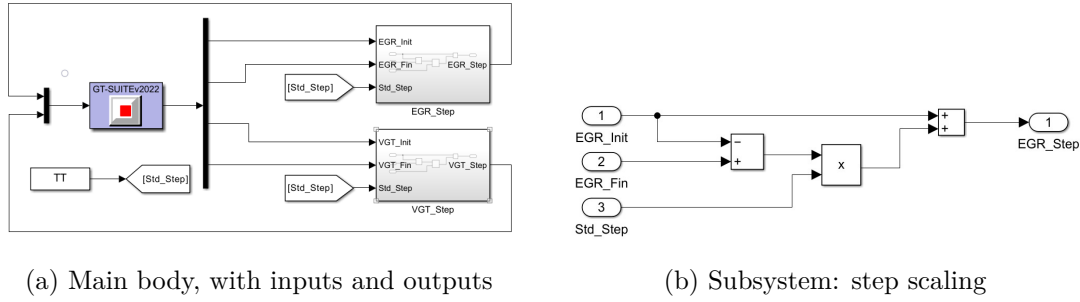


Figure 4.1: SimuLink standardized step signal generation

having to regenerate the SimuLink code whenever the input amplitude is changed. The step given by SimuLink is given after 15 s, and lasts 60 s, so as to be sure the system reaches a steady state, both before and after the step is given. A schematic representation of the given step is provided in Figure 4.2. At this point, the cases are sequentially run on GT-Power environment and results are collected. If the variations on output values are either too small or too big, the test is discarded and, respectively, a higher or lower variation of the control variable is input. At the end of the procedure, the proper values of EGR and VGT positions are stored in a table, and their values will be used in the next section: the real system identification of the engine parameters.

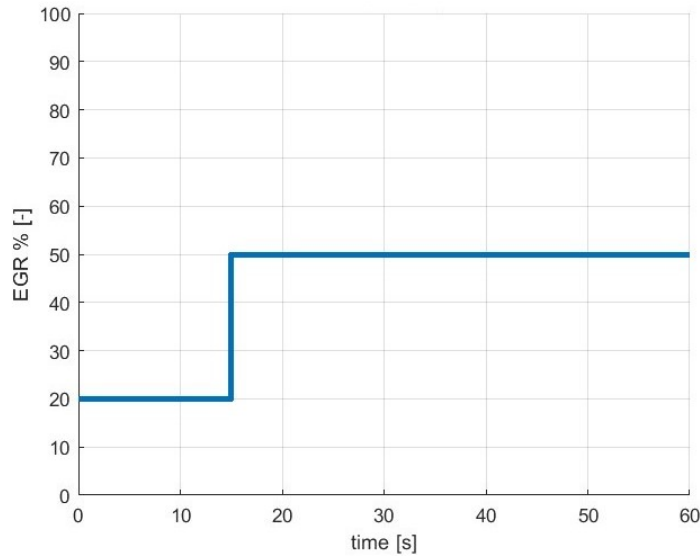


Figure 4.2: An EGR sample step test, EGR valve opens from 20 to 50% of its total size

The tests outcome is reported in Tables 4.1 and 4.2, where every engine case is listed, highlighting the engine speed, the *BMEP*, the actuators initial and final positions and the percentage δ between initial and final value of the output target variables, once the steady state is reached. For the sake of simplicity, output percentage deltas have been accepted when in the 5 to 15% range, thus slightly enlarging the previously imposed constraint. The

EGR values that leveraged over the most \dot{m}_{air} values range from 10 to 40% opened valve. A corresponding situation is found in VGT case, with VGT rack opening from 80% to 100%. As in the previous case, variations between 5 and 14% in the *IMAP* boost pressure have been deemed as satisfying. Such assessment is performed only on the output variable, that is related to the input control action.

Edge cases have not been strictly considered in this phase, as the identification process is not to be carried on them, as they often feature nonlinear behaviours and engine integrity problems; indeed, these critical cases need a tailored control logic, that is discussed later on.

| EOP | $EngSp$ [rpm] | $BMEP$ [bar] | EGR_i | EGR_f | $\Delta\dot{m}_{air}$ [%] |
|-----|---------------|--------------|---------|---------|---------------------------|
| 1 | 3500 | 14.31 | 5 | 25 | 11.43 |
| 2 | 1200 | 14.66 | 0.01 | 20 | 15.20 |
| 3 | 1000 | 10.54 | 0.01 | 20 | 10.70 |
| 4 | 3000 | 15.08 | 10 | 20 | 6.50 |
| 5 | 2500 | 15.75 | 10 | 40 | 11.39 |
| 6 | 1800 | 15.75 | 20 | 40 | 9.72 |
| 7 | 3850 | 7.21 | 5 | 20 | 9.78 |
| 8 | 3500 | 11.06 | 10 | 20 | 6.64 |
| 9 | 2750 | 11.27 | 20 | 40 | 8.67 |
| 10 | 2250 | 11.27 | 20 | 40 | 8.24 |
| 11 | 1600 | 11.26 | 20 | 35 | 7.30 |
| 12 | 1200 | 7.29 | 15 | 30 | 9.60 |
| 13 | 3000 | 6.45 | 25 | 40 | 7.19 |
| 14 | 2500 | 6.74 | 25 | 50 | 9.29 |
| 15 | 1800 | 6.76 | 25 | 50 | 11.92 |
| 16 | 1000 | 3.95 | 50 | 75 | 11.49 |
| 17 | 3500 | 3.69 | 10 | 20 | 7.66 |
| 18 | 2750 | 4.48 | 25 | 50 | 10.84 |
| 19 | 1600 | 4.48 | 30 | 60 | 11.11 |
| 20 | 2250 | 2.26 | 40 | 80 | 8.58 |

Table 4.1: EGR step test outputs variation assessment

Tables 4.1 and 4.2 show that, within given limits, an adequate variation range of the output signal can be ensured by properly tuning the validation signal. The higher or lower variability of the output at specific engine states is going to be addressed through the gain-scheduling control, that will be presented and discussed in Chapter 7.

| EOP | $EngSp$ [rpm] | $BMEP$ [bar] | VGT_i | VGT_f | $\Delta IMAP$ [%] |
|-----|---------------|--------------|---------|---------|-------------------|
| 1 | 3500 | 14.31 | 60 | 75 | 9.07 |
| 2 | 1200 | 14.66 | 75 | 100 | 14.11 |
| 3 | 1000 | 10.54 | 50 | 100 | 13.12 |
| 4 | 3000 | 15.08 | 65 | 80 | 8.52 |
| 5 | 2500 | 15.75 | 80 | 90 | 6.82 |
| 6 | 1800 | 15.75 | 85 | 100 | 13.79 |
| 7 | 3850 | 7.21 | 50 | 65 | 9.46 |
| 8 | 3500 | 11.06 | 60 | 75 | 9.58 |
| 9 | 2750 | 11.27 | 80 | 95 | 10.95 |
| 10 | 2250 | 11.27 | 80 | 100 | 6.11 |
| 11 | 1600 | 11.26 | 85 | 100 | 11.68 |
| 12 | 1200 | 7.29 | 50 | 100 | 10.54 |
| 13 | 3000 | 6.45 | 75 | 90 | 9.15 |
| 14 | 2500 | 6.74 | 80 | 100 | 11.61 |
| 15 | 1800 | 6.76 | 75 | 100 | 9.45 |
| 16 | 1000 | 3.95 | 20 | 100 | 5.70 |
| 17 | 3500 | 3.69 | 55 | 75 | 10.90 |
| 18 | 2750 | 4.48 | 70 | 95 | 13.47 |
| 19 | 1600 | 4.48 | 75 | 100 | 5.68 |
| 20 | 2250 | 2.26 | 50 | 100 | 9.71 |

Table 4.2: VGT step test outputs variation assessment

4.3 The identification signal

In this section, the development of a proper identification signal, that is able to entail the needed input variability, is discussed.

Signal is named PRBS, or Pseudo-Random Binary Signal, as it switches between two main values with pseudo-randomly varying periods; its requirements, characterising the whole model creation, are the following ones:

- Signal shape, series of step signals, with variable period/amplitude.
- Given period range, between 0.05 s and 20 s.
- Given amplitude range, not exceeding the values defined in Section 4.2 for each EOP.
- Sufficient settling time, set to 20 s, starting from benchmark mapped valve position.
- Signal must come back, for a given number of times, to the benchmark mapped value, so as to ease the manipulation of the identification signals: indeed, every time the signal comes back to the mapped value, the equivalent of a signal *reset* is performed, this enabling a clear division between signal intervals.
- Signal length, not exceeding 300 s.

Last requirement is due to several factors, two of which are particularly relevant. One of them is computation time, required by the machine to sequentially run each GT-Power simulation, lasting, both in reality and on computer, about 300s; the other is cost-related issues, considering that, in a successive stage, such tests should be performed on test bench. Cost of these experiments is in the range of hundreds of euros per testing hour. The signal, once again, is created in a normalized form, that is then scaled on GT-Power, depending on each engine operating point.

Procedure is carried on in MatLab environment, using the MatLab function *idinput*, that enables the user to create step series signals, with varying period: more signals with varying parameters are created and then joint together, so that the resulting final signal includes substeps whose period ranges from 0.05 s to 24 s. The period is in this case considered as the time distance between an ascent and a descent of the signal: this is justified by a practical observation on the physical system behaviour, that actually shows a response to that input sequence each time a step, either ascending or descending, occurs, and not just on *e.g.* ascents.

Identification signal creation process can essentially be divided into four steps, that are here listed.

- A normalized [0; 1] time varying signal is created through *idinput* function. At this step, periods become progressively longer.
- Step signals are reshuffled, so as to obtain a randomly varying period, rather than always ascending period steps. This is particularly advantageous for identification purposes, as it represents a more general study situation.
- Eventually, signals at the central mapped valve opening value are added, especially at the beginning of the signal, and inside other four pseudo-random time instants.
- Normalized signal is tuned depending on GT-Power requirements, via the dedicated SimuLink scheme already presented in Figure 4.1.

A graphical representation of the input signal is given in Figure 4.3. Here, a 1 corresponds to the valve upper threshold, a 0 to the valve lower threshold and, eventually, the 0.5 is converted into the benchmark mapped valve value within SimuLink environment.

The input sequence has then been fed into the GT-Power engine model. At this point, the twenty engine operating points are tested, once varying the EGR position and keeping the VGT valve fixed to a predefined value, *i.e.* the reference mapped one, then doing the opposite, varying the VGT valve position and keeping the EGR position constant. The same test is carried out, for the sake of completeness, with five edge cases that are briefly presented in Chapter 3; a total number of 50 tests is therefore performed and data are collected and stored, to be visualized afterwards. System identification on edge cases gives comparable results to those of models on the edges of the engine map, however more extreme. This latter testing has been functional in understanding the plant behaviour in extreme situations, as well as in providing a comparison to double-check the quality of the identified models of the twenty selected EOPs.

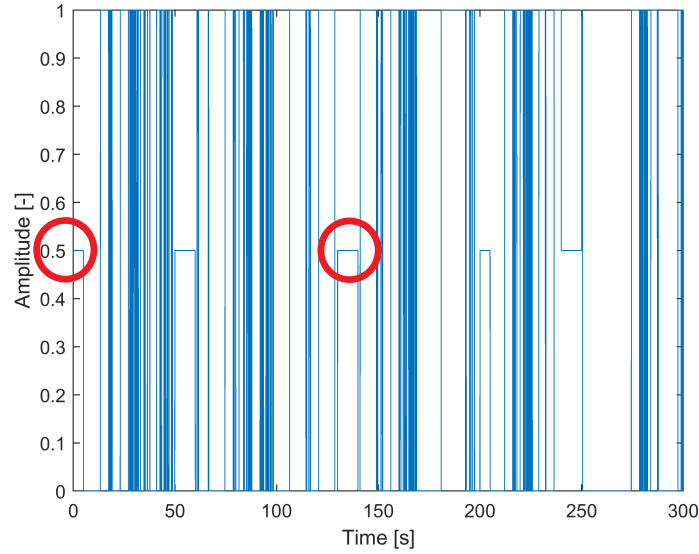


Figure 4.3: Normalized constant amplitude identification series; 1, 0.5 and 0 correspond to upper threshold, benchmark and lower threshold normalized valve position values. Starting value and a signal re-initialization are circled in red

4.4 Models overview

This section investigates the possible models used for identification purposes. Four model families will be presented and their strength and weaknesses are enlightened.

Mathematical models link the input, thus valve openings, to the output, either mass air flow or *IMAP*. Models take into account not only the input-output relation, but also an error interfering between the two signals. The development of specific mathematical functions to define how both the input-output relation and the error description work is what characterises the various used models.

4.4.1 The ARX model

First used model is ARX. The acronym, standing for AutoRegressive, with eXogenous inputs, describes a linear difference input-output relationship, where the noise is assumed to be a white noise and it enters the equation as a direct error. Model has been first developed by G. Box and G. Jenkins [32]; its equation can be described as

$$A(z)y(t) = B(z)u(t) + e(t). \quad (4.2)$$

In 4.2 the left-hand side is the autoregressive (AR) term and the input $u(t)$, multiplied by its corresponding polynomial, is the exogenous (X) part. Studied signals $y(t)$, $u(t)$ and $e(t)$

do depend on time, while $A(z)$ and $B(z)$ represent discrete polynomials; this aims to stress that the identification process is carried out on a discrete time domain, thus on z -plane. As it can be seen, no modification occurs to the error $e(t)$ structure, that is input without any pre-multiplying polynomial.

Polynomials $A(z)$ and $B(z)$ are characterised by two parameters, n_a and n_b , respectively representing their degree. Coefficients of these polynomials are the actual outcome of the identification process.

In the case $n_a = 0$ then $A(z) = k$, with k being a constant coefficient, the aforementioned model degenerates into a Finite Impulse Response, or FIR, model: ARX models are therefore already a generalization of a more simplistic model family. A proper transfer function $d\frac{B(z)}{A(z)}$, linking $y(t)$ to $u(t)$ is used during the identification procedure, thus $n_a \geq$. Graphical reference to the model is given in Figure 4.5.

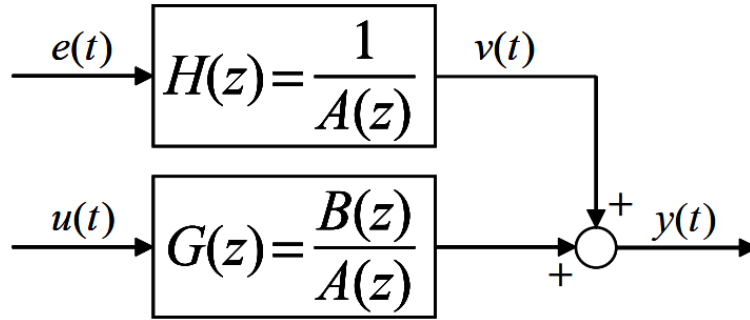


Figure 4.4: ARX model in simulation form. Credits [33]

4.4.2 The ARMAX model

Second proposed model is ARMAX. The acronym, standing for AutoRegressive, Moving-Average, eXogenous, is a direct evolution of the ARX model, where a further degree of freedom on the noise structure is added: now, the polynomial describing it is $C(z)$, that is in general different from 1. Model equation can be described as

$$A(z)y(t) = B(z)u(t) + C(z)e(t). \tag{4.3}$$

In 4.3 the polynomial $C(z)$ models the noise as a colored, *i.e.* correlated random variables, sequence. As it can be seen, no modification occurs to the other structures. Polynomials $A(z)$, $B(z)$ and $C(z)$ are here characterised by three parameters, being respectively n_a , n_b and n_c , that represent their degree. A proper transfer function $\frac{B(z)}{A(z)}$, linking $y(t)$ to $u(t)$ is used during the identification procedure, hence again $n_a \geq n_b$. Figure 4.5 presents the block scheme of the model.

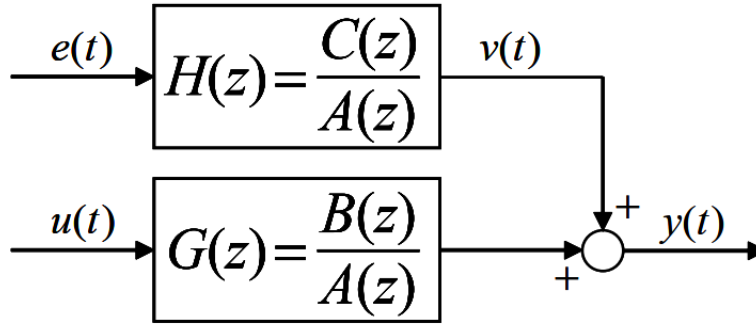


Figure 4.5: ARMAX model in simulation form. Credits [33]

4.4.3 The OE model

Last presented model of the same family is OE, or Output Error. Again, a linear difference input-output relationship is outlined, although here the noise is modelled as a white noise that is not disturbed in any way by the same transfer function affecting the input $u(t)$. Model equation is described as

$$y(t) = \frac{B(z)}{F(z)}u(t) + e(t). \quad (4.4)$$

The simpler structure of the model has to be noted; as it will be shown in Section 4.5, this will lead to the exclusion of the model from the identification process. Once more, polynomial $B(z)$ and $F(z)$ are characterised by two integers, n_b and n_f respectively, representing their degrees. Once more, a proper transfer function $\frac{B(z)}{F(z)}$, linking $y(t)$ to $u(t)$ is used during the identification procedure, so $n_f \geq n_b$. Model block scheme is shown in Figure 4.5.

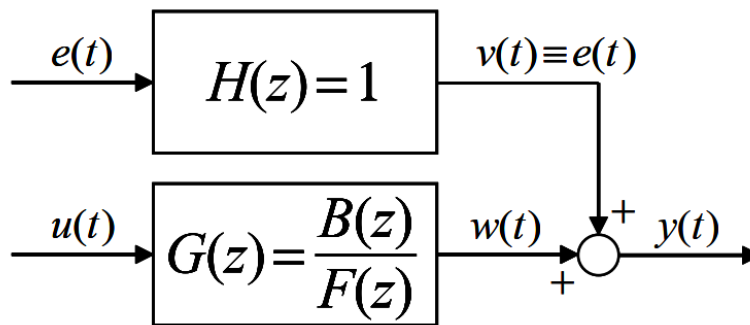


Figure 4.6: OE model in simulation form. Credits [33]

It is worth to mention that all the three described models are used in *simulation* form; simulation mode computes the model response using input data and initial conditions and is aimed at minimizing the simulation error, or *focus*. The technique is opposed to the

prediction form where, instead, model response is computed at some specified amount of time in the future using the current and past values of measured input and output values, as well as initial conditions.

On a macroscopic level, *prediction* form involves a real data feedback to build its model, while *simulation* form uses a simulated value of the system, thus relying on an internal feedback, that does not come from additional external data flowing into the identification.

Eventually, the *simulation* form identified model is targeted to capture system dynamics and is opposed to the *prediction* mode, whose main aim is to generate a model that is able to reduce the discrepancy between true $y(t)$ and predicted $\hat{y}(t)$ system output. The one-step prediction, $\hat{y}(t+1)$, based on the previous time samples is obtained feedbacking the known $y(1) \dots y(t)$ samples, and identifying a model based on them and on plant input $u(t)$.

Even though prediction form yields satisfying results when performing system identification, simulation form is tailored to provide the more perceptive approach, to understand how well the identified model performs under a wide range of operating conditions.

For the sake of comparison, the graphical schematic of *prediction* form procedure for an ARMAX model is given in Figure 4.7, with $H(z) = \frac{C(z)}{A(z)}$ and $G(z) = \frac{B(z)}{A(z)}$.

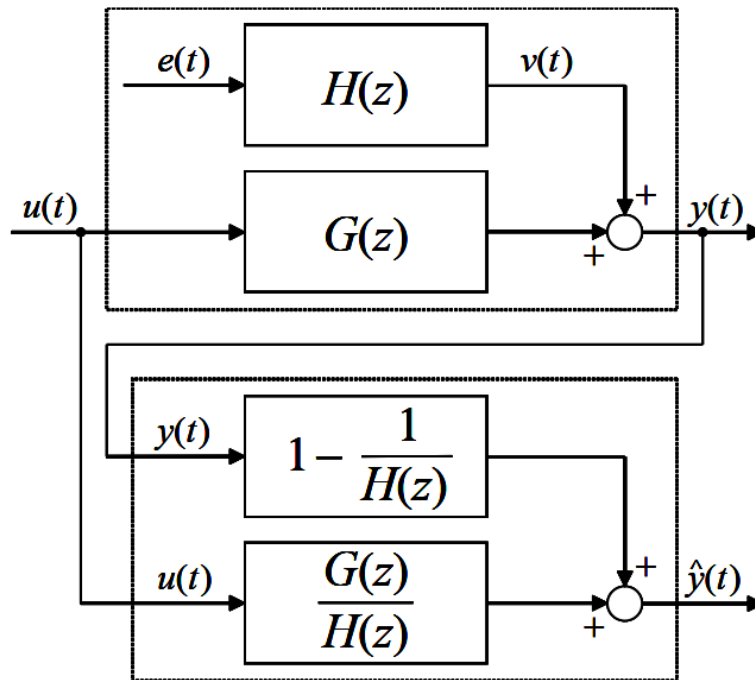


Figure 4.7: ARMAX model in prediction form (bottom part) and physical system (top part). Credits [33]

4.4.4 State-space model

Fourth model type that is considered is state-space representation: here, a set of inputs, outputs and disturbances are linked through first order differential equations, defining the state-space. Minimum number of state variables is generally equal to the order of the chosen differential equation to represent the system. Studied quantities are related between each other through five matrices, A , B , C , D , K , defining the system as the following one:

$$\begin{cases} \dot{x}(t) = Ax(t) + Bu(t) + Ke(t) \\ y(t) = Cx(t) + Du(t) + e(t) \end{cases} \quad (4.5)$$

From Equation 4.5 it is possible to see how error enters the model, being an output error when reaching $y(t)$, the output, and being manipulated by matrix K when entering the state variables. It is, moreover, necessary to remind that, here, the model design is performed on s -plane and not on z , as done before. A conversion from continuous to discrete, or *viceversa* is therefore necessary to effectively compare state-space models with the three other model families, *ARX*, *ARMAX* and *OE*. Block scheme of the state-space identified system is given in Figure 4.8, for the sake of completeness.

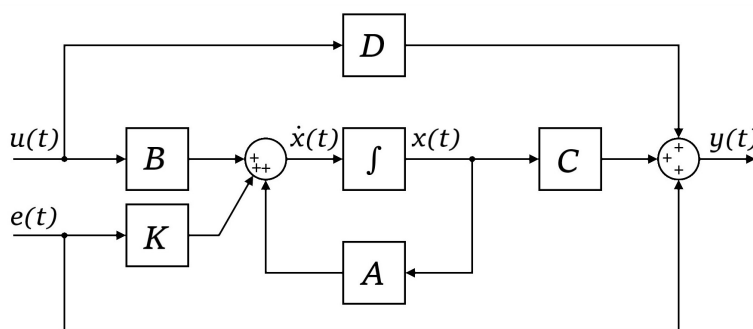


Figure 4.8: SS model block scheme. Adapted from [31]

4.5 Decoupled identification process and results

An analysis of the main results obtained from the identification process on engine parameters is here proposed. The data collected in Section 4.3 has its first four seconds removed, so as to ensure the starting engine condition does not erroneously affect the identification procedure; then it is divided into two equally long subsets, one used for the identification and a second one for the validation process. The data series are then deducted from their average, in order to better investigate the variation brought by the input signal.

At this stage, several identification algorithms are run, so as to compare, contrast and assess the best system models. The chosen identification schemes are the following ones, also outlined before:

- ARX models, entailing an autoregressive and an exogenous part.
- ARMAX models, moving average, *e.g.* *coloured noise* is added to ARX model.
- OE models, output error endowed with *white noise* modelling.
- State-space (or *SS*) models.

For what concerns the last model, state-space is used when dealing with a SISO system: its usage for MISO, SIMO or MIMO models implies the construction of matrices that eventually lead to transfer functions that share the same denominator. This leads to a loss of generality in the model, whose training procedure proves however to be more robust with reduced number of parameters, as there are more degrees of freedom to be tuned.

State-space models are eventually converted into transfer functions, for an easier understanding and handling, as well as for a direct comparison with other model families. This, however, implies the narrowing of the generality of the identified models, as the transfer function is created basing on the hypothesis of zero initial conditions. In turn, the non-null solution of the underlying differential equation is discarded.

Order n of the models is in every case swept between 1 and 3, as in most mechanical systems involving fluid-components coupling no higher orders are needed to accurately describe the system dynamics, this coming from previous engine airpath tests and past experience [1][2]. Moreover, higher order models may end up in *overfitting* problems, affecting the overall quality of the model on new datasets. The same reasoning is followed when imposing a maximum time delay between input and output, n_k .

From now on, a detailed report of the identification process on the points shown in Figure 4.9 is provided. Such points are chosen so as to be a comprehensive representation of the main engine behaviours and are

- Case 2, 1200 *rpm*, 14.7 *bar*, characterised by low engine speed and high *BMEP*;
- Case 10, 2250 *rpm* and 11.3 *bar*, characterised by medium engine speed and medium *BMEP* (map central point);
- Case 13, 3000 *rpm* and 6.5 *bar*, characterised by high engine speed and low *BMEP*;
- Case 16, 1000*rpm*, 3.9 *bar*, characterised by low engine speed and low *BMEP*.

The error parameters used to assess the quality of the estimates are here listed.

- *RMSE*, the root mean square error, between true and model-produced series.
- *AIC*, *Akaike's identification criterion*, minimizing the distance between model-produced probability density function and the true one.
- *MDL*, *Rissanen's minimum description length criterion*, similar to *AIC*; but penalising higher complexity models.
- *BF*, fit percentage between true output data series and the one simulated from the validation series.

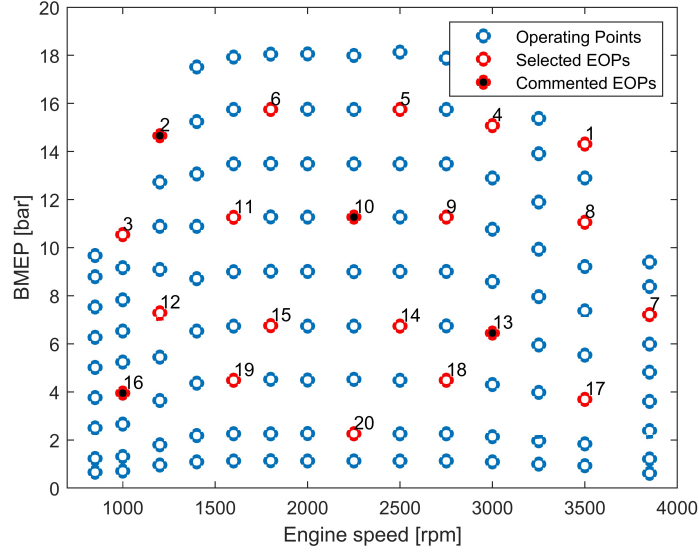


Figure 4.9: Engine map highlighting the EOPs over which a detailed identification procedure is provided for the four highlighted points

$RMSE$ is defined as in Equation 4.6.

$$RMSE = \sqrt{\frac{1}{N} \sum_{i=1}^N (y_i - \hat{y}_i)^2} \quad (4.6)$$

Here, y_i is the validation dataset output at time i and \hat{y}_i is the corresponding identified model output. N is the number of considered samples to compute the indicator. Low $RMSE$ values are better: a low value means there is not a major difference between reality and identified model. MSE value is obtained squaring the $RMSE$ and is shown for the sake of completeness. AIC error indicator, minimizing the so-called *Kullback* distance between the true probability density function of the data and the one produced by a given model, is better when negative; same is valid for MDL . AIC is defined as in Equation 4.7.

$$AIC = n \frac{2}{N} + \ln(RMSE) \quad (4.7)$$

In Equation 4.7 the first term accounts for the model complexity, being multiplied by the model order n and is furthermore divided by the number of input/output samples, N . The second term is a logarithmic adaptation of the $RMSE$. It is at this point immediate to notice that AIC can also take positive values, depending on the contributions of its two terms.

Same considerations are valid for MDL criterion, whose underlying equation is still characterised by a penalty term, due to model complexity, and an $RMSE$ -derived term, its equation being shown in 4.8.

$$MDL = n \frac{\ln N}{N} + \ln(RMSE) \quad (4.8)$$

Again, in Equation 4.8, $\ln(RMSE)$ can be below zero and, in the case it is bigger in absolute value than $\ln(RMSE)$, the quality indicator may also be negative. Eventually, BF performance indicator is better when closer to 100%.

4.5.1 EGR identification

This subsection illustrates and comments identification attempts run on the four selected cases, when EGR valve is controlled and VGT one is kept stationary.

| n_k | n | $RMSE \left[\frac{g}{s} \right]$ | $MSE \left[\frac{g^2}{s^2} \right]$ | $AIC [-]$ | $MDL [-]$ | $BF [%]$ |
|-------|-----|-----------------------------------|--------------------------------------|-----------|-----------|----------|
| 1 | 1 | 0.57 | 0.324471 | -1.12 | -1.12 | 85.8 |
| 1 | 2 | 0.49 | 0.239129 | -1.43 | -1.42 | 88.1 |
| 1 | 3 | 0.44 | 0.195514 | -1.63 | -1.62 | 89.7 |
| 2 | 1 | 0.98 | 0.952647 | -0.05 | -0.04 | 76.5409 |
| 2 | 2 | 0.89 | 0.795005 | -0.23 | -0.22 | 78.8 |
| 2 | 3 | 0.83 | 0.696563 | -0.36 | -0.35 | 80.3 |
| 3 | 1 | 0.96 | 0.916127 | -0.09 | -0.08 | 76.6 |
| 3 | 2 | 0.89 | 0.798828 | -0.22 | -0.22 | 78.2 |
| 3 | 3 | 0.82 | 0.67553 | -0.39 | -0.38 | 79.9 |

Table 4.3: ARX identification on case n. 2 - Validation metrics report

A first ARX identification is run on case n. 2, thus when engine speed is 1200 rpm and $BMEP$ is equal to 14.7 bar; to this regard, a validation error ARX summary is reported in Table 4.3. The identified models present a fairly good fit, especially when not considering huge delays between input and output signal ($n_k = 1$); in this situation, the model complexity in terms of order, n_a, n_b , affects the validation errors only marginally. A similar trend is followed by other indicators, such as $RMSE$: here it is evident that the distance between identified and true output grows with the increase of delay parameter n_k . It is furthermore noteworthy that, when going from second to third order models, the degree increase does not yield a significant improvement in either the MDL or the BF criterion, suggesting that a balance has to be found in choosing a model that is, contemporarily, descriptive but not cumbersome.

This latter piece of information allows to conclude that, when studying the relatively simple ARX model, a model with $n_k = 1$ and $n_a = n_b = 2$ is already adequate to describe the system behaviour.

Coefficients of the ARX model are now given in Equation 4.9, for the sake of completeness. In Equation 4.9, discrete-time ARX model, with $n_a = n_b = 1$; $n_k = 1$ and sample time 0.05 s, is given.

$$\begin{aligned} A(z)y(t) &= B(z)u(t) + e(t) \\ A(z) &= 1 - 0.395z^{-1} \\ B(z) &= -0.129z^{-1} \end{aligned} \tag{4.9}$$

Discrete-time ARX model, $n_a = n_b = 2$; $n_k = 1$ and sample time 0.05 s is given in Equation 4.10

$$\begin{aligned} A(z)y(t) &= B(z)u(t) + e(t) \\ A(z) &= 1 - 0.803z^{-1} + 0.314z^{-2} \\ B(z) &= -0.128z^{-1} - 0.002z^{-2} \end{aligned} \tag{4.10}$$

Same data series is now identified through several ARMAX models and performance results are given in Table 4.4.

| n_k | n | $RMSE \left[\frac{g}{s} \right]$ | $MSE \left[\frac{g^2}{s^2} \right]$ | $AIC [-]$ | $MDL [-]$ | $BF [\%]$ |
|-------|-----|-----------------------------------|--------------------------------------|-----------|-----------|-----------|
| 1 | 1 | 0.56 | 0.312547 | -1.16143 | -1.16 | 86.9 |
| 1 | 2 | 0.45 | 0.203539 | -1.58875 | -1.58 | 88.7 |
| 1 | 3 | 0.40 | 0.159662 | -1.82997 | -1.82 | 90.5 |
| 2 | 1 | 0.87 | 0.763369 | -0.27 | -0.26 | 79.1 |
| 2 | 2 | 0.84 | 0.698739 | -0.36 | -0.35 | 79.9 |
| 2 | 3 | 0.81 | 0.663327 | -0.41 | -0.39 | 80.6 |
| 3 | 1 | 0.89 | 0.797777 | -0.22 | -0.22 | 78.6 |
| 3 | 2 | 0.87 | 0.765247 | -0.26 | -0.25 | 78.9 |
| 3 | 3 | 0.81 | 0.659709 | -0.41 | -0.40 | 80.2 |

Table 4.4: ARMAX identification on case n. 2 - Validation metrics report

Here, a marginally better fit compared to the simpler ARX model is achieved, at the cost of a worse MDL, this is shown taking the example of $n_k = 1$, $n = 2$, featuring a $BF_{ARX} = 88.1\%$ vs $BF_{ARMAX} = 88.7\%$ and $MDL_{ARX} = -1.42$ vs $MDL_{ARMAX} = -1.58$. In this case, given the higher complexity of ARMAX models, a possible design choice is to discard it, keeping a simpler and equally accurate ARX description. An ARMAX model with coefficients is in any case given, with a view to comparing it to the previously studied ARX model.

Discrete-domain ARMAX model, $n_a = n_b = n_c = 2$; $n_k = 1$ and sample time 0.05 s is shown in Equation 4.11.

$$\begin{aligned}
 A(z)y(t) &= B(z)u(t) + C(z)e(t) \\
 A(z) &= 1 - 0.348z^{-1} + 0.192z^{-2} \\
 B(z) &= -0.121z^{-1} - 0.055z^{-2} \\
 C(z) &= 1 + 0.511z^{-1} + 0.264z^{-2}
 \end{aligned} \tag{4.11}$$

It is noticeable that coefficients have only slightly varied compare to the ARX case: summing up, the ARMAX model does not provide major differences compared to the corresponding ARX one, if not for the addition of the coloured noise structure.

| n_k | n | $RMSE \left[\frac{g}{s} \right]$ | $MSE \left[\frac{g^2}{s^2} \right]$ | $AIC [-]$ | $MDL [-]$ | $BF [\%]$ |
|-------|-----|-----------------------------------|--------------------------------------|-----------|-----------|-----------|
| 1 | 1 | 0.65 | 0.417272 | -0.87 | -0.87 | 82.6 |
| 1 | 2 | 0.55 | 0.302507 | -1.19 | -1.19 | 84.4 |
| 1 | 3 | 0.53 | 0.285371 | -1.25 | -1.24 | 84.9 |
| 2 | 1 | 1.05 | 1.09882 | 0.10 | 0.10 | 74.3 |
| 2 | 2 | 1.03 | 1.06746 | 0.07 | 0.07 | 74.7 |
| 2 | 3 | 1.01 | 1.01337 | 0.02 | 0.03 | 75.3 |
| 3 | 1 | 1.69 | 2.84995 | 1.05 | 1.05 | 59.6 |
| 3 | 2 | 1.63 | 2.64108 | 0.97 | 0.98 | 60.5 |
| 3 | 3 | 2.31 | 5.3573 | 1.68 | 1.69 | 30.8 |

Table 4.5: OE identification on case n. 2 - Validation metrics report

OE case, presented in Table 4.5, shows a difference compared to the two previous models: due to the relatively simple error structure, the model performance is worse and error metrics are substantially lower for every indicator, except for the MDL , benefitting from the lower model complexity; once more, first or second order models are fully adequate to represent system dynamics, and there is no substantial improvement when using third order models. A further demonstration of this can also be seen from Figure 4.10, where only minor overshoots or undershoots can be seen in the \dot{m}_{air} behaviour when EGR steps occur: overshoots, indeed, require an at least second order models structure to be represented.

A complete OE identification output, with model coefficients is now given in Equation 4.12, where the discrete-domain OE model with $n_b = n_f = 2$, $n_k = 1$ and sample time 0.05 s is shown.

$$\begin{aligned}
 y(t) &= [B(z)/F(z)]u(t) + e(t) \\
 B(z) &= -0.141z^{-1} - 0.042z^{-2} \\
 F(z) &= 1 - 0.371z^{-1} + 0.244z^{-2}
 \end{aligned} \tag{4.12}$$

A parallel comparison with the previous models is here no longer possible; it comes as no surprise that model performance deteriorates once the model complexity increases, as the model structure is essentially not tailored to represent the system dynamics.

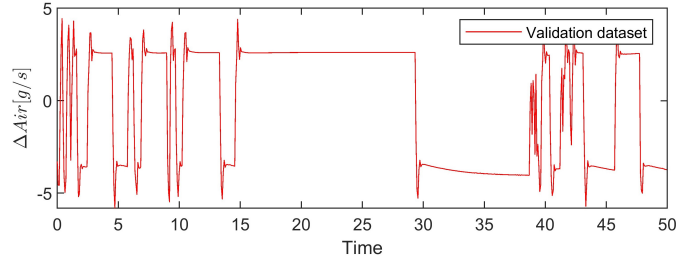


Figure 4.10: EGR control action and \dot{m}_{air} response in case n. 2

A last identification is now performed directly relying on state space models and outcome is shown in Table 4.6. Here, no sweep on delay parameter n_k is performed. This latter identification features errors that are comparable to ARX and ARMAX models. Besides, model quality is not appreciably improved if model order is increased. It is, ultimately, interesting to note that, however going hand in hand with AIC , the MDL error parameter gradually detaches from AIC error, becoming worse owing to the higher model order.

| n | $RMSE \left[\frac{g}{s} \right]$ | $MSE \left[\frac{g^2}{s^2} \right]$ | $AIC [-]$ | $MDL [-]$ | $BF [\%]$ |
|-----|-----------------------------------|--------------------------------------|-----------|-----------|-----------|
| 1 | 0.56 | 0.312017 | -1.16 | -1.16 | 86.9 |
| 2 | 0.45 | 0.202348 | -1.60 | -1.59 | 88.7 |
| 3 | 0.40 | 0.159517 | -1.83 | -1.82 | 90.5 |

Table 4.6: SS identification on case n. 2 - Validation metrics report

Again, the model coefficients are fully represented, showing a discrete-time state-space model, with $n = 1$; $n_k = 1$ and sample time 0.05 s in Equation 5.1.

$$\begin{aligned}
 x(t+k) &= Ax(t) + Bu(t) + Ke(t) \\
 y(t) &= Cx(t) + Du(t) + e(t) \\
 A &= 0.347; B = -0.121; C = 1; D = 0; K = 0.350
 \end{aligned} \tag{4.13}$$

An example of the identification process output, on a validation test signal, is now reported in Figure 4.11, whose graphs show a substantial superimposition between the validation dataset curve and the effective ARX $n_k = 1$, $n_a = n_b = 2$ model output; the model output, however not significantly delayed with respect to the validation data, shows a small tail effect that is owed to the peculiar distribution of zeros and poles in z -plane.

A further point that has to be mentioned is the non-perfect achievement of the validation dataset steady state value. Being the model output steady state slightly bigger

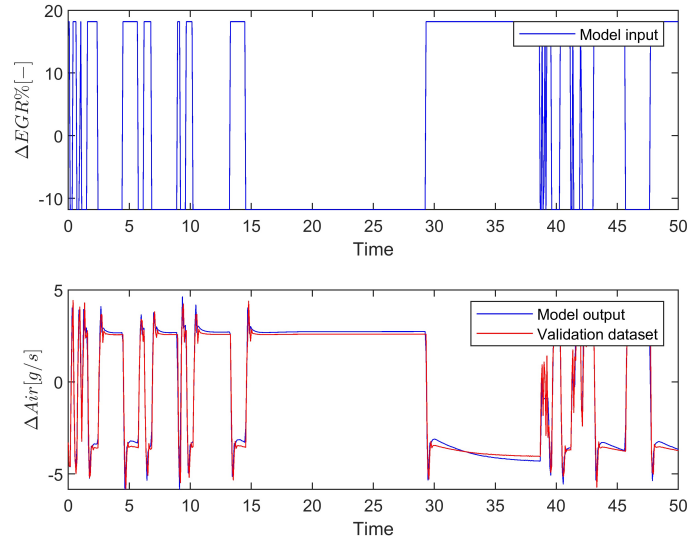


Figure 4.11: ARX model with $n_k = 1$, $n_a = n_b = 2$, EGR control action variation and \dot{m}_{air} variation in case n. 2 - comparison with validation dataset

than the validation dataset for both positive and negative curve steady state values, it is reasonable to conclude that a small mismatch between model gain and real one is present.

Table 4.7 give an overview of the most representative identification models altogether, in order to clearly grasp differences and similarities between them. Specifically, ARX, ARMAX, OE models of orders $n = 1, 2$ and $n_k = 1$ are shown, along with the ARMAX $n = 2$, $n_k = 2$ and with SS models of order $n = 1, 2$. These models are selected as representing a compromise between identification quality and complexity: indeed, second order models are neither control-wise cumbersome, nor too simple to capture the plant dynamics. In parallel to them, examples of ARX and OE models are given, to underline their lower quality with respect to ARMAX and SS ones.

Overall results on EGR case n. 2, presented in Table 4.7, show once more that the best performing models are the simplest ones, both with low complexity order and the smallest time delay. Another point that needs to be mentioned is the similarity between ARX and OE model structure outputs, when the model order is low: once the order increases, OE models performance decays as they are not capable of taking into account the error dynamics, being the transfer function that models the error simpler than the one adopted in ARX and ARMAX models. SS model achieve very satisfying performance and are close to ARMAX in terms of model coefficients and validation metrics. They are therefore eventually chosen as a basis to the development of the airpath control logics.

Summary tables for case n. 10 is provided, in 4.8.

Case n. 10 shows a similar behaviour to case n. 2 and highlights the trend of the performance indicators: up to order $n = 2$ there is a noticeable however not huge improvement in BF percentage. At the same time, a performance worsening when increasing time delay n_k

| Model | n_k | n | $RMSE \left[\frac{g}{s} \right]$ | $MSE \left[\frac{g^2}{s^2} \right]$ | $AIC [-]$ | $MDL [-]$ | $BF [%]$ |
|-------|-------|-----|-----------------------------------|--------------------------------------|-----------|-----------|----------|
| ARX | 1 | 1 | 0.57 | 0.324471 | -1.12 | -1.12 | 85.8 |
| ARX | 1 | 2 | 0.49 | 0.239129 | -1.43 | -1.42 | 88.1 |
| ARMAX | 1 | 1 | 0.56 | 0.312547 | -1.16 | -1.16 | 86.9 |
| ARMAX | 1 | 2 | 0.45 | 0.203539 | -1.59 | -1.58 | 88.7 |
| ARMAX | 2 | 2 | 0.84 | 0.698739 | -0.36 | -0.35 | 79.9 |
| OE | 1 | 1 | 0.65 | 0.417272 | -0.87 | -0.87 | 82.6 |
| OE | 1 | 2 | 0.55 | 0.302507 | -1.19 | -1.19 | 84.4 |
| SS | 1 | 1 | 0.56 | 0.312017 | -1.16 | -1.16 | 86.88 |
| SS | 1 | 2 | 0.45 | 0.202348 | -1.60 | -1.59 | 88.7 |

Table 4.7: Selected models identification on EGR case n. 2 - Validation metrics

| Model | n_k | n | $RMSE \left[\frac{g}{s} \right]$ | $MSE \left[\frac{g^2}{s^2} \right]$ | $AIC [-]$ | $MDL [-]$ | $BF [%]$ |
|-------|-------|-----|-----------------------------------|--------------------------------------|-----------|-----------|----------|
| ARX | 1 | 1 | 0.50 | 0.248605 | -1.39 | -1.39 | 88.7 |
| ARX | 1 | 2 | 0.47 | 0.224071 | -1.49 | -1.49 | 89.7 |
| ARMAX | 1 | 1 | 0.50 | 0.246373 | -1.40 | -1.39 | 89.1 |
| ARMAX | 1 | 2 | 0.43 | 0.186522 | -1.68 | -1.66 | 90.3 |
| ARMAX | 2 | 1 | 0.92 | 0.841572 | -0.17 | -0.16 | 79.4 |
| OE | 1 | 1 | 0.54 | 0.288879 | -1.24 | -1.24 | 87.2 |
| OE | 1 | 2 | 0.44 | 0.19404 | -1.64 | -1.63 | 89.8 |
| SS | 1 | 1 | 0.50 | 0.246351 | -1.40 | -1.40 | 89.1 |
| SS | 1 | 2 | 0.43 | 0.186738 | -1.68 | -1.67 | 90.3 |

Table 4.8: Selected models identification on EGR case n. 10 - Validation metrics

from 1 to 2 occurs: this can be noticed from Table 4.8, considering each of the indicators, from $RMSE$, that is almost doubled, to AIC and MDL , that go almost hand in hand, up to BF criterion, dropping by more than 10 percentage points. Tables of cases n. 13 and n. 16 are omitted, being the identification results largely parallel to those already highlighted.

4.5.2 VGT identification

This subsection illustrates and comments identification attempts run on the four target cases, this time when VGT valve is controlled and EGR one is kept stationary.

Here, a dissertation on case n. 2 is given: first macroscopic point to be brought up is the higher fitting percentage, compared to the previously identified EGR models. This is justified by the higher transient times, shown in Figure 4.12 that are typical of the VGT valve: an almost complete superimposition between validation dataset and model output is visible. The absence of long steady-state ranges implies that the model puts more effort in identifying transient behaviours, correctly sticking to them, however not many pieces of information are provided with respect to the steady state gain of the system, or to possible unseen tail effects. To this regard, it is conceivable that same EGR small discrepancies

will occur in the VGT identification process, provided to use a longer VGT step periods identification signal. From a macroscopic perspective, as in the EGR identification process, error descriptors tend to decrease, however not by much, when increasing model time delay and they marginally increase when increasing model order n ; this can be seen from Tables 4.9 and 4.10. ARX and ARMAX model performances are comparable and, the other way round, OE performance slightly lowers when increasing output time step delay. SS performance is, as expected, very similar to ARMAX one.

| Model | n_k | n | $RMSE \left[\frac{g}{s} \right]$ | $MSE \left[\frac{g^2}{s^2} \right]$ | $AIC [-]$ | $MDL [-]$ | $BF [%]$ |
|-------|-------|-----|-----------------------------------|--------------------------------------|-----------|-----------|----------|
| ARX | 1 | 1 | 0.00172172 | 2.96433e-06 | -12.7277 | -12.7242 | 98.4209 |
| ARX | 1 | 2 | 0.000462691 | 2.14083e-07 | -15.3546 | -15.3476 | 99.5477 |
| ARMAX | 1 | 1 | 0.00160787 | 2.58525e-06 | -12.864 | -12.8587 | 98.5392 |
| ARMAX | 1 | 2 | 0.000453526 | 2.05686e-07 | -15.3935 | -15.3829 | 99.5619 |
| ARMAX | 2 | 1 | 0.000974481 | 9.49614e-07 | -13.8655 | -13.8602 | 99.1026 |
| OE | 1 | 1 | 0.00552535 | 3.05295e-05 | -10.3957 | -10.3922 | 94.3758 |
| OE | 1 | 2 | 0.00444129 | 1.9725e-05 | -10.8313 | -10.8243 | 95.2035 |
| SS | 1 | 1 | 0.00152187 | 2.3161e-06 | -12.9745 | -12.971 | 98.593 |
| SS | 1 | 2 | 0.000453475 | 2.0564e-07 | -15.3949 | -15.3878 | 99.5618 |

Table 4.9: Selected models identification on VGT case n. 2 - Validation metrics report

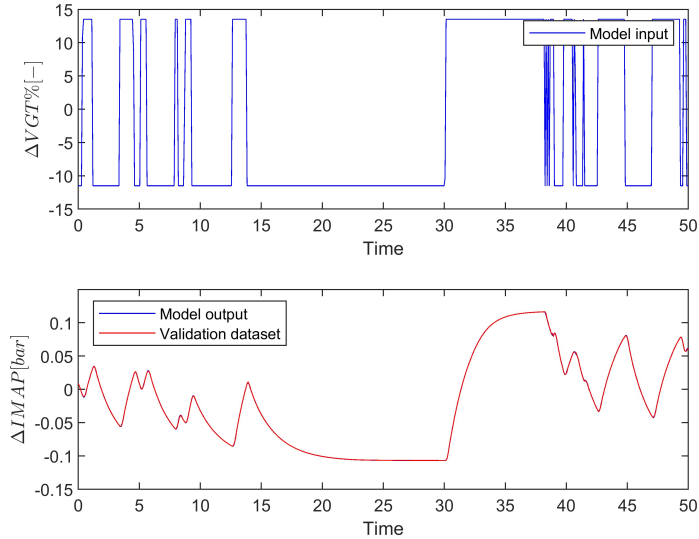


Figure 4.12: SS model with $n_k = 1$, $n = 2$, VGT control action and $IMAP$ response in case n. 2 - comparison with validation dataset

Concerning the other three examined cases, again no major behaviour differences can be seen. RMSE and MSE values are predictably smaller than in the EGR case, due to the implicitly smaller IMAP values. AIC and MDL error metrics are accordingly smaller.

| Model | n_k | n | $RMSE \left[\frac{g}{s} \right]$ | $MSE \left[\frac{g^2}{s^2} \right]$ | $AIC [-]$ | $MDL [-]$ | $BF [%]$ |
|-------|-------|-----|-----------------------------------|--------------------------------------|-----------|-----------|----------|
| ARX | 1 | 1 | 0.00157478 | 2.47992e-06 | -12.9062 | -12.9028 | 98.5876 |
| ARX | 1 | 2 | 0.00147002 | 2.16097e-06 | -13.0428 | -13.036 | 98.8281 |
| ARMAX | 1 | 1 | 0.00153708 | 2.3626e-06 | -12.9541 | -12.949 | 98.7056 |
| ARMAX | 1 | 2 | 0.00139101 | 1.9349e-06 | -13.1522 | -13.142 | 98.8787 |
| ARMAX | 2 | 1 | 0.00452698 | 2.04935e-05 | -10.7938 | -10.7887 | 96.1871 |
| OE | 1 | 1 | 0.0088228 | 7.78418e-05 | -9.45974 | -9.45633 | 90.2245 |
| OE | 1 | 2 | 0.00873315 | 7.6268e-05 | -9.47906 | -9.47226 | 89.6584 |
| SS | 1 | 1 | 0.00148619 | 2.20876e-06 | -13.022 | -13.0186 | 98.7452 |
| SS | 1 | 2 | 0.00139092 | 1.93467e-06 | -13.1534 | -13.1466 | 98.8787 |

Table 4.10: Selected models identification on VGT case n. 10 - Validation metrics report

4.6 Identification summary and prospects

Given the overview of the run identification process, state-space and ARMAX models are preferred over ARX and OE ones, the reason for the former preference being the higher fit percentages and completeness that they guarantee. Lack of an adequate error representation in other models is witnessed by the otherwise low performance indicators, being evident especially in OE models.

SS models have an edge over the other model families, since their different structure provides additional pieces of information, highlighting the intermediate states that describe the system. This is not the case in ARX, ARMAX and OE counterparts. SS models are consequently chosen so as to implement the system control architecture. For what concerns the model order, setting $n = 2$ is deemed as the best choice to capture system behaviour. In case of a fluid-mechanical components coupling, second order generally is a proper description, as already illustrated in Section 4.5. Conversely, order $n = 1$ models would not be able to correctly represent overshoots or undershoots; models with order $n = 3$ or higher would yield unnecessary complications in successive control design and implementation, possibly adding high frequency zeros and poles that do not give an actual contribution to the effective system dynamics. Eventually, time delay n_k is set to 1, as its performance in terms of any error metric is definitely better than for higher delays. In the state-space models family, time delay choice is, in any case, not possible, and $n_k = 1$ by default. A broader perspective on the models chosen for control purposes is given in Chapter 5, where an algorithm to effectively select a subset of the total EOPs is presented in Section 5.1, basing on identified models performances. In addition to that, model characteristics are deepened and zeros-poles maps, Bode and Nichols charts are presented in the same Section.

A final comment that needs to be stressed is the altogether good fitting of the models with the *simulated* behaviour of the system, meaning that the model families that are proposed are able to efficiently tackle the identification problem. It is anyway crucial to bear in mind that the *real* airpath system is largely more affected by noise, non-linearities, and disturbances in general. Hence, identified models would yield lower fitting percentages,

when basing on a true test-bank dataset. The comparison between the two results serves as the foundation for future works/studies that delve deeper into the subject.

Chapter 5

Control

In this chapter, different control strategies are investigated. Aim of this part of the work is to provide the EGR and VGT engine valves with a reliable control law, that is able to guarantee the fulfillment of the engine performance, in terms of target air mass flow rate and IMAP tracking.

5.1 Control EOPs selection

In order to tackle any control problem, first the model on which to operate has to be clearly identified. To this regard, the work done in Chapters 3 and 4 is brought up and the twenty EOPs that have been selected and modelled are further skimmed. This lays the foundations for a faster operating point labelling to each current engine state, having to spot the best suited model among a smaller subset of points, thus speeding up the control logic. In addition to that, the process leads to the simplification of the overall airpath plant, resulting in simpler and less cumbersome control design techniques.

The EOP skimming process pursues the dimensional reduction of the previously selected twenty EOPs. A reasonable amount of control EOPs, that still does not compromise the engine airpath modelling quality is ca. the half of the initial points. However this being in general not always valid, past experience as well as control results illustrated in Chapter 7 do indeed demonstrate that the choice is largely acceptable.

To achieve such screening, EOP identified models are mutually compared, to understand when they can be replaced one by the other. When it is the case, a *benchmark* point, and therefore its surrounding engine map region, can be replaced by the mathematical model of a *comparison* point, of a nearby map region. Graphical and procedural description of this idea is given in Chapter 3.

Models that are used to reciprocally compare their performances, when replaced with other ones, are those obtained from ARMAX and the SS identifications, following the results of Section 4.5. This choice is consequential to the higher completeness that these models bring, when used to describe the air-path system. For the same reason, second order models are adopted, instead of first order ones.

At this point, the list of performance indicators defining the interchangeability between two models is given.

- Mutual percent fit of *compared* model, applied to *benchmark* validation points, or BF;
- Percent fit variation, from *benchmark* validation fit to *compared* model applied to validation, also called ΔBF ;
- Zero-pole-gain relative difference between *benchmark* model and *comparison* one, here referred to as ΔZPK .

The first quantity is obtained performing a model validation on the dataset with the *comparison* model and taking the fit value. Second indicator is a derivation of the former, that takes the difference between fit percentage of the *benchmark* model minus the one of the *comparison* model; the lower the index, the better a model can replace the other, without losing descriptive accuracy.

The third performance indicator is more cumbersome and is therefore described in Equation 5.1, with an example.

Zero-pole-gain relative difference is computed as the average between relative errors between zeroes, poles and gains of the *benchmark* and the *compared* model. Relative errors are expressed with respect to the *benchmark* model. A comparison example between two models both having $m = 1$ zero and $n = 2$ poles is here given in Equation 5.1, where their parameters are outlined.

$$\begin{aligned} k_b &= 1; \quad z_b = 0.5; \quad p_{b,1} = 0.3; \quad p_{b,2} = 0.7 \\ k_c &= 1.2; \quad z_c = 0.4; \quad p_{c,1} = 0.3; \quad p_{c,2} = 0.6 \end{aligned} \quad (5.1)$$

In the equation, b stands for *benchmark* and c stands for *comparison*. Equation to compute ΔZPK is

$$\begin{aligned} \Delta ZPK &= \text{avg} \left(\left| \frac{k_c - k_b}{k_b} \right| + \sum_{i=1}^m \left| \frac{z_{ci} - z_{bi}}{z_{bi}} \right| + \sum_{j=1}^n \left| \frac{p_{cj} - p_{bj}}{p_{bj}} \right| \right) = \\ &= \text{avg} \left(\left| \frac{1.2 - 1}{1} \right| + \left| \frac{0.4 - 0.5}{0.5} \right| + \left| \frac{0.3 - 0.3}{0.3} \right| + \left| \frac{0.6 - 0.7}{0.6} \right| \right) = \\ &= \text{avg} (0.2 + 0.2 + 0 + 0.17) = 0.142 \end{aligned} \quad (5.2)$$

From 5.1 it is already possible to see that the lower ΔZPK is, the closer zeroes, poles and gains of the two models are. Differences are taken in absolute value so as to account for both higher and lower *comparison* model zeros/poles/gains. This data, however, does not account for possible sign changes occurring to zeros and poles: this specific situation

has to be studied case by case, in order not to lose track of consequential possible model misbehaviours. The afore-mentioned performance indicators refer to averaged values between ARX and SS models and give therefore an overall idea of how close the two points are from not just a *control*, but also a *physical* point of view.

Once the three indicators are designed, each of the twenty EOPs is compared to the remaining nineteen, by evaluating such indicators; the comparison is performed once for $EGR-\dot{m}_{air}$ systems and once for $VGT-IMAP$ ones. Results are stored and graphically represented in Figure 5.1.

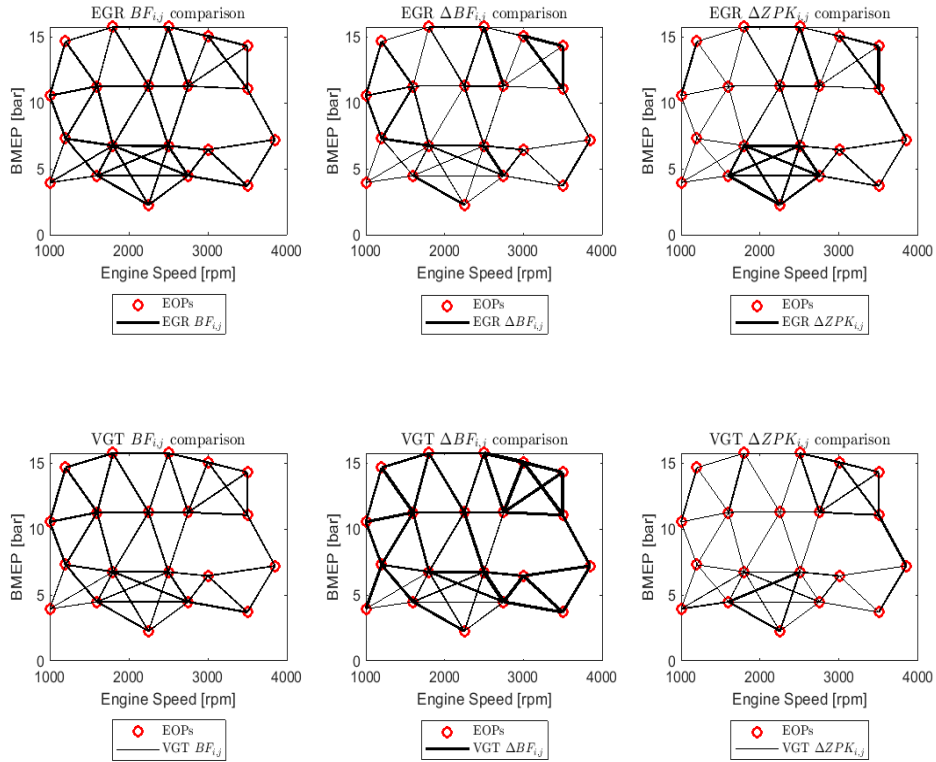


Figure 5.1: EOPs mutual relationships, for both EGR (top) and VGT (bottom) models, exponential linewidth. Thicker lines representing high affinity between two points

Network in Figure 5.1 represents, once for each criterion, the affinity between two EOP models: the thicker the line, the more similar the two EOP models; only lines between relatively close models have been drawn. The lines thickness is scaled to emphasize the differences between model performances: indeed, affinity indicators, such as fitting percentage, do almost never go below 80%, however being represented by relatively narrow lines. Aim of the control engineer is to choose, among the twenty points, those satisfying one of the two following conditions:

- *Benchmark* does not share *any* thick line with the adjacent EOPs and thus could not be replaced by other models.
- *Benchmark* shares thick links with other *comparison* EOPs, implying that they may be able to replace them if the others are discarded.

The procedure is performed first of all evaluating the fit between two models (see *BF* graphs in 5.1); the second indicator used to discern between candidate control EOPs is the zero-pole-gain similarity, or ΔZPK in 5.1). A further criterion is the fit variation between *benchmark* model and *comparison* one. Iterating this affinity assessment procedure until a satisfactory result is reached, with all the discarded points being substituted by a fairly similar adjacent model, the selected control points are the ones shown in blue in Figure 5.2.

Figure 5.2 emphasizes how the selection criteria have been applied. Specifically drawing the attention to high speed - high *BMEP* region, as an example, it is possible to see how all the four EOPs inside the curve, in bottom-right VGT plot, do share thick links and are therefore model-wise similar one to each other. The same points show similar affinity also with respect to the other indicators, they are therefore replaced by only one of them, CEOP n. 8, the *central* one.

Once a similar choice has been made for the whole set of EOPs, a double-check on the exact position of zeroes and poles of the models is performed, so as to ensure these values keep the same sign when switching from a model to an affine other one.

As it possible to observe from Figure 5.2, engine map shows different properties across well recognisable areas: left map region, featuring low engine speed EOPs, entails significantly different models if compared to central-to-right area of the map, where models start being more similar one to the other: this is mostly due to possible non-linearities affecting the model at low speeds or low pressure areas. More marked differences can be seen between VGT high-low speed EOPs, when compared to the same points in EGR control actions. A last remark is given, concerning ZPK affinity: however more evident than model fitting performance, or BF, zeroes, poles and gains small variations seem not to play an upsetting role on the model quality, that remains fairly high, except for some specific points, such as EOP n.16, on bottom-left part of the engine map.

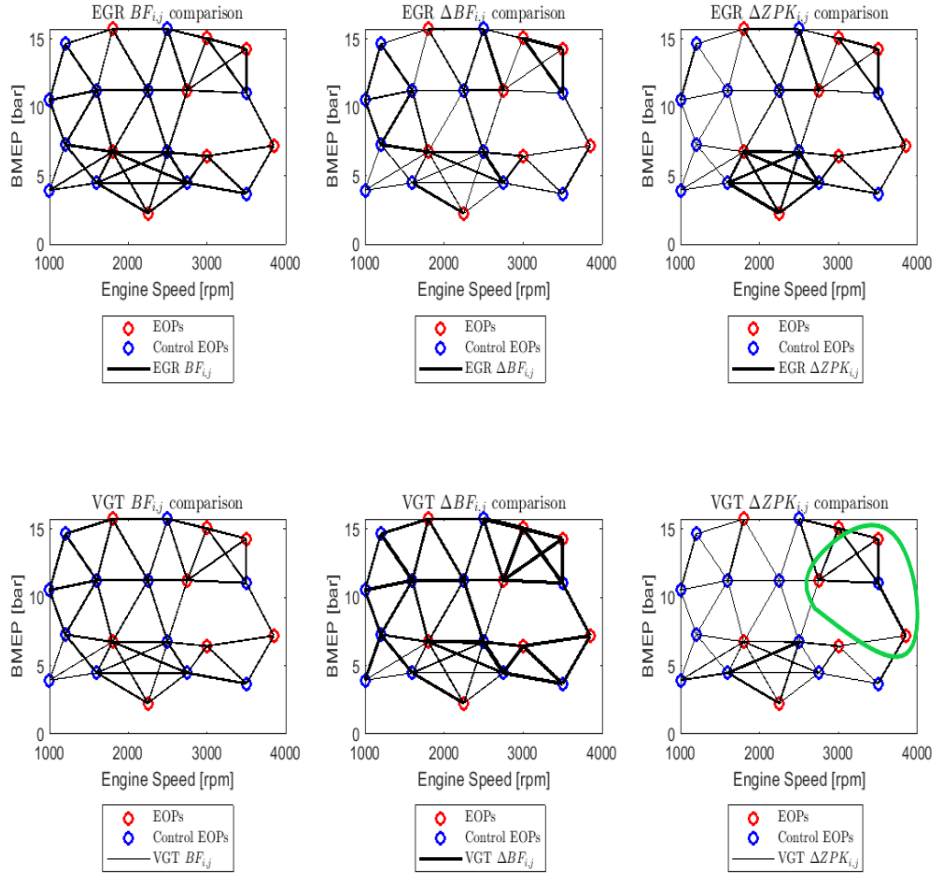


Figure 5.2: Chosen control EOPs and mutual relationships, for both EGR (top) and VGT (bottom) models. Thicker lines representing high affinity between two points. A four point cluster is highlighted in green

The eventual matching between discarded EOPs and remaining control points is proposed in Table 5.1, where if the point number does not change, it means the point is indeed one of the chosen control points.

Same results of Table 5.1 are graphically reported in Figure 5.3, where what immediately stands out is the vicinity between replaced EOPs and corresponding CEOPs, as for the case of top-right cluster, featuring medium-high engine speed as well as $BMEP$ in all its points. Another interesting detail is the model affinity between points in bottom-centre of the engine map, featuring medium engine speed and low $BMEP$; here, depending on the point, EOP is replaced by the CEOP with closest engine speed or $BMEP$, depending on the situation, meaning there is a slight edge in model affinity when either $BMEP$ or engine speed is close. More on this topic was given in Chapter 3.

| Original EOP | CEOP | Original EOP | CEOP |
|--------------|------|--------------|------|
| 1 | 8 | 11 | 11 |
| 2 | 2 | 12 | 12 |
| 3 | 3 | 13 | 14 |
| 4 | 5 | 14 | 14 |
| 5 | 5 | 15 | 18 |
| 6 | 10 | 16 | 16 |
| 7 | 8 | 17 | 17 |
| 8 | 8 | 18 | 18 |
| 9 | 8 | 19 | 19 |
| 10 | 10 | 20 | 14 |

Table 5.1: Initial EOPs and corresponding replacements. Control EOPs are in bold

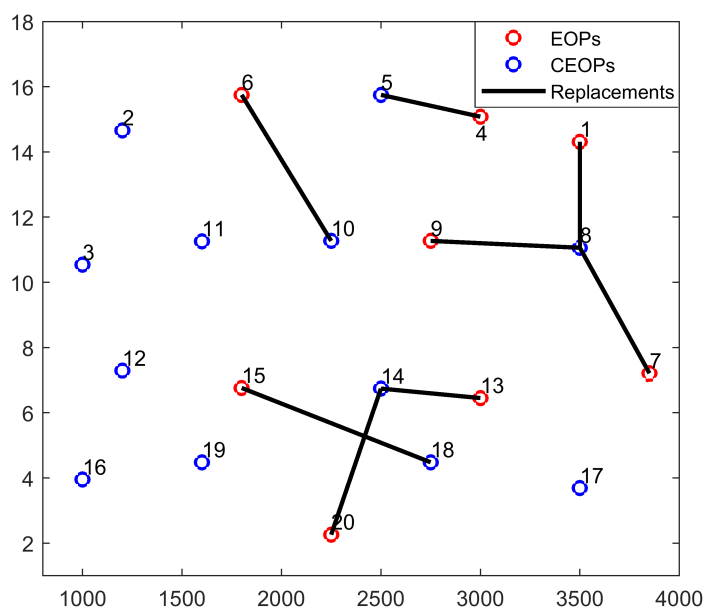


Figure 5.3: Chosen CEOPs, replacing original EOPs; replacement is shown by black lines

5.1.1 The ARMAX case

Figure 5.4 shows the zeros and poles placement of both the original model, in red, and the replacing one, in blue, in the ARMAX models of order $n = 2$, both for $A(z)$ and for $B(z)$ polynomial. If no red points are seen, this means the replacing model is so similar to the starting one that its zeros and poles are almost superimposed to those of the original model. Figure 5.4 shows zeros and poles of EGR -air mass flow rate system in the continuous domain rather than the discrete one, to facilitate interpretation and comparison with SS models of the same plants; plots represent the domain in a $[-60; 60]$ range.

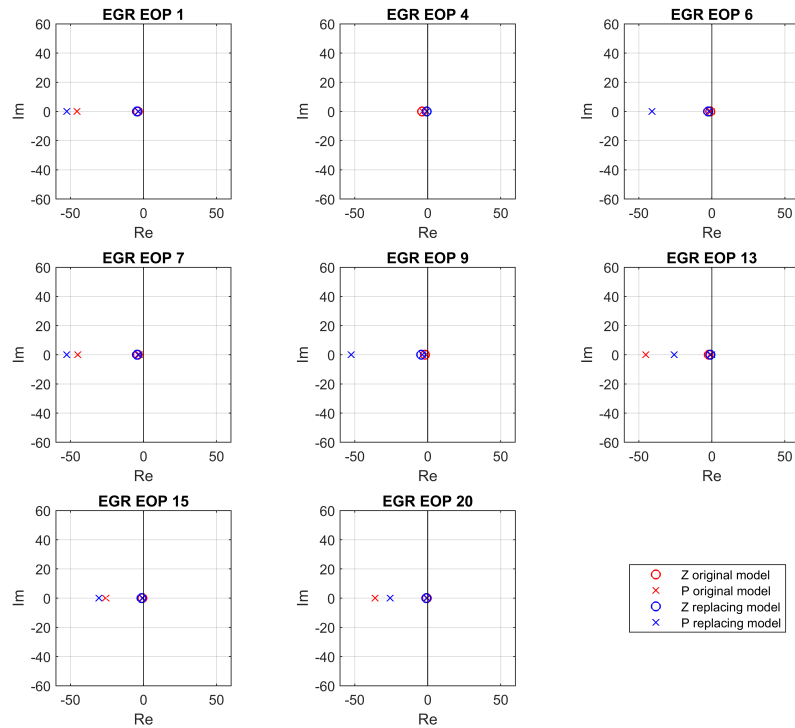


Figure 5.4: Continuous ARMAX zeros-poles map of the eight replaced original EOPs and their replacing CEOPs

5.1.2 The state-space case

This subsection illustrates the main features of EGR - air mass flow rate system, with a view to comparing the *benchmark* CEOPs, used for control purposes, with the *replaced* ones.

Graph in Figure 5.5 shows the zeros-poles placement in the continuous state-space order $n = 2$ models. This specific outcome demonstrates that the assigned parameters are not far from the ones assigned through ARMAX models.

For what concerns the gains, k , they play a noticeable role, as they are responsible for the steady state value of the air-path variables behaviour. What is more, gains signs affect the increase/decrease in the output variable, depending on the given input. An example of this can be found in EGR - \dot{m}_{air} SISO models of any kind: here, a wider opening of the EGR valve corresponds to less air entering the combustion chamber, thus \dot{m}_{air} decreases and transfer function gain is, as a consequence, negative. The outcome of the model replacements, in terms of gains variation is summarised in Table 5.2.

| Original EOP | Original $K_{P,VGT}$ | Replacing EOP | $K_{P,VGT}$ Replacing |
|--------------|----------------------|---------------|-----------------------|
| 1 | -41.2 | 8 | -45.3 |
| 4 | -238.1 | 5 | -32.5 |
| 6 | -255.8 | 10 | -12.0 |
| 7 | -29.5 | 8 | -45.3 |
| 9 | -34.2 | 8 | -45.3 |
| 13 | -14.4 | 14 | -5.4 |
| 15 | -4.3 | 18 | -6.8 |
| 20 | -2.5 | 14 | -5.4 |

Table 5.2: $K_{P,EGR}$ gains for original models and replacing CEOPs, for continuous domain SS model family

Table 5.2 shows a fair similarity between original and replacing gain of the plant transfer functions. Replacing gains do indeed almost never change in terms of order of magnitude, except for cases n. 6 and 4. Point n. 6 is replaced by CEOP n. 10, featuring a 4 *bar* difference, this being the major reason for the gain variation. EOP n. 4, lays on the full load engine curve, thus replacement is critical. The latter has been in any case deemed as feasible, due to the similarity between zeros and poles of the model, as well as the high correlation between corresponding VGT models of the same original and replacing EOP. Plant gains $K_{P,EGR}$ are, according to physical considerations, all negative.

Figure 5.5 shows there is a reasonable affinity between zeros and poles of original and replacing model; most of all, models featuring imaginary roots, such as n. 2 and 3, are not replaced by other models, as in this specific case, or by one sharing this same trait, so as not to neglect specific oscillating system dynamics. These two models are therefore not shown in the graph.

Concerning the very same state-space order $n = 2$ models, a Bode plot representing magnitude, in Figure 5.6 and phase rotation, in Figure 5.7, is now given. The similarities between the magnitude and the phase in the plots indicate there is a satisfactory correlation between zeros and poles of the original model and the replacing one. On the contrary, gain K yields a marginal difference to the plots amplitude, visible as an offset mismatch between red and blue curves in Figure 5.6.

The results of the replacement process in terms of EGR models show an almost global adequacy of the replacing models, except for few local cases, one of them being EOP n. 6, where the presence of a high frequency negative pole is possibly caused by the usage of a second order identification model, instead of a first order one. EOP n. 6 is eventually replaced by EOP n. 10, not presenting this feature; the substitution takes place with a CEOP that is ca. 4 *bar* below and 700 *rpm* above in the engine map, this being a further explanation for the difference between the two models. Models of VGT actuation are, conversely, much more similar for the two EOPs, being this noticeable from graph to the centre-bottom in Figure 5.2: indeed, almost all of the EOPs are connected through thick lines, indicating the loss in terms of BF between original and replacing model is negligible, when replacing an EOP model with another one.

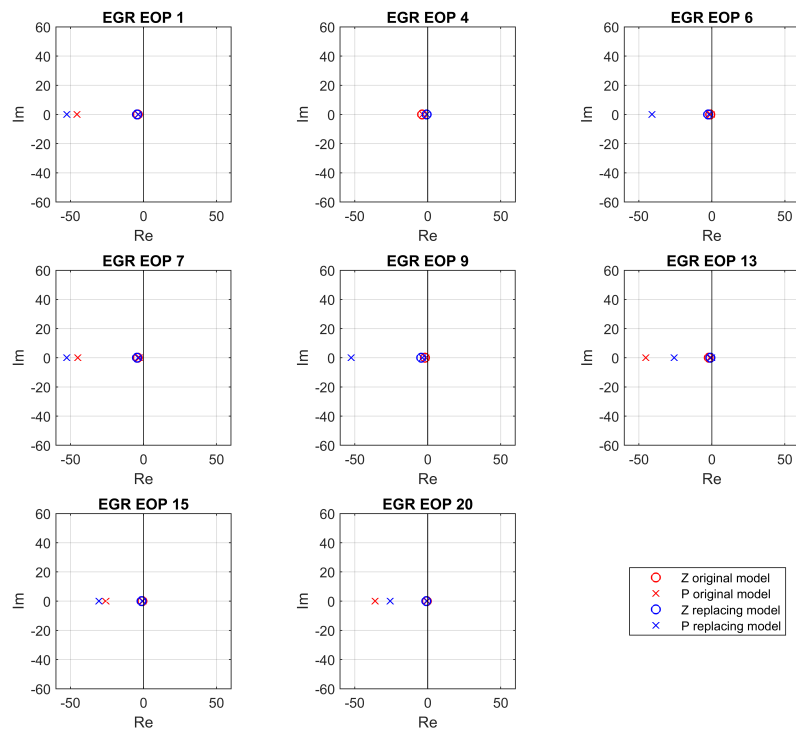


Figure 5.5: Continuous SS zeros-poles map of the eight replaced original EOPs and their replacing CEOPs, $[0; 50]$ axes range

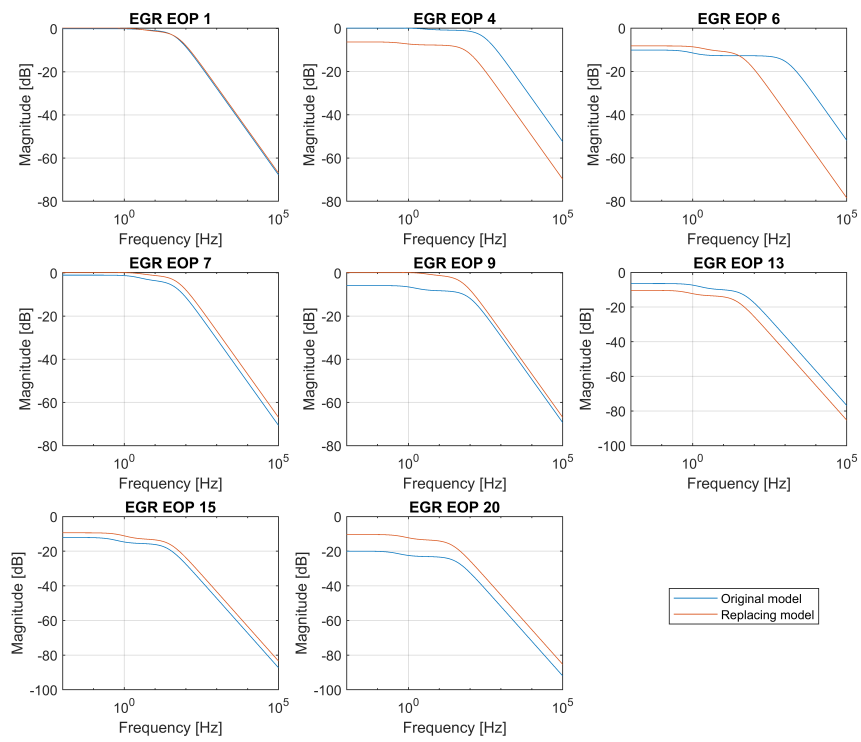


Figure 5.6: Continuous SS magnitude Bode plot of the eight replaced original EOPs and their replacing CEOPs

As shown in Figure 5.6, Bode plots do indeed fall after a given threshold frequency, ranging from 5 to 50 Hz , beyond which any given higher frequency input is filtered by the engine air-path; this result goes hand in hand with the typical behaviour of the vast majority of the physical systems, that can be assimilated to a low pass filter.

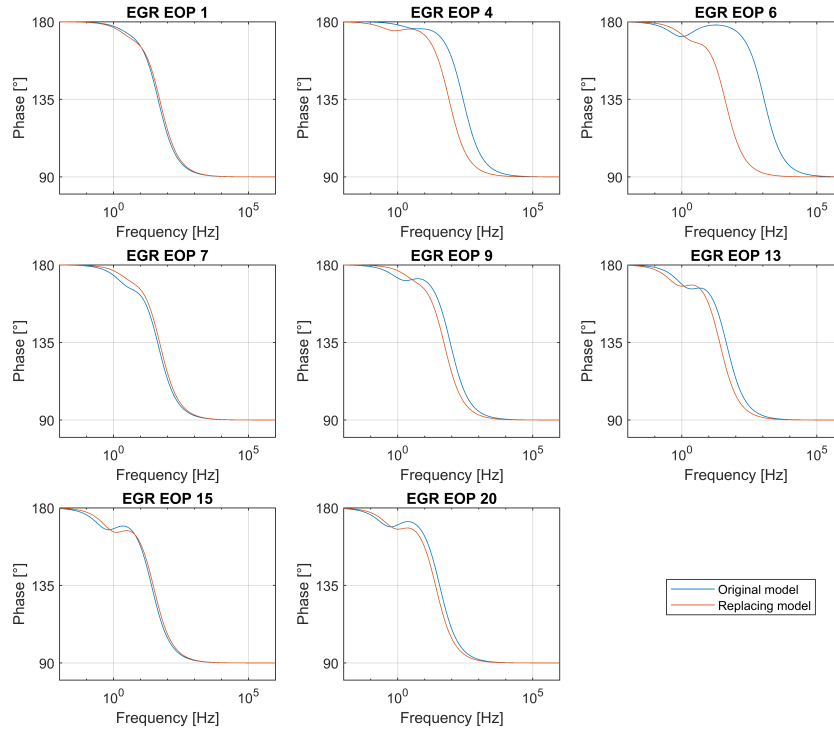


Figure 5.7: Continuous SS phase Bode plot of the eight replaced original EOPs and their replacing CEOPs

Bode phase charts, presented in Figure 5.7 do not show major misalignments between original and replaced models, A separate mention is given to EOP n. 6, where an inversion of zero and pole occurs, causing the bump in the diagram. As discussed, EOP n. 6 is, indeed, to be considered as a borderline replacement: a possible parallel study on the control behaviour obtained without its replacement may be brought on.

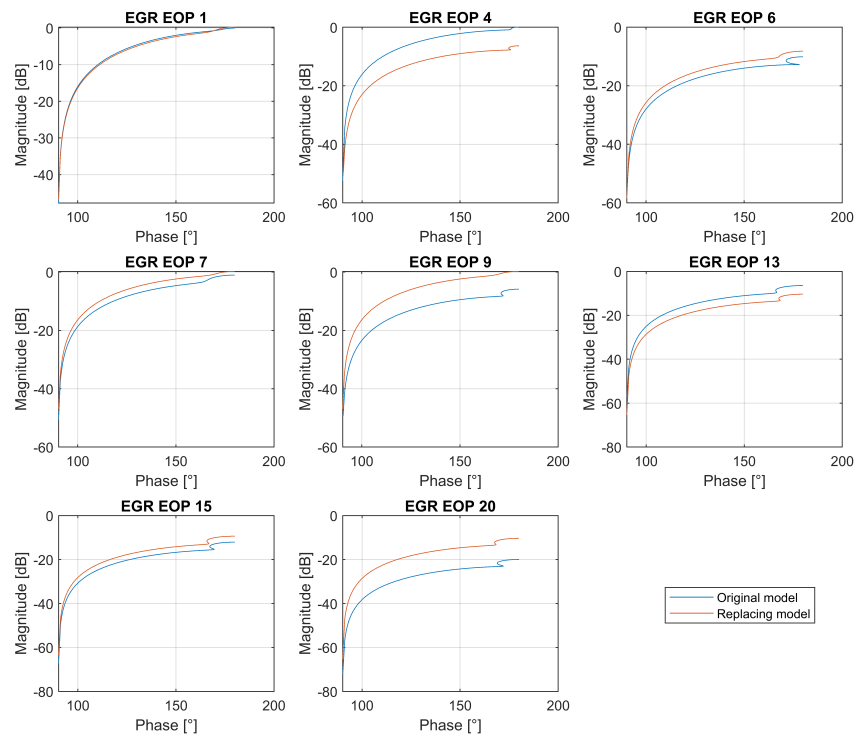


Figure 5.8: Continuous SS Nichols plot of the eight replaced original EOPs and their replacing CEOPs

Analysis of Nichols charts, provided in Figure 5.8, shows once more how the general shape of the identified plants is similar between COEPs and replaced EOPs. A last graph on the same topic is presented, collecting Bode magnitude plots of all the twenty EOPs and their replacing subset of twelve CEOPs. Result is illustrated in Figure 5.9 and is intended to help noticing the similarity of the models, that span across a 30 dB range in terms of steady-state gain; curve do indeed show similar pass-band frequencies, except for specific borderline cases.

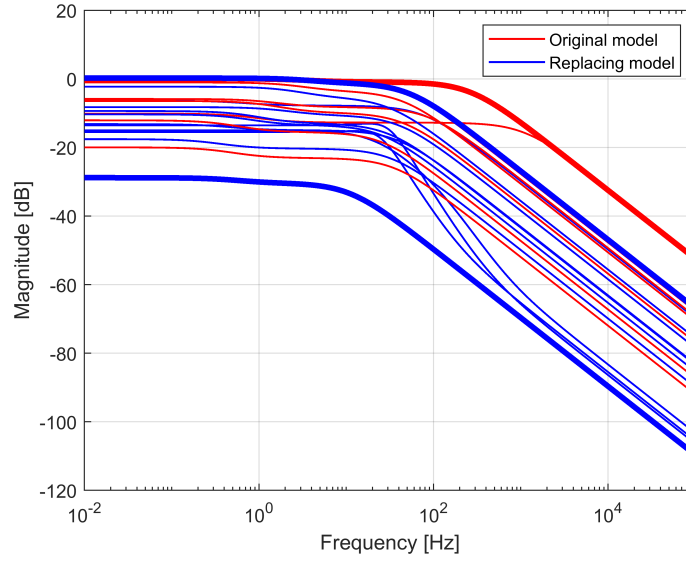


Figure 5.9: Superimposed continuous SS Bode magnitude plots of the twenty original EOPs and replacing CEOPs

Figure 5.9 shows the dispersion of the Bode magnitude plots from model to model. CEOP n. 16 corresponds to the lowest, thick, blue, Bode curve. This comes as no surprise, being CEOP n. 16 in the low speed ($< 1500 \text{ rpm}$) - low load ($< 1.5 \text{ bar}$) engine map subregion: here, for mechanical reasons that are explained in detail in Section 7.2, even a large EGR valve opening does not yield a parallel decrease in air mass flow rate. Upper Bode plots, on the other hand, are represented by CEOP n. 8, marked in blue, that replaces a total of three other models, namely n. 1, 7 and 9; not surprisingly, these points all lay in the high speed ($> 2500 \text{ rpm}$) - high load ($> 10 \text{ bar}$) engine map area where, again because of mechanical components-fluid coupling, a milder EGR actuation is sufficient to noticeably vary the air mass flow rate. CEOP n. 8, as mentioned, corresponds to upper thick blue line in Bode plot.

On the whole, CEOPs models enclose all the replaced EOPs, testifying this way the adequacy of the replacing procedure. Case of EOP n. 4, corresponding to thick red line in Figure 5.9 is in no way Unanticipated, being in turn replaced by a close CEOP model.

Graph in Figure 5.5 shows the zeros-poles placement in the continuous state-space order $n = 2$ models. This specific outcome demonstrates that the assigned parameters are not far from the ones assigned through ARMAX models.

5.2 Median CEOPs selection

A second attempt in discerning the most adequate CEOPs to use, so as to best suit the current engine state to its own plant model and to adequately control it through a tailored control action, is here performed.

Main idea of the proposed algorithm is to select a median-based averaged model for each EOPs cluster, that can therefore be as representative as possible of all the models in the cluster, instead of using an already existing CEOP; to this regard, an example is given.

Let $\Psi = \{EOP_1, EOP_2, EOP_3\}$ be a set of, *e.g.* SS models related to given operating points, belonging to the same cluster Ψ and therefore replaced by a given $CEOP_k$. Without loss of generality, we set $CEOP_k := EOP_1$. Let also \mathbf{z}_i , \mathbf{p}_i and \mathbf{k}_i be the vector triple of zeros, poles and gain of each model EOP_i . Key idea is now to replace $CEOP_k$ with a new model, $CEOP_{med}$, defined as the transfer function of numerator and denominator obtained as the *median* between \mathbf{z}_i , \mathbf{p}_i and \mathbf{k}_i for $i = 1, 2, 3$. The new model, $CEOP_{med}$, is therefore obtained sorting and taking the central point among zeros, poles and gains of the three *EOPs* and entails parts of their original dynamics. The model, clearly, has a similar structure to that of its replacing *EOPs*. The assessment of this concept is now given in Table 5.3, in the case of EOP_1 , EOP_7 , EOP_8 and EOP_9 , that were originally replaced by EOP_8 as they have all been assigned to the same cluster.

| EOP_i | BF $CEOP_8$ [%] | BF $CEOP_{med}$ [%] |
|---------|-----------------|---------------------|
| 8 | 86.1249 | 82.40 |
| 1 | 82.2250 | 84.24 |
| 7 | 75.1770 | 82.93 |
| 9 | 82.6510 | 82.84 |
| Median | 81.5445 | 83.10 |

Table 5.3: Fit percentages for $CEOP_8$ and $CEOP_{med}$ on SS models

Table 5.3 shows the fit percentages of the four datasets when modelled by $CEOP_8$ (and not by their own $CEOP_i$), to the left, and by $CEOP_{med}$, to the right. As it is possible to see, median-averaged CEOP selection gives overall slightly better fitting results, compared to the direct COEP model choice among the original four EOPs. It is, furthermore, noticeable that the small percentage fit loss occurred in benchmark case n. 8, is largely recovered in the remaining three cluster points. This happens as point n. 8, that was originally served by its own model, is now modelled by the median-based transfer function. Controllers of the other points, conversely, have been replaced by a new one that also entails part of their characteristics: their fit performance is consequently improved.

Median-based model, by and large, features a 2 percentage points improvement with respect to the original one. The trend is confirmed when applying same procedure to other EOPs clusters, with only minor variations.

Such pattern can be thus exploited defining, for each cluster, a $CEOP_{med}$ averaging its EOPs, obtaining therefore an improved model quality and a consequentially more robust control action. In the same way, a further extension of this concept is the computation

of the median of SS transfer function coefficients, instead of that of their zeros, poles and gains, or the usage of weighted averages to compute the same quantities, obtaining a $CEOP_{w,avg}$ as replacement of the original EOPs.

5.3 Benchmark selection

In this section, the very first step of the gain scheduling controller design is carried out and an overview of the required procedural steps is given.

The need for a progressive design, allowing for a constant refinement and tuning of the compensators parameters, has encouraged to split the design process in three separate phases, namely:

- single CEOP controller design;
- four CEOPs gain-scheduling;
- whole engine map gain-scheduling.

Each stage introduces a higher level of accuracy, as the progressively developed controller become tailored to tackle their corresponding engine areas.

At this step, the definition of a proper benchmark model, on which a first controller is built, is discussed. This single CEOP controller is not yet an example of gain-scheduling action and its architecture is not yet equipped with any additional control block. *Ratio* behind this procedure is to understand the limitations of this initial architecture, in order to best comprehend what the successive control development must be. Second and third controller design phase are presented in Chapter 7.

Among ARMAX and SS models, in the end SS ones are chosen so as to implement the control logics of the system. The reason for this coming from several points.

- SS models are slightly more robust with respect to ARMAX ones [31].
- SS models can be easily casted into TF models, thus being easily manageable when it comes to designing a tailored controller based on them.
- Just the model order has to be tuned, instead of separately tuning both numerator and denominator of the resulting transfer function.

With a view to comparing control results with a benchmark, a first outline of the fit performances of a given model, applied to all the other operating points, is shown. Core idea is that the benchmark point will provide a non-specific, however still fairly fitting, modelling and control performance.

The benchmark EOP is chosen so that it lies in the middle of the EOPs map and is as much representative as possible of the majority of the other EOPs; this can be seen in Figure 5.10, where the point n. 15, 1800 *rpm* and 6.76 *bar*, is highlighted.

The chosen CEOP is adequate to be the benchmark point of the entire operating range as, even if not perfectly centered, it is placed in a highly visited engine area: the vehicle is

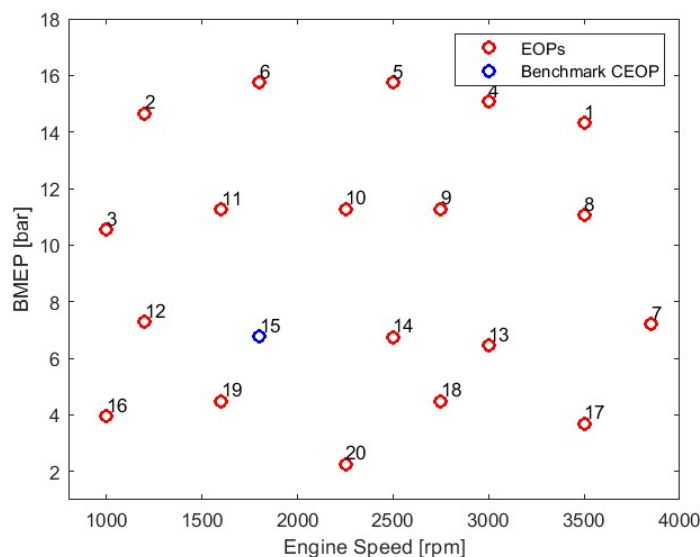


Figure 5.10: EOPs and benchmark point, case n. 15, in blue, at 1800 *rpm* and 6.76 *bar*

indeed unlikely to run for a long time span in high engine speed - high torque configuration, those areas being therefore less meaningful for generalized control quality assessment purposes, with respect to the selected one. Still, less visited areas have to be carefully investigated; this is done in detail in Chapter 7.

Another point that is worth to mention is that the benchmark CEOP does not belong to the CEOPs subset: this has been done for the sake of generality and so as not to privilege a CEOP or the other during the quality of control techniques assessment.

| Target EOP | Fit [%] | Target EOP | Fit [%] |
|------------|---------|------------|---------|
| 1 | 63.89 | 11 | 82.69 |
| 2 | 78.88 | 12 | 88.07 |
| 3 | 78.60 | 13 | 75.36 |
| 4 | 63.83 | 14 | 86.94 |
| 5 | 70.23 | 15 | 93.41 |
| 6 | 70.31 | 16 | 0.00* |
| 7 | 67.16 | 17 | 77.05 |
| 8 | 64.62 | 18 | 86.28 |
| 9 | 73.87 | 19 | 72.08 |
| 10 | 77.52 | 20 | 57.25 |

Table 5.4: Order 2 SS models EGR benchmarks with respect to EOP n. 15; case 16, using its own model, would yield an 88.3% correlation performance

In Tables 5.4 and 5.5, the fit percentages of EOP n. 15 model can be found. In one specific EGR operating point, n. 16, benchmark value of the own model of the EOP is also mentioned, since EOP n. 15 was not able to provide a sufficiently good approximation

| Target EOP | Fit [%] | Target EOP | Fit [%] |
|------------|---------|------------|---------|
| 1 | 90.55 | 11 | 96.19 |
| 2 | 96.52 | 12 | 89.09 |
| 3 | 93.11 | 13 | 93.45 |
| 4 | 91.60 | 14 | 96.07 |
| 5 | 92.31 | 15 | 98.57 |
| 6 | 94.75 | 16 | 20.28 |
| 7 | 92.28 | 17 | 95.69 |
| 8 | 91.89 | 18 | 96.37 |
| 9 | 92.99 | 19 | 89.06 |
| 10 | 94.78 | 20 | 92.41 |

Table 5.5: Order 2 SS models VGT benchmarks with respect to EOP n. 15

of the output signal, given the input, when using the corresponding validation dataset. This accords well with the EOP position: a low engine speed ($< 1500 \text{ rpm}$) - low $BMEP$ ($< 7.5 \text{ bar}$) operating point.

5.4 Benchmark single controller design

The benchmark point obtained in Section 5.3 is now used for control purposes, so as to acquire useful pieces of information, in order to calibrate the entire set of controllers to be used in the whole engine map. A first attempt is therefore performed adopting a single controller, whose application will span through the whole engine map, defined by engine speed and $BMEP$. The controller is designed basing on the engine plant identified model of EOP n. 15, here referred to as G_P . The model comes from the selection of a benchmark EOP, described in Section 5.3. It must be emphasized that such plant model has been identified on a given engine operational region, underlining that its corresponding controller should operate within this same region, so as to preserve the linear identified engine dynamics and to consequently obtain a satisfactory control action.

The adopted models are state space models of order 2, whose transfer functions are reported in 5.3 and 5.4.

$$G_{P,EGR} = \frac{-4.3424(s + 0.7101)}{(s + 26.07)(s + 0.4759)} \quad (5.3)$$

$$G_{P,VGT} = \frac{0.009089(s + 11.79)}{(s + 20.12)(s + 1.105)} \quad (5.4)$$

5.4.1 Control requirements

To design the control architecture, the following main requirements are considered, being, in the case of the EGR valve,

- overshoot, \hat{s} , that should not be greater than 15%;
- rise time, from 10 to 90%, set to $t_r = 0.7s$;
- settling time, within a 5% band, here set to $t_s = 1.3s$;
- perfect steady state step signals tracking;
- ramp signals tracking at steady state, with $\delta = 0.15$ tolerance;
- phase margin, not to be below 55° , to avoid instability risk.

Similar constraints are set for the VGT control, though being less restrictive than in EGR case. VGT valve, as explained in Chapter 1, has slower dynamics than the EGR one. VGT requirements are here listed.

- Overshoot, \hat{s} , not greater than 15%;
- rise time, from 10 to 90%, set to $0.9s$;
- settling time, within a 10% band, here set to $1.8s$;
- perfect steady state step signals tracking;
- ramp signals tracking at steady state, with $\delta = 0.25$ tolerance;
- phase margin, again not to be below 55° .

As it is possible to see from Equations 5.3 and 5.4, the models do not present poles in the origin, meaning one will be added so as to track ramp signals, similar to those actually applied when pressing the vehicle accelerator pedal. This pole is responsible for a steady-state perfect tracking of step signals, as well as for a finite error when tracking ramps. The chosen control architecture is a simple one, such as a lead-lag compensator or a PID compensator, where integral part is able to minimize the tracking error, until it becomes null; on the other hand, a small tolerance is accepted for the ramp signals tracking.

5.4.2 Used networks and control design

First computation that is done to build the controller is the conversion of the time requirements into frequency ones: a range of crossover frequency ω_c , of the open-loop system function, is therefore obtained. An $\omega_{c,1}$ is computed to satisfy requirement on the rise time and a second one, $\omega_{c,2}$, is set to account for the settling time: among them, the highest one is chosen as control parameter, thus $\omega_{c,target} = \max(\omega_{c,1}, \omega_{c,2})$. Such frequency constraint needs to be respected, so as to provide a satisfactory time response of the system; crossover frequency is obtained from Nichols chart, looking at the intersection between curve and x-axis, where magnitude is 0 dB ; same is done for the phase margin, computed as the difference between phase at 0 dB and -180° . A second target, being overshoot \hat{s} , is taken into account by drawing corresponding damping ellipses on the Nichols chart, being them a forbidden region where the controlled open-loop function should not lay, in order

to avoid too large overshoots or instability. Used networks will generally be an integral one, corresponding to the coefficient K_I , and a proportional one, K_P ; the latter will be largely used in VGT control, to improve tracking performance.

Requirement on ramp signals tracking is converted into a constraint on controller gain, the equation to be respected being 5.5.

$$|K_C| \geq \left| \frac{R_0}{K_P \delta} \right| \quad (5.5)$$

In Equation 5.5 K_C and K_P are, respectively, the controller steady state gain and the plant steady state gain; R_0 is the slope of the ramp to be tracked and δ represents the slope range inside which the controlled output variable must lay.

5.4.3 EGR control on benchmark EOP

Compensator of EGR EOP n. 15 requires a negative control gain, its sign being given by stability constraints; if the sign were to be positive, Nyquist stability criterion would not have been satisfied and the system would be unstable.

The need for a pole in the origin in the controller transfer function already brings to an initial shape of the open loop transfer function, in which a first trial gain $K_{I,EGR} = -1$. Nichols chart of the function with $G_{C,EGR} = -\frac{1}{s}$, multiplied by the plant transfer function G_P , is reported in Figure 5.11.

The curve, however not trespassing the design target magnitude ellipses, does not yield a satisfactory response time, being the crossover frequency ω_c too low. Iterative attempts are therefore performed to raise the gain of the control transfer function. This procedure is halted when reaching both a suitable response time and being at a tolerable distance from the afore-mentioned ellipses. The procedure is stopped when the Nichols chart curve is approximately tangent to the 0.25 dB ellipse. At this point, phase margin is measured, being 67° and overshoot is 4.5%; rise and settling time are also satisfied, being respectively 0.15 s and 0.29 s. Final controller transfer function is

$$G_{C,EGR} = \frac{-71}{s} = \frac{K_{I,EGR}}{s} \quad (5.6)$$

Resulting Nichols chart can be seen in Figure 5.11.

EGR control performances are shown in Section 5.5, where target is tracked both in slow and fast varying cycles; the tracking behaviour corresponds to the controller requirements: steady state is always reached and ramp signals are followed with only a minor delta, within reasonable tolerance. Overshoot is $\hat{s} = 5\%$ and is, thus, well below the imposed one. The control action efficiency deteriorates as the required engine cycle becomes more aggressive. Specifically, getting further from the linearity region to which the control was tailored, not only does the controller make a bigger effort to match the air mass flow target, but also does the physical model actually change, at the expense of the control action appropriateness.

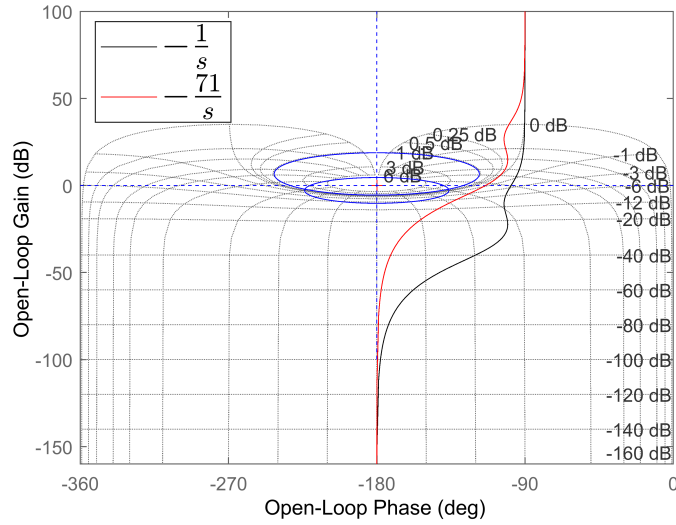


Figure 5.11: Nichols chart on EGR controller n. 15, highlighting the subsequent controller refinements

5.4.4 VGT control on benchmark EOP

VGT valve control behaviour fairly differs from the EGR case, especially due to the VGT valve longer response time: this can be noticed by the looser requirements that are set to the controller. Control scheme is anyway built following a similar procedure to that of the EGR valve, resulting in the selection of a compensator with an integral action, given by a pole in the origin, whose aim is to track ramp signals within a given tolerance, and a proportional one, that is given by the zero added to the transfer function for stability purposes. Frequency of the zero is set so as to cancel the pole of the plant transfer function. This technique will be applied, where possible, also in the design of the other CEOPs.

Eventually, magnitude is raised to speed up the response time. During this step, an adequate crossover frequency ω_C is reached, satisfying both rise and settling time, being respectively 0.73 s and 0.92 s. Overshoot of the step response is negligible and phase margin is equal to 98° .

Final VGT controller transfer function is given in Equation 5.7, where proportional and integral gains, $K_{I,VGT}$ and $K_{P,VGT}$, are highlighted. The same results are shown in Figure 5.12, where successive refinements of the original controller transfer function can be seen. Eventually, $K_{C,VGT}$ embraces the forbidden magnitude ellipses with its convexity, thus being far from the instability region.

$$G_{C,VGT} = 900 \left(\frac{1 + \frac{s}{1.1}}{s} \right) = \frac{900}{s} + 818.2 = \frac{K_{I,VGT}}{s} + K_{P,VGT} \quad (5.7)$$

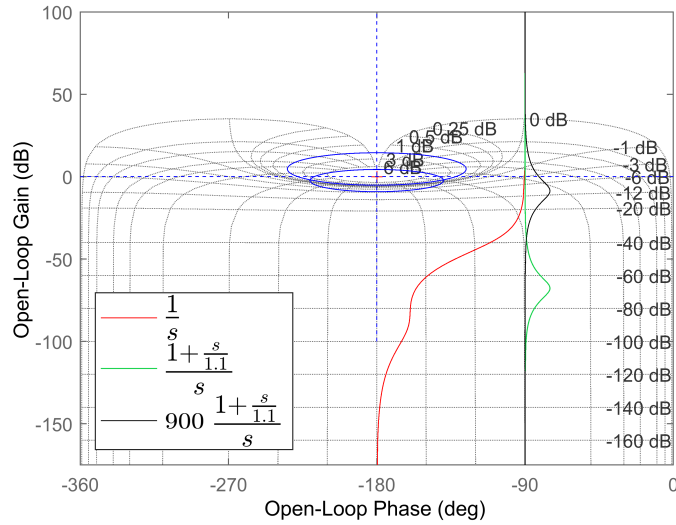


Figure 5.12: Nichols chart on VGT controller n. 15, highlighting the subsequent controller refinements

5.5 Control performance on EOP n. 15

This section illustrates the control outcome on EOP n. 15, featuring 1800 *rpm* per 6.76 *bar*; here, the control through mapped values, as defined by the ECU, is firstly given, then it is compared to the one based on the controllers designed in Section 5.4 and reported in Table 5.6

| Actuator | G_P | K_I | K_P |
|----------|---|-------|-------|
| EGR | $\frac{-4.3424(s + 0.7101)}{(s + 26.07)(s + 0.4759)}$ | -71 | 0 |
| VGT | $\frac{0.009089(s + 11.79)}{(s + 20.12)(s + 1.105)}$ | -900 | 818.2 |

Table 5.6: Plant models and proportional and integral gains of EGR and VGT controllers, for benchmark case n. 15, featuring 1800 *rpm* and 6.76 *bar*

Target variables to be tracked are obtained through experimental maps, directly coming from engine manufacturer and test-bank experiments. Maps are built in SimuLink environment and fed with engine speed and *BMEP* and give as output either target air mass flow rate or boost pressure. Inputs come from GT-Power simulation software and output is tused as target in the control logic. A SimuLink map scheme is given in Figure 5.13 for boost pressure target output.

Figure 5.13 already anticipates the key role that is played by the two input signals. An adequate signal treatment is responsible for a realistic target signal and, consequentially, for a functional controller.

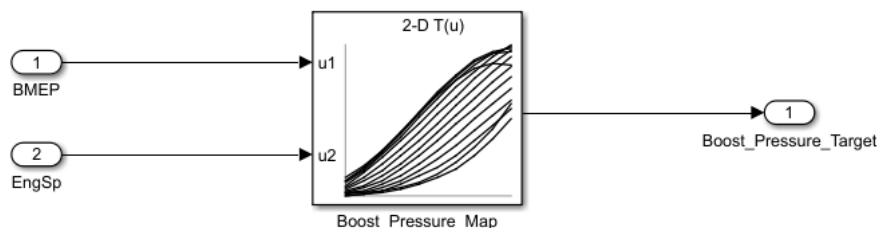


Figure 5.13: Mapped target boost pressure, obtained from *BMEP* and engine speed, in turn coming from GT-Power

Testing of the controllers, especially in VGT case, has immediately brought on the topic of windup, as VGT actuation frequently operates close to saturation and is consequentially prone to incurring in windup phenomena, with long inactivity time spans. The control architecture is therefore enriched of an anti-windup scheme, that zeroes the integrator term of the controller when given conditions are satisfied. The following control outcomes, visible from 5.5.2 to 5.5.5, refer to a control logic to which a conditional integration anti-windup mechanism has been added. A detailed study of the adopted anti-windup mechanisms is given in Chapter 6, where more schemes are presented and mutually compared.

The compensators are further equipped with conditional integration anti-windup mechanism, embodied in integrator block, compliant to the MISRA[39] guidelines. To further speed up the control action, the error zeroing is performed upstream the integrator and not downstream, as in the theoretical example presented in Section 6.4. This has valuable results especially within the EGR control, where the controller transfer function G_C is a simple integrator. Here, the downstream zeroing in case of actuator saturation would have led to a non-zero integrator outcome, leading to an unchanged control action, not able to track the reference anymore. Conditional integration is chosen among the different anti-windup architecture as it is the most reliable in terms of intervention speed and it is targeted for controllers that can feature a PID form. When this latter hypothesis were to fall, a generalized architecture would be used.

5.5.1 Test sequences outline

The fed test sequences are four and are catalogued as here described.

- Calm test sequence: *BMEP* and engine speed vary one at a time, ramps are slow, values do not get far from linearity range of EOP n. 15.
- Moderate test sequence: *BMEP* and engine speed vary one at a time, ramps are moderately fast, values get out of linearity range of EOP n. 15.
- Aggressive test sequence: *BMEP* and engine speed vary contemporarily, ramps are more aggressive, values do not get far from linearity range of EOP n. 15.

- Pedal-driven test sequence: cycle is given providing to the GT model the accelerator pedal and engine speed experimental traces, thus also affected from noise, simulating a realistic input signal; load and engine speed vary contemporarily, with variable slope ramps, values get out of linearity range of EOP n. 15.

Graphs in Figure 5.14 show the afore-mentioned engine cycles, used to assess the compensators.

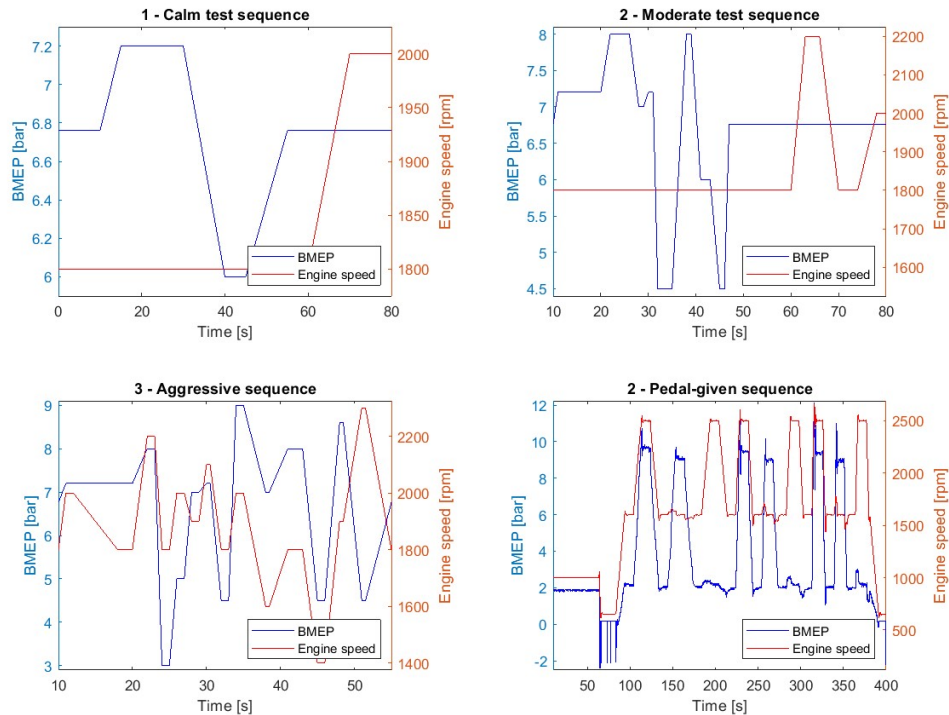


Figure 5.14: Assessment test sequences: from left to right and from top to bottom, in order, calm, moderate, aggressive and pedal-given engine cycles

5.5.2 Tracking - Calm test sequence

An outline of the tracking performances of the benchmark controller is now given, beginning from the calm engine test sequence. Figures 5.15 and 5.16 show different performances obtained using, respectively, the mapped EGR and VGT values or the ones chosen by tailored controllers. The comparison between the two graphs highlights an improvement in the tracking performance when the controller action is added to the mapped valve values, justifying the presence of the controller. The same situation occurs for both the EGR and the VGT; performance-wise, no major overshoots are seen and tracking is definitely better with controller, with respect to mapped values, that almost constantly show a delta between target outputs and actual ones. Controller actuation, however, still shows an

intense noise, that is attributable essentially to the imperfect gains of the control action and to the lack of any pre-processing to the engine speed and *BMEP* signals entering the compensator.

IMAP tracking is not perfect in the second half of the calm test sequence, as the VGT actuation gets saturated.

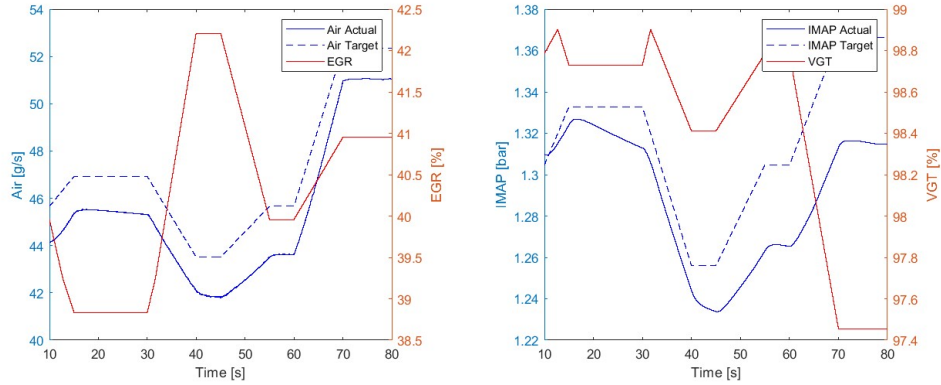


Figure 5.15: Control performance, with EGR and VGT mapped values, on calm test sequence, see 5.14

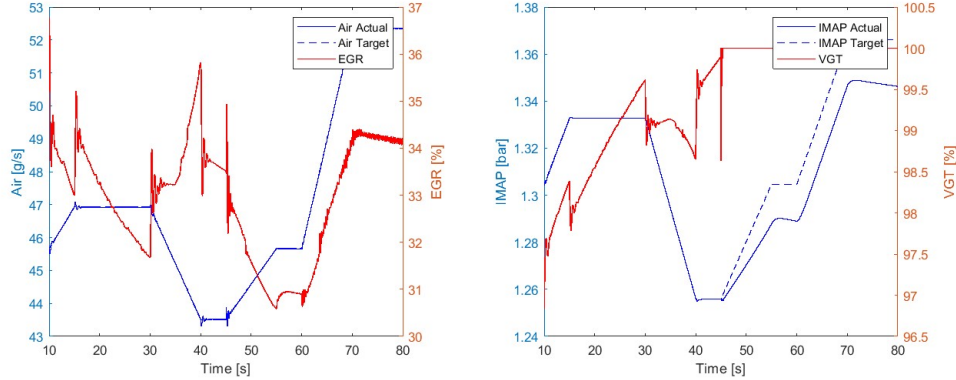


Figure 5.16: Control performance, with EGR and VGT controllers, on calm test sequence, see 5.14

5.5.3 Tracking - Moderate test sequence

Second set of measurements, presented in Figures 5.17 and 5.18, describes the control outcome when target variables start to go beyond linearity ranges and quickly vary, requiring, at least theoretically, a more aggressive control action. Applied test sequence is the moderate one. Here, again, mapped EGR and VGT positions fail to adequately track the target pressure and air flow quantities; conversely, controllers give satisfactory tracking results,

with limited overshoots occurring only occasionally and with an almost perfect tracking otherwise. Traces of chattering can be seen in the controller action, mostly in the EGR case. Besides, too fast variations in the actuation occur, for both EGR and VGT.

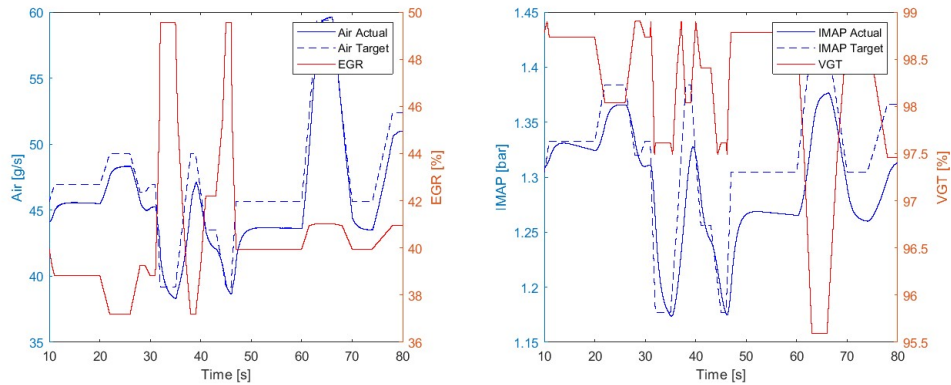


Figure 5.17: Control performance, with EGR and VGT mapped values, on moderate test sequence, see 5.14

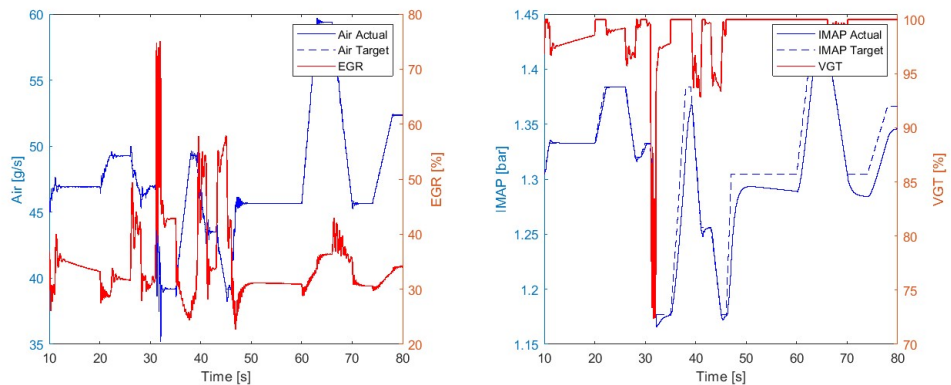


Figure 5.18: Control performance, with EGR and VGT controllers, on moderate test sequence, see 5.14

5.5.4 Tracking - Aggressive test sequence

Aggressive test sequence, with both the input quantities contemporarily varying, at a fast rate, yields the tracking results shown in Figures 5.19 and 5.20, respectively outlining mapped and controlled variables performances.

Though, on one side, mapped values keep giving a fairly good target tracking, especially for the EGR actuator, the same cannot be said for the controllers. Their usage brings decent tracking, however with noticeable overshoots, mostly in correspondence to engine speed/*BMEP* values laying out of the linearity range of EOP n. 15, as well as large chattering in the set actuator positions. This would not be accepted physics-wise, as such

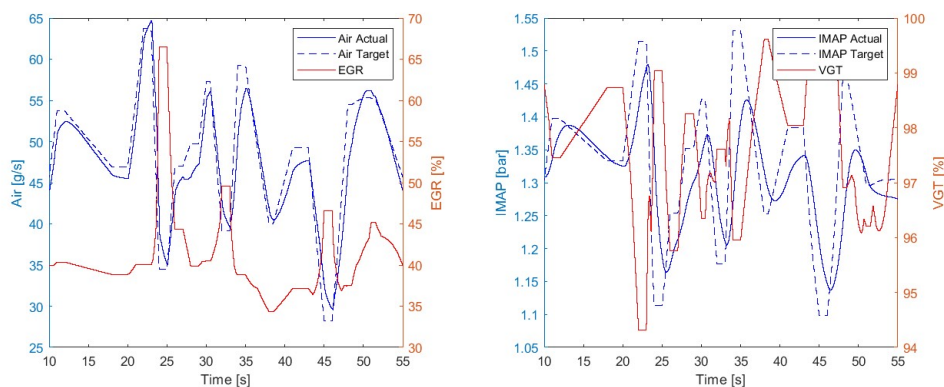


Figure 5.19: Control performance, with EGR and VGT mapped values, on aggressive test sequence, see 5.14

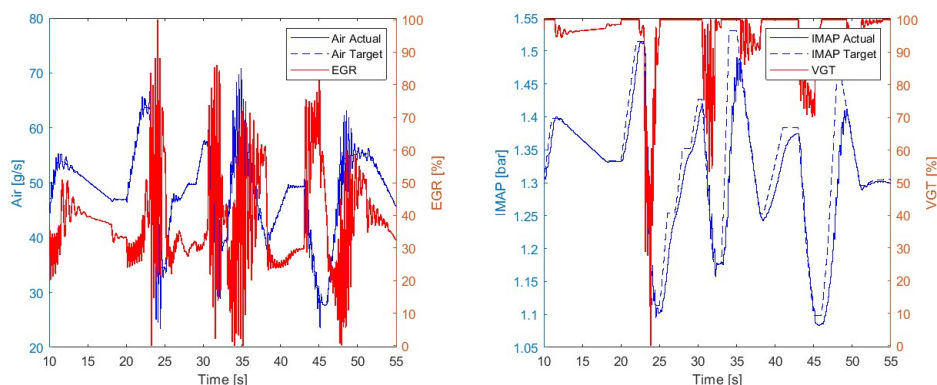


Figure 5.20: Control performance, with EGR and VGT controllers, on aggressive test sequence, see 5.14

requirements would largely hinder the mechanical actuators, progressively wearing them. At the same time, mechanical actuators cannot provide an infinitely fast actuation, making the suggested control action unrealistic: actuators do have, indeed, a maximum response speed that has to be respected.

To address this issue, the exploitation of a three-cycles averaged input engine speed and the reduction of EGR controller gains are proposed and results can be seen in Figure 5.21. As far as the control logic is concerned, the averaged engine speed causes the inputs to be smoother and less prone to unnecessary oscillations; in the end, this results in a definitely better tracking of the air mass flow rate \dot{m}_{air} and of the boost pressure, the $IMAP$. The second performed adjustment acts on the EGR controller transfer function, $G_{C,EGR}$, whose gain is reduced by a 0.7 factor: this is done since, allegedly, an aggressive controller is responsible for an in turn excessive response, that is sensitive to even small variations in input parameters. Not least, the faster the response, the higher the probability ripple in the output occurs; controller is overall more robust. Results of these changes can be seen in Figure 5.21: indeed, the applied modifications cause a remarkable smoothing, both in

the control actions and in the targets tracking.

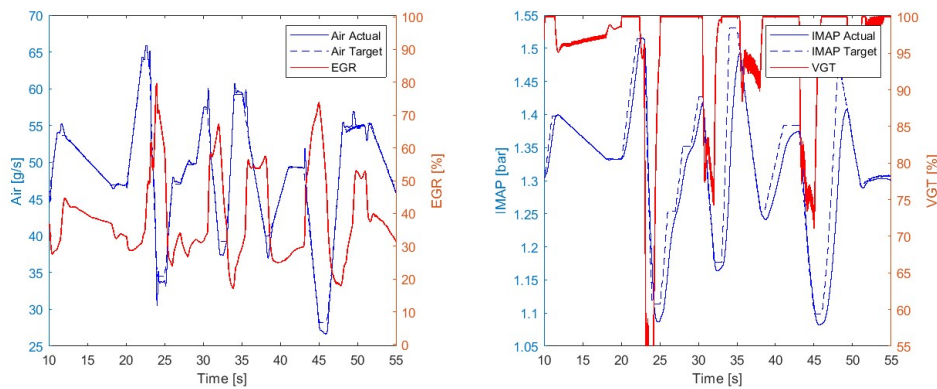


Figure 5.21: Control performance, with EGR and VGT controllers, on aggressive test sequence, see 5.14; EGR controller gain is reduced and averaged engine speed is fed

5.5.5 Tracking - Pedal-given test sequence

Last engine cycle to be studied for the validation of the PI compensators for EOP n. 15 is a pedal-given signal, characterised by noise corrupted inputs, as well as variable slope and height engine speed/ $BMEP$ ramps. Target signals, owing to the different generation of engine speed and $BMEP$, are the first ones showing a significant ripple, coming from the non-idealities of the plant itself.

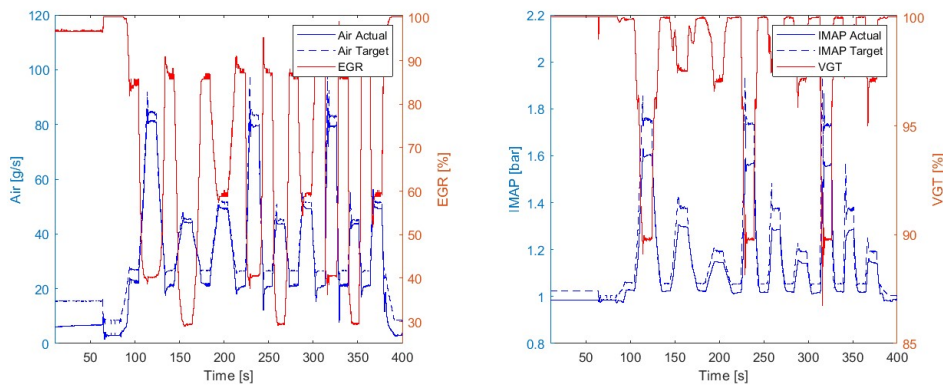


Figure 5.22: Control performance, with EGR and VGT mapped values, on pedal-given test sequence, see 5.14

Proposed control results entail a comparison between mapped values control with and without averaged engine speed, in Figures 5.22 and 5.23, and the control performance when EGR and VGT compensators are used, with reduced EGR G_C gain, in Figure 5.24. As expected, mapped values relying on an averaged engine speed give an output that is slightly closer to the target quantities, furthermore, compensators guarantee a sufficient

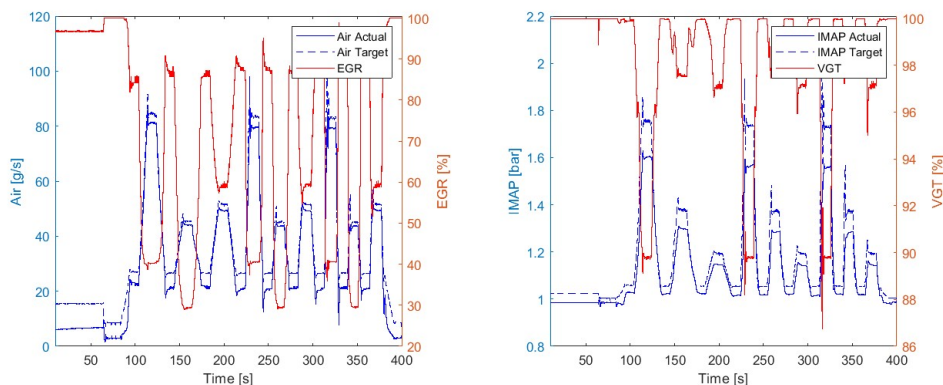


Figure 5.23: Control performance, with EGR and VGT mapped values, on pedal-given test sequence, see 5.14; averaged engine speed values are fed

tracking performance, notwithstanding the fast variations in the input parameters. Steady states values are not always reached, mostly due to actuators saturation or too fast required dynamics.

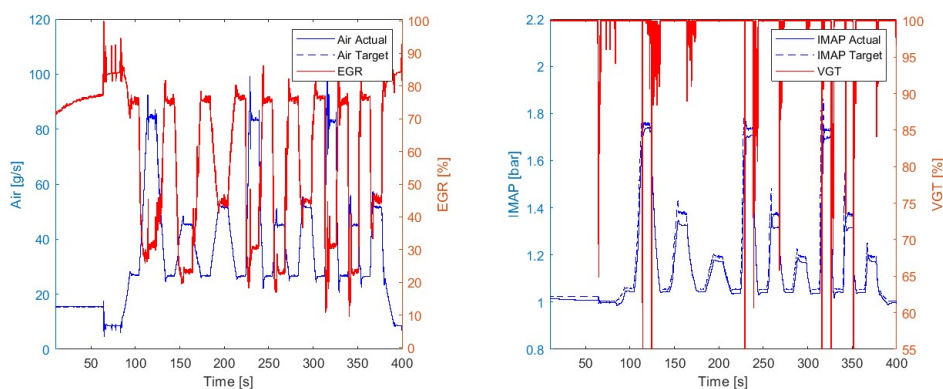


Figure 5.24: Control performance, with EGR and VGT controllers, on pedal-given test sequence, see 5.14; EGR controller gain is reduced and averaged engine speed is fed

5.6 Results and additional control components

This last section investigates the outcomes of the control action basing only on benchmark model n. 15. The testing has served as a basis to understand what networks have to be added to the control logic, depending on the control constraints.

Initial benchmark controller has overall achieved a satisfactory target signal tracking, for both air mass flow rate and *IMAP*. Such results decay progressively when feeding the

control scheme with more aggressive inputs. This can be noticed especially with aggressive test sequence, shown in Figure 5.20. The controller behaviour deviates from a sufficient performance immediately after engine speed is swept out of the 1800 ± 200 rpm range. When going beyond it, controller gains are too high and thus generate more chattering. When going below, situation is less severe, though still the actuation suffers from the previously introduced ripple. Moreover, frequent spikes in the actuation point out that the two target-defining signals, engine speed and load, are in turn affected by noise. This causes in turn the corruption of the target signal and an inadequate control action. These issues are effectively tackled with the pre-filtering of the input signals, by imposing a three-cycles average on engine speed and by reducing EGR controller gains by 70%. Results of these are a much better tracking of aggressive and pedal-given test sequences.

A further key feature, firstly emerging in Figure 5.16, is the presence of actuation saturation periods. This phenomenon, mostly occurring in VGT actuation system, owes to the impossibility of physically tracking given *IMAP* combinations, with the present mechanical components. The presence of recurring saturation phenomena is the motivating reason for the addition of an anti-windup mechanism in both the control logics. This topic is faced in Chapter 6, where multiple anti-windup solutions are considered.

Eventually, the introduction of bumpless filters to mitigate the sudden change from a gain to the other is brought to the attention. This behaviour will be present when designing the gain-scheduling control action, involving more CEOPs, described in Chapter 7. Frequent spikes phenomenon is however similar to that caused by the noisy input signals: in both cases, actuation sudden spikes are generated. The insertion of bumpless schemes to mitigate the issue is presented in Chapter 7 and follows a similar *ratio* to that outlined in 5.5.4, where moving average blocks are introduced in the SimuLink scheme to pre-filter the engine speed control input.

Chapter 6

Anti-windup Architectures

From tests performed on VGT controller in Section 5.4, it was already possible to notice an evident windup phenomenon, whose influence grows when the EGR valve action is coupled to that of the VGT control. *Integral windup*, defined as the error accumulation in the integral term of any controller or, more generally, the *reset windup*, still occurring when the control actuator, once the saturation limit is reached, yields an error accumulation into the controller, that is then discharged in a long time. Not being able to give a stronger control action than a given threshold, the accumulated error takes time to be brought back to zero, resulting in a poor and slow control [35][37].

These occurrence can be effectively targeted through an anti-windup device, that detects the windup, zeroing the integral error once it starts either

- decreasing, in case the upper saturation of the actuator is reached;
- increasing, thus going back to zero, but from negative values, in case the lower saturation of the actuator is reached.

This additional architecture depends on two inputs, here listed.

- Difference between saturated output and controller output.
- Target error on the output variable, being either \dot{m}_{air} or $IMAP$, when the considered actuation is the EGR or the VGT, respectively.

Provided output is the zeroing of the target error, when windup conditions occur, through a back-calculation architecture. Full controller is depicted in Figure 6.1 and, in Figure 6.2, an insight of the anti-windup mechanism is given. It is, lastly, worth to mention that VGT standard value is for the moment set to 99.11%, being the mapped ideal value when engine is running at 1800 *rpm* - 6.76 *bar*, being EOP n. 15.

The architecture, once received the two previously described inputs, zeroes the target error when, if out of the actuator feasibility range, the target error decreases in absolute value. This way, the controller is able to instantly reset a proper control action, without waiting for the discharge of the integral error.

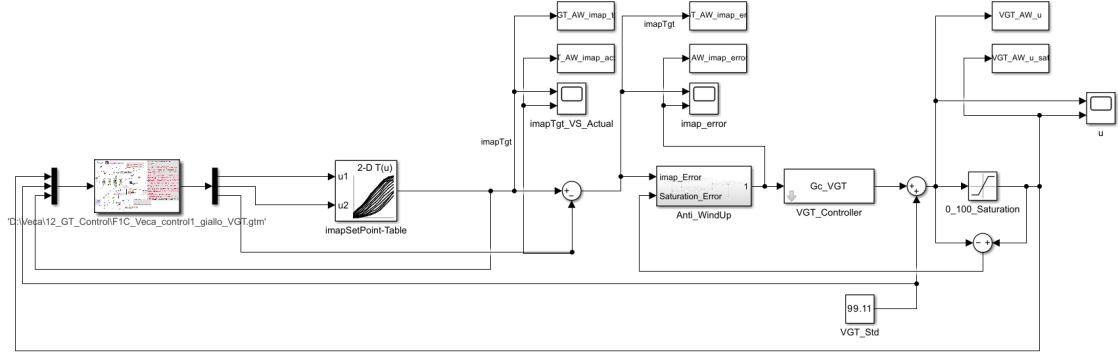


Figure 6.1: VGT controller scheme, with anti-windup architecture and standardized VGT fixed point

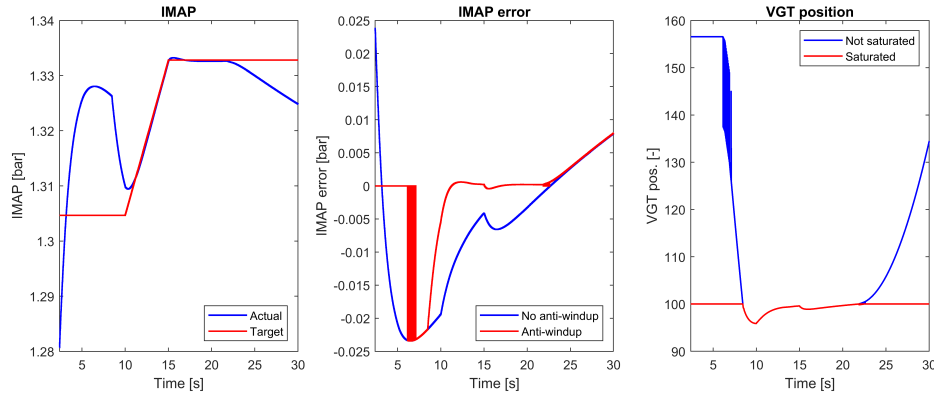


Figure 6.2: Anti-windup architecture, defined through boolean operators, here represented for the VGT control

6.1 Baseline architecture

This first architecture is applied modularly for both the EGR and VGT controllers. Specifically, only VGT anti-windup action is presented as it is more critical, given the control action, frequently close to the saturation limit and given the macroscopic effect the windup has on the tracking performance.

For the sake of completeness, boolean decisional logic of the anti-windup module is provided in Table 6.1, where $e_{track}(t)$ stands for target error at time instant t .

VGT compensator transfer function is given in Equation 6.1; the function has been obtained in .

$$G_{C,VGT} = \frac{900}{s} + 818.2 = \frac{K_{I,VGT}}{s} + K_{P,VGT} \quad (6.1)$$

In terms of control performance, first an overview of the windup phenomenon is presented in Figure 6.3; left chart represents target $IMAP$ vs the actual one; middle chart

| Actuator saturation | $ \dot{e}_{track}(t) $ | $e_{track}(t)$ zeroing |
|---------------------|------------------------|------------------------|
| No | - | No |
| Yes | > 0 | No |
| Yes | < 0 | Yes |

Table 6.1: Boolean decisional logic of baseline anti-windup architecture

shows the *IMAP* tracking error; to the right, VGT output command $u(t)$ and saturated command $u_{sat}(t)$ are given.

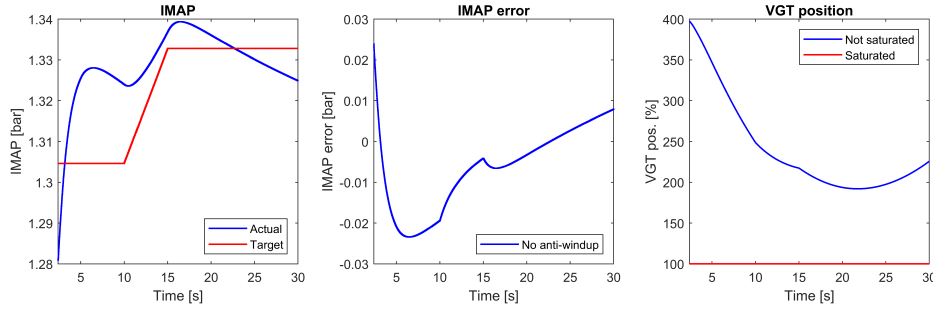
Figure 6.3: *IMAP* target vs actual value, *IMAP* error and rack position, *without* using anti-windup architecture on VGT

Figure 6.3 shows how the controller is substantially unable to track the required *IMAP*. VGT actuation is permanently saturated: no control is exerted on the boost pressure.

The same graph is then obtained equipping the controller with anti-windup baseline architecture: the very same variables are hence shown in Figure 6.4. Left chart represents target *IMAP* vs the actual one; middle chart shows the *IMAP* tracking error, comparing it between *without* and *with* anti-windup zeroing logic. To the right, VGT output command $u(t)$ and saturated command $u_{sat}(t)$ are again given.

Figure 6.4 shows how the controller now zeroes the *IMAP* error, not making it yield any additional contribution to the integrator.

It is evident that, employing such anti-windup structure, an *IMAP* tracking is achieved (see left graph) and the valve does not get stuck at its maximum opening for too lengthy an amount of time. Indeed, VGT position plot of Figure 6.3 shows VGT actuator is always saturated at maximum value when no anti-windup architecture is added. Same would happen when going below valve opening lower threshold.

An enlargement of the same graphs is now provided in Figure 6.5, where the benefits of adopting an anti-windup logic are evident. The focal point of the action is time horizon between $t = 2.4$ s and $t = 30$ s. Here, as tracking error $|e_{track}(t)|$ decreases, at $t \approx 6$ s, $e_{track}(t)$ is zeroed: this enables, slightly after, the exit of the actuator from the saturation region. The anti-windup logic, anyway, is not able to eliminate the fast transition from zeroed error to error actual value, visible for $t \approx 6.5$ s; furthermore, chattering in VGT

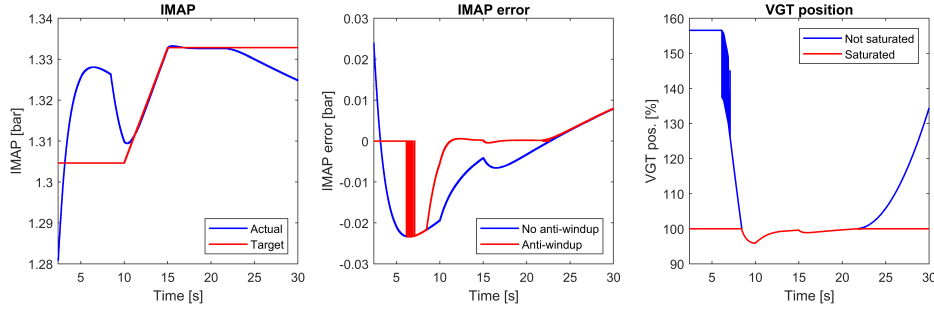


Figure 6.4: *IMAP* target vs actual value, *IMAP* error with and without anti-windup and rack position, when using baseline anti-windup architecture on VGT

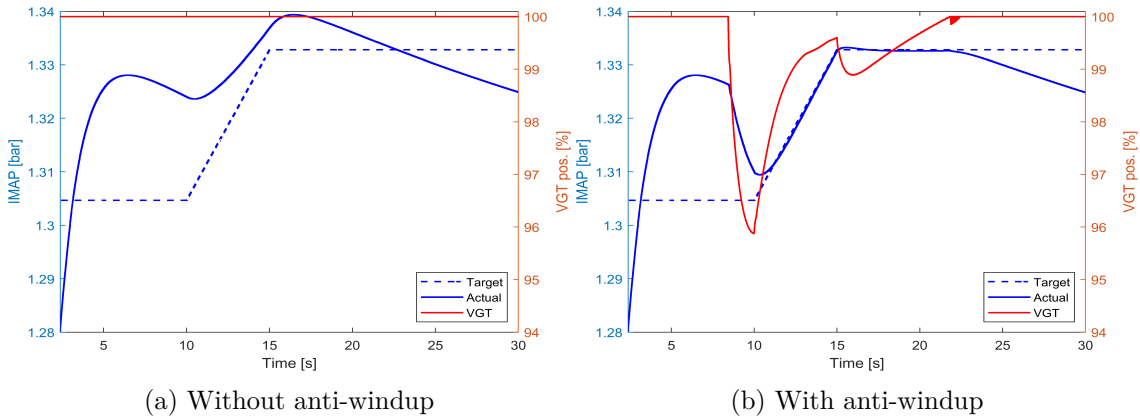


Figure 6.5: *IMAP* target vs actual value and rack position, without and with AW baseline architecture

control action is present and is visible from Figure 6.4 at time $t \approx 6.5$ s, even though not being visible, as it occurs in the actuator saturation region. Inability to track the signal at $t \approx 22$ s, resulting in windup, is mostly due to a further saturation phenomenon, that has not been counteracted by the AW logic yet.

Final outcome of the process is a much better signal tracking, compared to the unresponsive action of the controller without any AW mechanism.

6.2 Moving average smoothing

Solution to the chattering problem affecting the VGT rack position, presented in Figure 6.4, third graph, are illustrated. Chattering problem may hinder the functioning of the mechanical component if going below the actuator saturation limit, thus asking too fast a control action. To avoid possible mechanical wear, different possibilities are studied. First one is to apply a moving average to the output target error, with a view to smoothing the signal, avoiding the ripple in the control action. For this purpose, an averaging between 10 samples, thus exactly 0.1 s time, is used. Activation logic, given the smoothed

integral error signal, remains the same as in Table 6.1. SimuLink scheme of the controller is proposed in Figure 6.6; results can be observed in Figure 6.7.

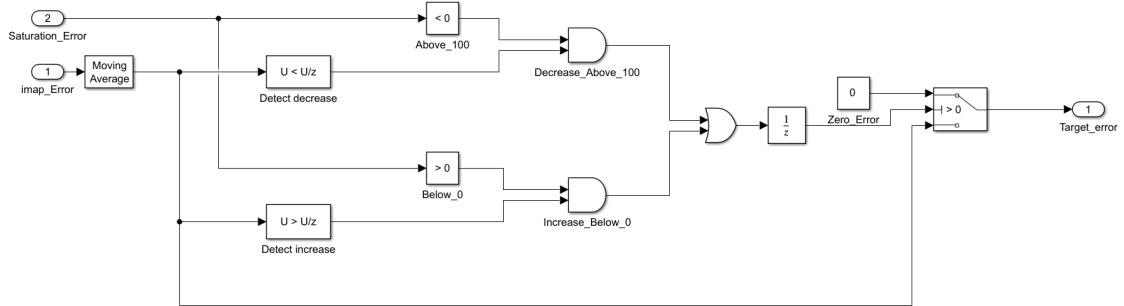


Figure 6.6: Anti-windup architecture, with moving average on target error, here represented for the VGT control

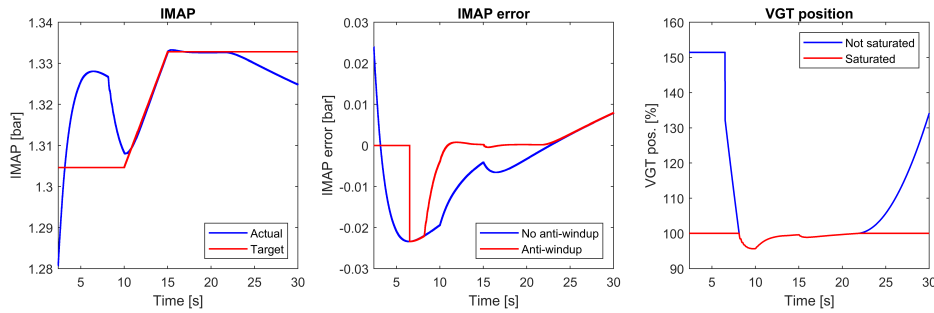


Figure 6.7: *IMAP* target *vs* actual value, *IMAP* error in with and without anti-windup and rack position, anti-windup architecture with moving average, on VGT control

Figure 6.7 clearly shows an improvement in the smoothness of the control action, that now benefits from a totally removed *chattering*. To this, target tracking speeding up is added. Indeed, new tracking, visible in Figure 6.8, occurs ca. 0.5 s before than when using simple baseline architecture. Further improvements in tracking response can be seen in Sections 6.3, and .

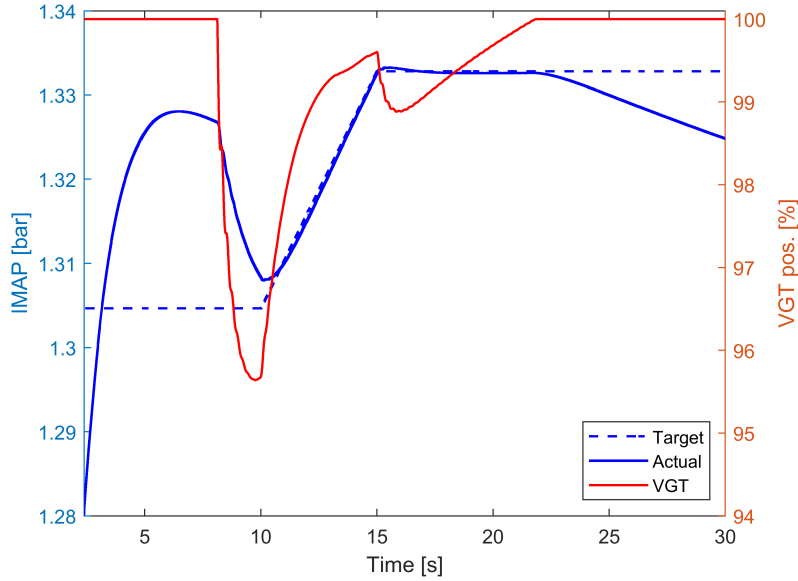


Figure 6.8: *IMAP* target vs actual value and rack position, anti-windup architecture with moving average, on VGT control

6.3 Zeroing activation thresholds

A further implemented anti-windup architecture makes use of thresholds, for the decisional logic enabling or disabling the integrator zeroing. This has an impact on the response time, becoming much faster. More in detail, the target error is not brought to zero when the integration error starts to be discharged, but *before*, within a given tolerance; activation logic summary is provided in Table 6.2, where activation condition is now dependent on derivative of $e_{track}(t)$ rather than on the integral error itself.

| Actuator saturation | $ \dot{e}_{track}(t) $ | $e_{track}(t)$ zeroing |
|---------------------|------------------------|------------------------|
| No | - | No |
| Yes | $\geq 10^{-4}$ | No |
| Yes | $< 10^{-4}$ | Yes |

Table 6.2: Boolean decisional logic of baseline anti-windup architecture

This architecture has the upper hand on previous ones, as it can, within certain limits, predict the decrease of the error and, therefore, is able to speed up the exit from stall of the control action. SimuLink scheme of the decrease detection block of the anti-windup architecture is reported in Figure 6.9, followed by a graphical overview of the control performance, seen, as usual, between the range 2.4 - 30 s, presented in Figures 6.10 and 6.11.

SimuLink scheme of Figure 6.9 is an modification of Figure 6.6, where the switch to the right has been replaced by the threshold target error zeroing. Zeroing threshold has been chosen iteratively, eventually selecting a 10^{-4} bar limit below which to zero the error.

Designed AW architecture outcome shows a much faster signal tracking: target *IMAP*

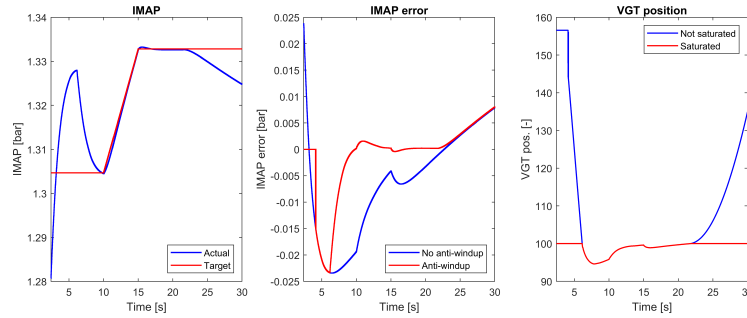


Figure 6.9: Anti-windup architecture, with 10^{-4} bar activation threshold on target error variation, represented for the VGT control

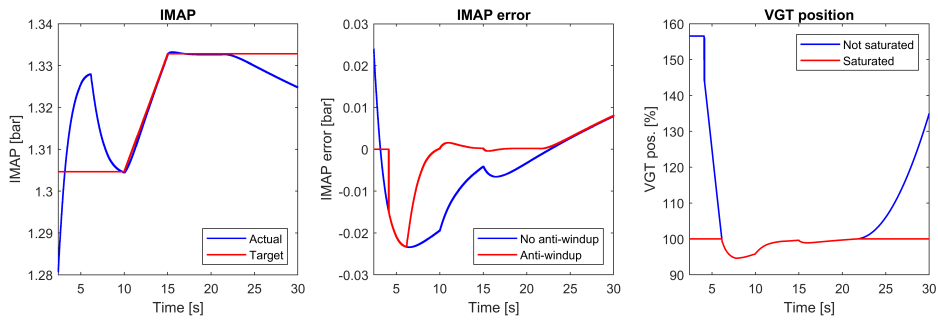


Figure 6.10: *IMAP* target vs actual value, *IMAP* error in with and without anti-windup and valve position, when using anti-windup architecture on VGT, with 10^{-4} bar activation thresholds

is successfully matched already at $t = 10$ s, compared to the 11 s characterizing the baseline AW and the 11.5 s without any AW architecture. VGT control action is essentially anticipated with respect to previous AW schemes.

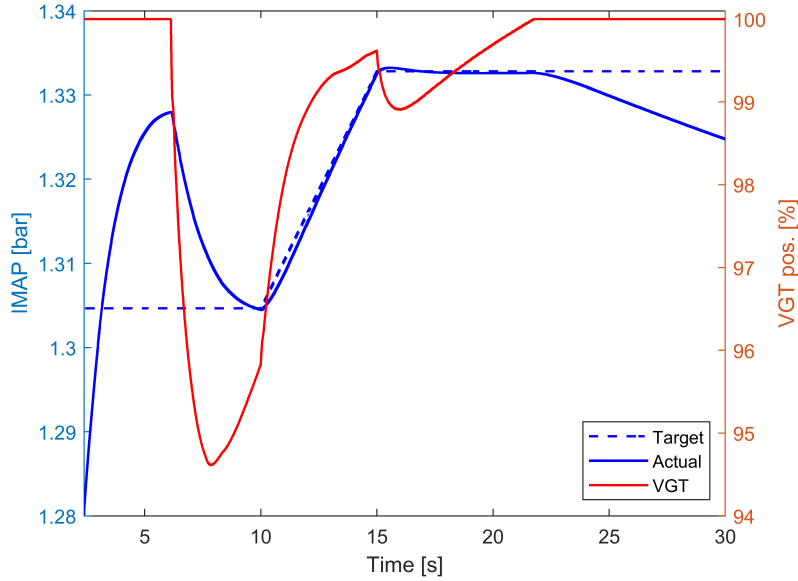


Figure 6.11: *IMAP* target *vs* actual value and rack position, when using anti-windup architecture on VGT, with 10^{-4} bar activation thresholds

6.4 Conditional integration

The implementation of anti-windup schemes has until now gone on using decisional logics, not dealing specifically with the control transfer function G_C . In this subsection, such transfer function is exploited, so as to build a mechanism that directly targets it and is built-in, rather than extrapolated from the status of the controller of the system.

This specific feature is reached splitting the transfer function G_C into two parts, in the VGT case an integral and a proportional one. This is done via simple mathematical computations, starting from the original *zpk-form* of the transfer function, as seen in Equation 6.2. EGR anti-windup logic is built in the same exact way, omitting the proportional term when not present.

$$G_C = \frac{K_C(1 + \tau s)}{s} = \frac{900(1 + \frac{s}{1.1})}{s} = 900 \left(\frac{1}{s} + \frac{1}{1.1} \right) = K_C \left(\frac{1}{s} + \tau \right) \quad (6.2)$$

This enables to isolate the integral term, $\frac{K_C}{s}$, from the rest of the transfer function. At this point, the anti-windup architecture is applied to the integral portion only, not affecting the remaining part of G_C . This leaves the controller with the proportional part only once the actuator saturation takes place and, as a result, control performance is largely improved. Main difference between this method and the previous ones is the complete discharging of the integral action when meeting the logic triggering requirements. The zeroing of the integral error $e_i(t)$ allows a much faster action, since windup state is abandoned much faster, being the integral error discharge time null.

The procedure, as seen here, can be applied to any PID controller having an integral term, hence a pole in the origin within its transfer function. A more general method, that can be exploited for *any* transfer function, will be illustrated in Section 6.5.

Controller scheme is represented in Figure 6.12 where, as observable, the original transfer function block, to be seen, for the sake of comparison, in Figure 6.2, has been replaced from a PI network, with anti-windup action on the integral term. In Figure 6.13 details of the decisional logic providing integral error zeroing are shown; logic is represented via a *switch* block in SimuLink environment.

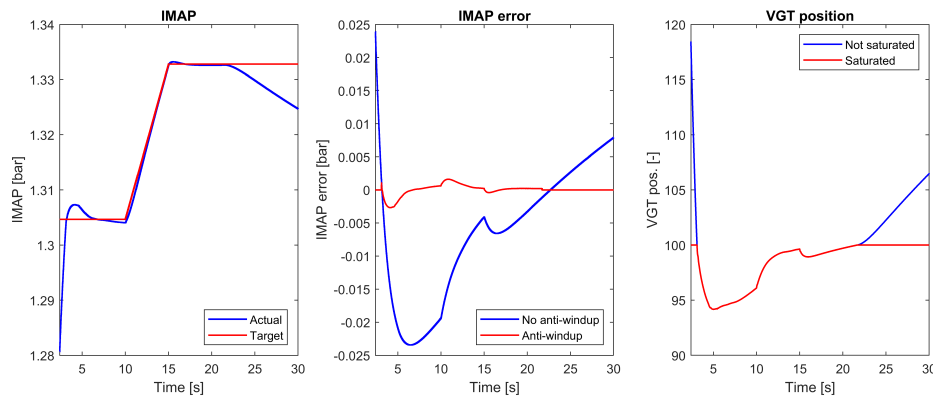


Figure 6.12: Anti-windup architecture through conditional integration, represented for the VGT control

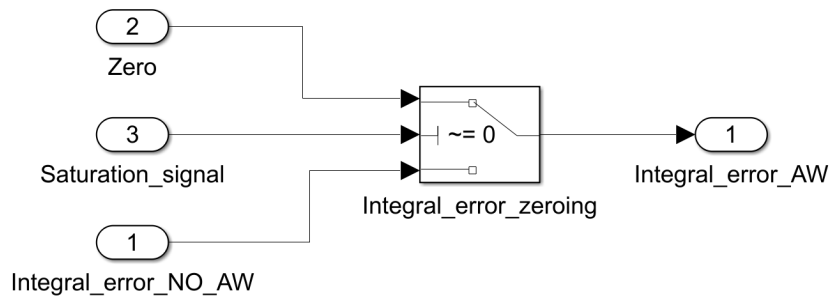


Figure 6.13: Anti-windup decisional logic in conditional integration, represented for the VGT control

Controller performance, on the very same timespan of the previous tests, is provided in Figure 6.14. Focusing especially on the left graph, it is indeed evident that the target *IMAP* is reached far earlier than in previous cases; furthermore, no ripple at anti-windup activation is present. VGT position is actuated in a noteworthy different way, practically never reaching saturation until the *BMEP* request significantly differs from the benchmark values.

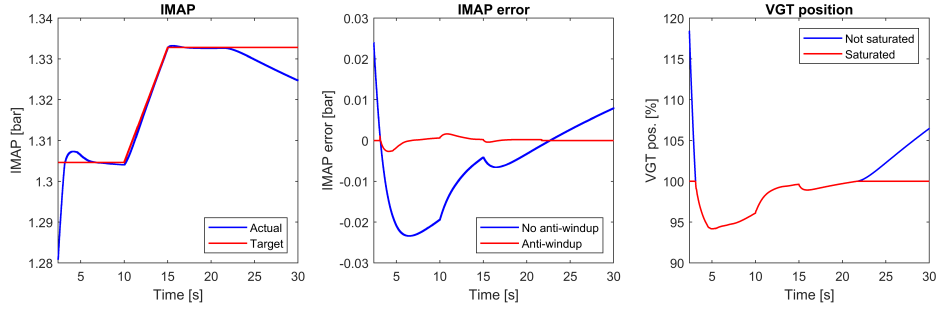


Figure 6.14: *IMAP* target vs actual value, *IMAP* error in with and without anti-windup and rack position, with conditional integration anti-windup architecture applied on VGT controller

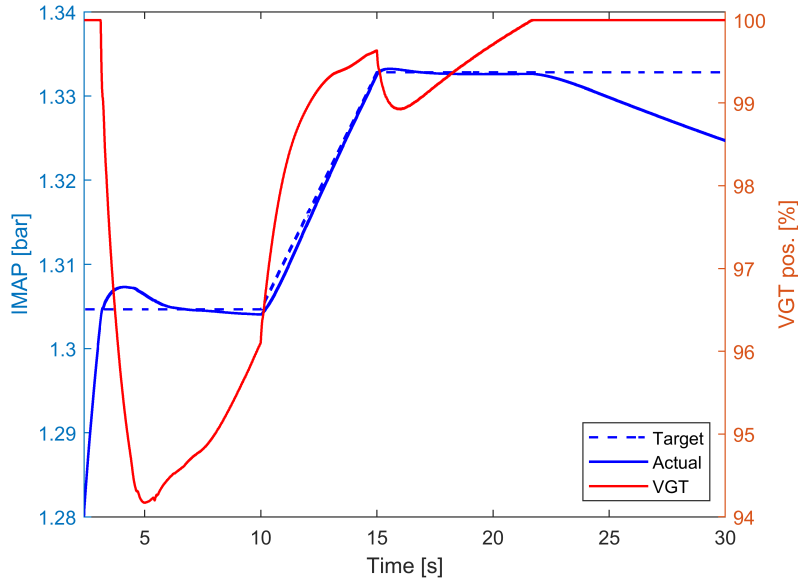


Figure 6.15: *IMAP* target vs actual value and rack position, with conditional integration anti-windup architecture applied on VGT controller

6.5 Generalized form architecture

One last anti-windup architecture is now provided. Advantage of this final technique is its versatility: the AW scheme does not have to be necessarily employed on PID compensators, but can address any transfer function, provided that given requirements are satisfied. Key idea of this anti-windup module is the usage of two different control transfer functions, one of them being the designed one, and the other one a variation of the former, defined by the entity of the actuator saturation. More specifically, G_C remains unchanged when actuator is within its operating range; conversely, when actuator is saturated in either of the two sides, countermeasures are taken. As it is possible to see from Figure 6.16, the model relies on the additional transfer function, $\Gamma(s)$, and on $N_C(s)$ and $D_C(s)$, being respectively the numerator and the denominator of compensator transfer function $G_C(s)$.

First thing to notice is that, however $\Gamma(s)$ is chosen, controller block in Figure 6.16 is equal to G_C when control action is not saturated, thus $u(t) = u_{sat}(t)$. Indeed, Equation 6.3, obtained equalling terms at node after first saturation block, circled in red in Figure 6.16, holds: this is shown following steps 6.3, 6.4 and 6.5.

$$u_{sat}(t) = u(t) = e(t) \cdot \frac{N_C(s)}{\Gamma(s)} + u(t) \cdot \frac{\Gamma(s) - D_C(s)}{\Gamma(s)} \quad (6.3)$$

Isolating $u(t)$ one gets

$$u(t) \cdot \frac{D_C(s)}{\Gamma(s)} = e(t) \cdot \frac{N_C(s)}{\Gamma(s)} \quad (6.4)$$

This, eventually, leads to

$$u_{sat}(t) = u(t) = e(t) \cdot \frac{N_C(s)}{D_C(s)} = e(t) \cdot G_C(s). \quad (6.5)$$

Equation 6.5 thus shows that, when no saturation occurs, controller output is unchanged from that of the previous Sections. What changes is, then, the anti-windup behaviour. This is strictly dependent on the choice of transfer function $\Gamma(s)$: this has to satisfy three criteria, namely

- A. $\Psi(s) = \frac{\Gamma(s) - D_C(s)}{\Gamma(s)}$ must have relative degree strictly greater than zero, *e.g.* the transfer function must be strictly proper so, at least, $\Gamma(s)$ and $D_C(s)$ must have the same higher order term.
- B. Polynomial $\Gamma(s)$ must be *Hurwitz*, *e.g.* all its roots must have negative real part.
- C. Constant term of polynomial $\Gamma(s)$ must share same sign of the constant term of polynomial $N_C(s)$, or $\frac{N_C(0)}{\Gamma(0)} > 0$.

The three conditions are, all in all, not particularly stringent, as a degree of freedom is provided by the insertion of the additional polynomial, $\Gamma(s)$. In this specific situation, project choice for the supporting polynomial is

$$\Gamma(s) = 1 + s. \quad (6.6)$$

The choice is performed with a view to respecting the three feasibility criteria, with the first and the third being immediately verified and the second featuring $\Psi(s) = \frac{\Gamma(s) - D_C(s)}{\Gamma(s)} = \frac{1}{s+1}$, whose relative degree is 1, thus being greater than 0. Anti-windup scheme is made of two transfer functions, being $\frac{N_C(s)}{\Gamma(s)}$ and $\frac{\Gamma(s) - D_C(s)}{\Gamma(s)}$; the former is placed on the feedforward

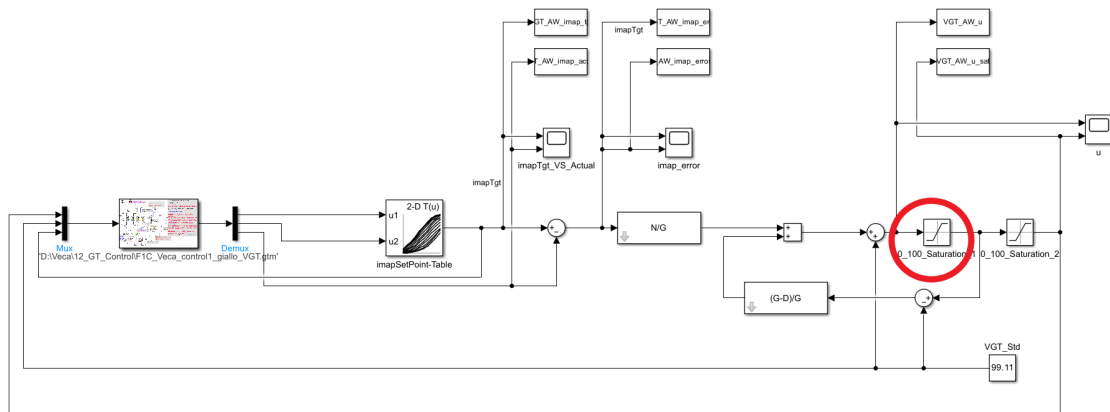


Figure 6.16: Anti-windup generalized form architecture, represented for the VGT control; $\Gamma(s) = G(s) = 1 + s$. Circled block is the actuation saturation

branch and the latter is on the feedback one, coming from the saturation block. For the sake of compliance with theoretical scheme[38], a further saturation block is included after the first one, on which the anti-windup action depends. More details are provided via SimuLink block representation, in Figure 6.16.

Control outcome is comparable to that of the conditional integrator, as it is possible to see in Figures 6.17 and 6.18.

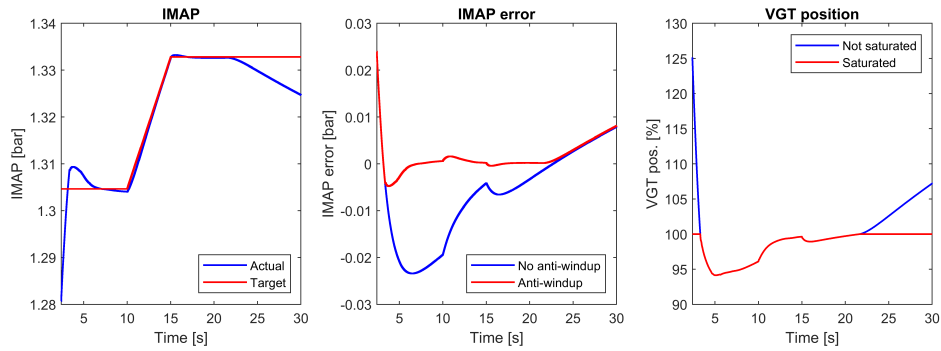


Figure 6.17: *IMAP* target vs actual value, *IMAP* error with built-in anti-windup and rack position, with general anti-windup architecture applied on VGT controller

Performance outcome is close to that of conditional integration AW logic. This is due to the similarity between the two architectures. A marginally higher overshoot is obtained at $t \pm 4$ s and is mostly due to the generality of the AW logic, whose performance exasperation is sacrificed in favour of a much wider application range.

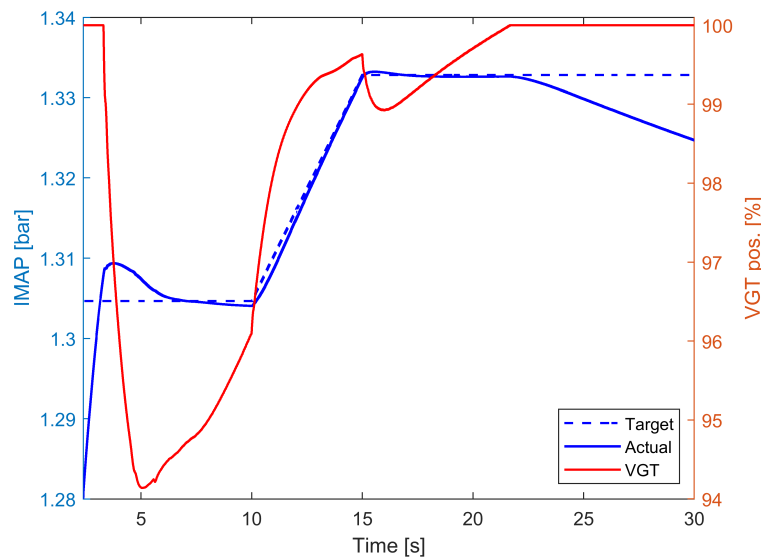


Figure 6.18: *IMAP* target vs actual value and rack position, with general anti-windup architecture applied on VGT controller

Figure 6.18 highlights also the corresponding parallelism between VGT rack position in the study case and that of conditional integration AW, visible in Figure 6.15.

6.6 Performance correlation

Once the anti-windup techniques have been presented, it is indeed crucial to understand what of them stand out as the most reliable ones. A first division line can be drawn between architectures based on boolean logics, that introduce a marked non-linearity to the system response, and those relying on transfer functions that variably modulate the integral error depending on the actuator saturation entity. On the one hand, former techniques act macroscopically on the windup phenomenon, being therefore more easily manageable than the latter; on the other, introduced non-linearities may result in poorly behaving controllers, such as the *AW baseline* or the *AW different thresholds*, endowed with zeroing activation cutoffs: in both those cases, the windup is recovered in a relatively large amount of time: 5 s *versus* the ca. 1 s needed by the AW conditional integration scheme, mounted on the very same controller. Response time-wise, a marginally worse performance is achieved by the *AW moving average architecture*, aimed at smoothing the integral error before applying any logic, so as not to induce possible chattering phenomena in the actuator. In this case, the windup phenomenon lasts ca. 1 s more than in the other boolean schemes, as a set time is needed for the averaging to take place. This additional time loss is proportional to the length of the averaging range, defined in SimuLink environment. Last example, the *AW generalized form* architecture, shows a response time window that is practically analogous to that of the *AW conditional integration* scheme. The effort spent on the design of a further transfer function, detuning the integral error, as well as the lack of a visualization immediacy in the designed architecture, do not justify the large-scale application of such a module in all the CEOPs controllers.

Performance of the five presented architectures are summarised in Figure 6.19.

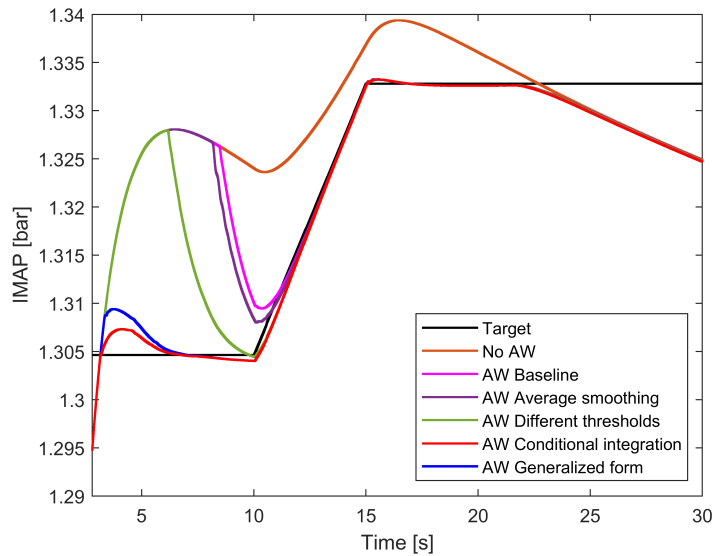


Figure 6.19: *IMAP* target *vs* actual value, without anti-windup and with the five different anti-windup architectures

Figure 6.19, depicting the different AW techniques in [2.8; 30] s time range, clearly shows

how *AW conditional integration* has an edge over the other techniques and is only comparable to the generalized form scheme that, however, yields a marginally slower settling time. The other three techniques, namely the *AW baseline* architecture, *AW average smoothing* and *AW different thresholds*, are defined by a similar logic, following the no-anti-windup defined *IMAP* and abandoning it progressively sooner depending on the quality of the activation logic. The other two techniques, as can be seen, radically change the shape of the *IMAP* actual value, bringing it much closer to the target value.

Considered literature [35][36][37][38] further studies other techniques, one of them involving a $\Gamma(s)$ transfer function of the form $\Gamma(s) = \gamma + s$, instead of classical building scheme $\Gamma(s) = 1 + s$. This enables to modulate the desaturation action, exploiting the free parameter γ . The scheme has been described for a second order control transfer function; if the order increases, that of $\Gamma(s)$ increases too.

One last proposed idea is the usage, as input of the anti-windup architecture, of the second derivative of the target error, instead of the first one itself. This may be helpful, in specific given situations, to speed up even more the exit from the control saturation zone, as the activation of the anti-windup logic would not start when the integral error starts to decrease, but already as it starts *increasing at a slower rate*. A predictive logic based on the target error behaviour could be in this case used, so as to understand when to switch, from the classical anti-windup scheme, to that involving the second derivative of the target error, as the logic may not be applied in each specific occurrence.

Key takeaway of the chapter is the different range of effectiveness of the tested anti-windup architectures. The actions are distinguished in terms of faster or slower tracking, as well as in terms of chattering phenomena in the control actuation. The higher or lower linearity of the control actuation is, in turn, a valuable indicator of the quality and feasibility of the control scheme. Conditional integration AW is the best performing amongst the set of schemes: both the EGR and the VGT actuation control systems are therefore equipped with this technical solution. Improvement in tracking efficacy can be seen in Chapter 7.

Chapter 7

Gain Scheduling Control

This chapter outlines the principles upon which a gain-scheduling control algorithm has been built and what the results of such procedure are. More specifically, a first control attempt relying only on four CEOPs is presented, followed by the complete twelve CEOPs control testing and assessment. Eventually, conclusions are drawn and a comparison between the benchmark experimental control, presented in Section 7.5, is made.

Gain scheduling is a common technique to address the control of nonlinear systems, whose dynamics change from one operating condition to another. Gain scheduling is used when a single set of controller gains does not provide desired performance and stability throughout the entire range of operating conditions that are intrinsic to the plant. [43]. Founding idea is to design more controllers, each one for an operating area of the controlled system, that is in this case the engine airpath. Each controller is designed basing on a linearisation of the mathematical model of the engine plant, that is therefore an approximation, and guarantees the meeting of the requirements only in the vicinity of the operating point. Obtained control parameters are therefore interpolated, thus varying along with the current engine airpath state.

Core aim of gain-scheduled control is to tackle the intrinsic non-linearity of the system plant with a control architecture that varies from one operating condition to another. Immediate effect of this procedure is the reduction of the working area of each controller: each $G_{C,i}$ transfer function now operates on a narrower region, with less risks of stepping out of the linearity region; maintaining the controller inside given borders does guarantee that an intensity-wise tailored control signal $u(t)$ is given to the valve actuators. No guarantee is given in terms of stability of the system: it is worth stressing that stability is a *punctual* property when dealing with linearised models that approximate a *nonlinear* system. At the end of the control design process, stability has to be assessed through tests and specific attention has to be paid when crossing from one operating point to the other.

Linearised models of the engine system have been identified and collected in Chapter 4, each model being linear in the vicinity of the EOP on which the identification has been run. To design a set of PI controllers, a semi-automatic tuning of the control parameters,

in the form of integral and proportional gains, $K_{I,i}$ and $K_{P,i}$ is applied, its scope being the selection of the most appropriate control parameters, guaranteeing consistent phase margin, crossover frequency ω_c and, consequently, overshoot, rise and settling time. The controller $G_{C,i}$ is chosen, time after time, depending on engine speed and $BMEP$ requested by the driver through the accelerator pedal.

7.1 Four CEOPs gain-scheduling

This first Section illustrates the control process when using a reduced set of four controller couples, thus four EGR and four VGT controllers; aim of this is to already provide a sufficiently general controller, that operates over a wide engine area, with only minor slips.

To accomplish the described target, four CEOPs out of the original twelve are chosen. Underlying *ratio* of the process is to guarantee that an as large as possible engine map area is covered by the chosen points, for this reason the selected CEOPs are practically arranged as the vertices of a square, within the engine operating map. Figure 7.1 points out how the CEOPs are chosen, highlighting with black filled dots the four selected CEOPs, while showing in blue the set of the twelve control points; benchmark point n. 15 is also highlighted, with red filled dot, for the sake of completeness. The same CEOPs are listed in Table 7.1, along with their respective plant models and the chosen control gains, both for EGR and VGT control, following in Tables 7.2 and 7.3. Control gains are selected according to the same procedure described in Section 5.4.

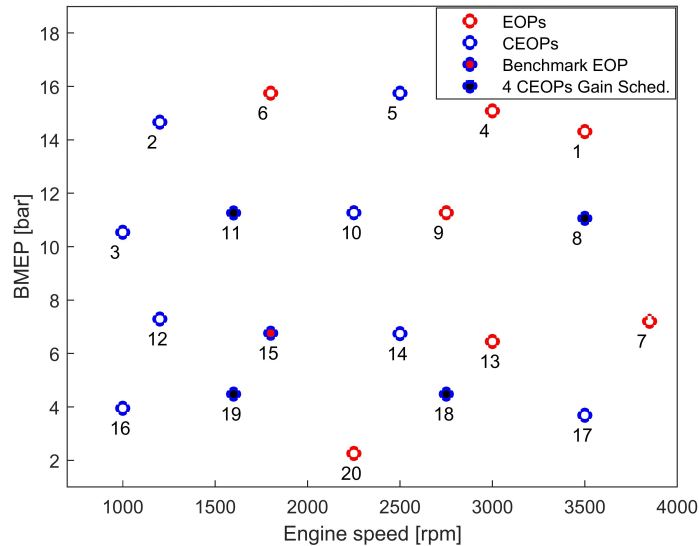


Figure 7.1: The four selected CEOPs, filled in black, chosen among the twelve CEOPs, in blue; benchmark point n. 15 is highlighted in filled red dot

The same CEOPs are also described in terms of zeros and poles of their plant transfer functions, $G_P(s)$, in Figure 7.2 for the EGR plant and in Figure 7.3 for the VGT plant.

| n. | CEOP. | Engine speed [rpm] | $BMEP$ [bar] |
|----|-------|--------------------|--------------|
| 1 | 8 | 3500 | 11.06 |
| 2 | 11 | 1600 | 11.26 |
| 3 | 18 | 2750 | 4.48 |
| 4 | 19 | 1600 | 4.48 |

Table 7.1: The four CEOPs, chosen to build the prototype gain-scheduling controller

| Point n. | Engine speed [rpm] | $BMEP$ [bar] | $G_{P,EGR}$ | $K_{I,EGR}$ |
|----------|--------------------|--------------|---|-------------|
| 8 | 3500 | 11.06 | $\frac{-45.279(s+4.502)}{(s+52.51)(s+3.786)}$ | -15 |
| 11 | 1600 | 11.26 | $\frac{-6.98(s+0.5268)}{(s+39.18)(s+0.429)}$ | -45 |
| 18 | 2750 | 4.48 | $\frac{-6.77(s+1.294)}{(s+30.47)(s+0.8469)}$ | -35 |
| 19 | 1600 | 4.48 | $\frac{-3.2056(s+0.4282)}{(s+33.34)(s+0.3116)}$ | -85 |

Table 7.2: The four CEOPs, gain-scheduling and plant transfer functions for EGR controller

It is immediate to understand that control gains K_I and K_P vary in a way that does not pay the duty to discontinuity: indeed, gains vary according to engine model, not featuring major spikes between one point and the other while, at the same time, showing peculiar characteristics in specific engine areas. Among these, the most evident is the presence of high gains in CEOP n. 19, characterised by low engine speed and low $BMEP$, thus struggling to provide right amount of air flow and boost pressure, as the engine speed is low: this is at the base, in turn, for the need for high control gains.

The described CEOPs are then exploited to build a map, with a view to obtaining a direct correspondence between any engine speed and $BMEP$ value and the targeted CEOP. The current engine speed and $BMEP$ are therefore linked to the nearest between the selected four CEOPs; this procedure will be referred to as *vicinity mapping* and has been described in Section 3.3.1. An alternative mapping is proposed, basing its correspondence not just on the two main engine variables, but also to the plant model affinity, in terms of fitting percentage, zeros, poles and gains, among the nearest engine EOP to the current engine state and the four chosen CEOPs; this mapping will be known as *affinity mapping* and is aimed at overcoming minor discrepancies that may occur, when selecting a CEOP basing only on its euclidean vicinity to the current engine state. Details on the mentioned mapping principle are given in 3.3.2. Eventually, one further mapping method is discussed, relying on k-means clustering when subdividing the engine operating areas into subregions. The mapping will be referred to as *k-means clustering mapping*, and an outline of its operating principle is given in Section 3.3.3.

A comparison between *vicinity mapping* and *affinity mapping* is shown in Figure 7.4, where nonlinear contour of *affinity mapping* are well distinguishable from those of *vicinity mapping*.

| Point n. | Engine speed [rpm] | BMEP [bar] | $G_{P,VGT}$ | $K_{I,VGT}$ | $K_{P,VGT}$ |
|----------|--------------------|------------|--|-------------|-------------|
| 8 | 3500 | 11.06 | $\frac{0.0020(s+1342)}{(s+43.03)(s+3.76)}$ | 630 | 168 |
| 11 | 1600 | 11.26 | $\frac{0.0062(s+35.61)}{(s+15.39)(s+1.206)}$ | 720 | 597 |
| 18 | 2750 | 4.48 | $\frac{0.013521(s+2.227)}{(s+3.313)(s+1.265)}$ | 650 | 514 |
| 19 | 1600 | 4.48 | $\frac{0.0037(s+8.66)}{(s+16.22)(s+0.996)}$ | 2100 | 2108 |

Table 7.3: The four CEOPs, gain-scheduling and plant transfer functions for VGT controller

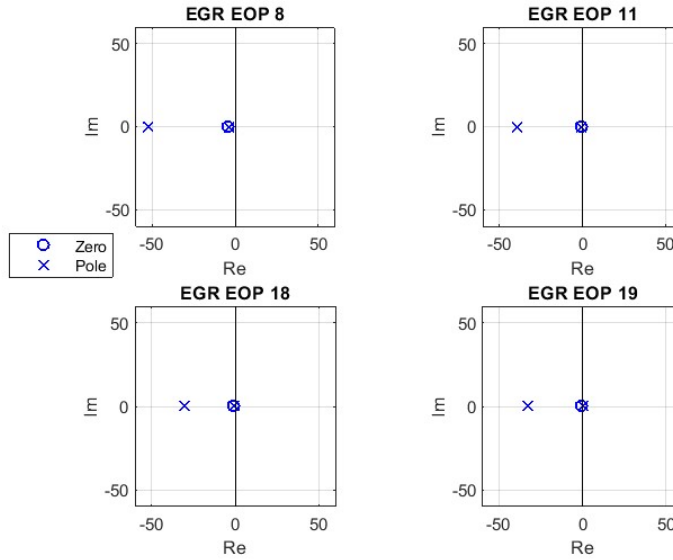


Figure 7.2: EGR zeros and poles of the four selected benchmark plants, $[0; 60]$ axes range

Going beyond the mapping principle upon which the controller gain is chosen, these data is expressed through lookup tables in SimuLink environment; controller gains are chosen according to the nearest CEOP to the current engine state, clipping to map border values if the engine state were to be outside the canonical engine map area. The switch from an operating point to the other, critical because of the discontinuities it generates in the control action, is addressed through a bumpless architecture, in order to smooth the control command. The bumpless architecture consists of moving average blocks, helping during the transition between one gain K_C and the other. Such blocks are set to average the control gains on a 2 s range, averaging the signal over 200 samples, to prevent sudden spikes in the control action. A faster change can be adopted for more aggressive test sequences. Other implementations, such as slow-fast decomposition [41] of the controllers transfer functions, as well as the usage of bumpless transfer filters [40] can be found in the literature and may be an occasion for further research. Operating principle of the latter is, in any case, similar and involves the prevention of spikes in the control action, causing undesired effects in the target tracking process.

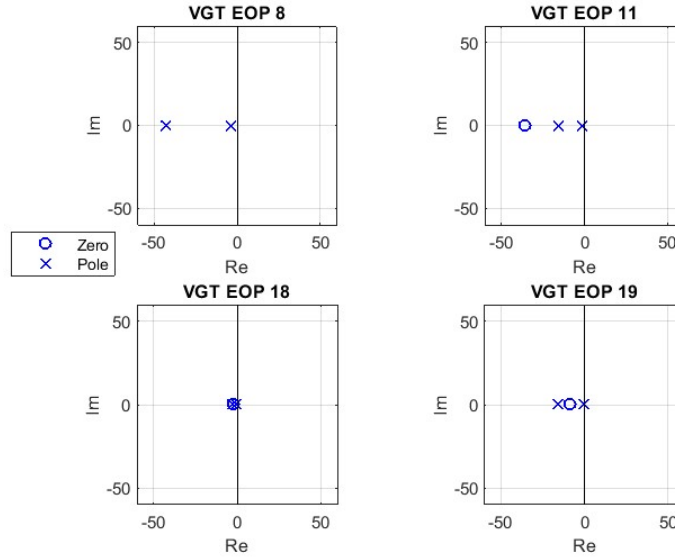


Figure 7.3: VGT zeros and poles of the four selected benchmark plants, $[0; 50]$ axes range. CEOP n. 8 features an additional high frequency zero

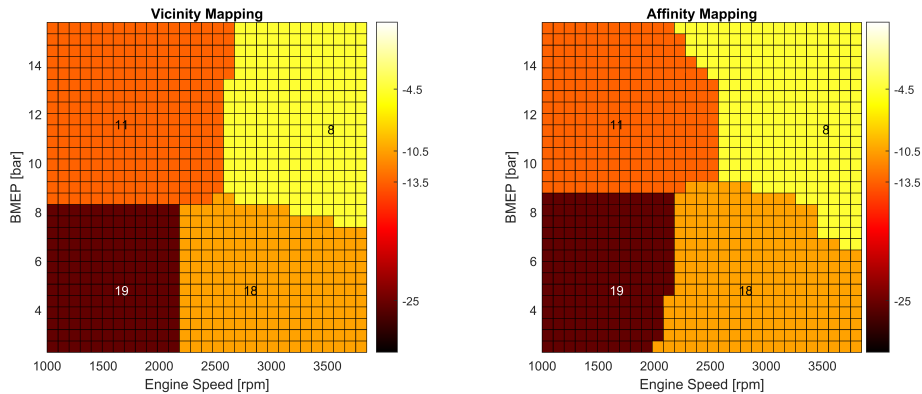


Figure 7.4: $K_{P,EGR}$ in four points mapping, *vicinity vs affinity mapping*, with labelled CEOPs numbers

SimuLink scheme of the proposed control architecture for VGT actuation is provided in Figure 7.5. Here, VGT gains have been reduced by 70% with respect to original designed values to avoid heavy actuator chattering, similarly to what has been done with EGR controller.

Figure 7.5 further offers the occasion to note the dichotomy of the designed controller: in this case, control logic is split in an upper part, providing the feedback correction and a lower one, giving the mapped preliminary VGT position value. Feedback part is marked in green and feedforward contribution is marked in red in Figure 7.5. A more articulated control scheme will be presented in Section 7.3.

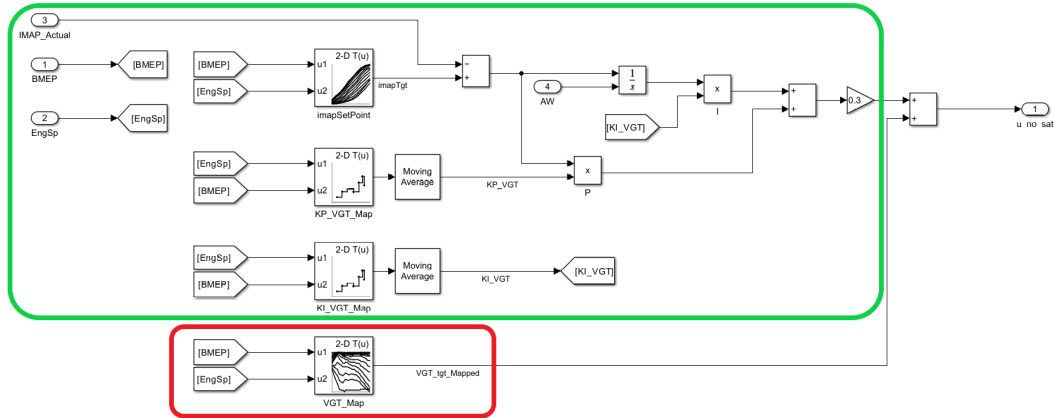


Figure 7.5: VGT PI control scheme, with four points gain-scheduling and command for integral anti-windup

A simulation performed on the aggressive test yields the following results, presented in Figure 7.6; in Figure 7.7, same results highlight how the switch from one controller to the other, taking place at this stage suddenly, does indeed show side effects on the control action, in terms of unexpected control behaviours, *e.g.* spikes. For reference, see circled area in Figure 7.6, where target tracking features a sudden oscillation after a rapid gain change. Fairly decent tracking quality can be appreciated in Figure 7.6, where a consistent air mass flow rate tracking is juxtaposed to a slightly delayed *IMAP* tracking; the small delay is a typical feature of the VGT actuation mechanism. Actuation ripple in VGT rack position owes to a still non-perfectly characterised actuation mechanism. Slow behaviour of the valve should be, indeed, taken into account through the application of a filtering, that represents the inertia of the mechanical component. Simulation is performed adopting the *standard mapping*, thus linking each current engine state with its corresponding closest CEOP, among the four used ones.

Figure 7.7 confirms the underlying procedure of gain-scheduling. A bumpless filter architecture is developed to address the issue. VGT gain-scheduling, featuring the exact same behaviour, is not shown for the sake of brevity.

Figure 7.7 underlines the behaviour of the gain-scheduling mechanism: controller starts working in the low engine speed ($< 1500 \text{ rpm}$) - low *BMEP* ($< 7.5 \text{ bar}$) region, CEOP n. 19 and gradually enters other regions, such as at $t = 22 \text{ s}$, where engine speed is raised, entering CEOP n. 11, where controller gain is consequentially diminished in absolute value. Engine cycle progressively gets more demanding and, as an example, at time $t = 34 \text{ s}$ CEOP n. 18, corresponding to high engine speed - high *BMEP* is reached. To this regard, the two described gain variations are indicated by arrows in Figure 7.7, where current CEOP is listed from time to time in black. Last CEOP variations are omitted to avoid overwhelming

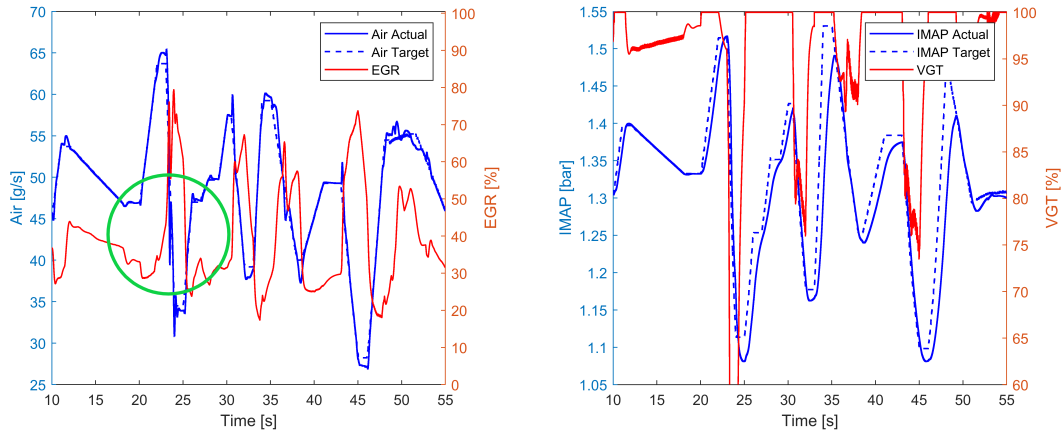


Figure 7.6: Control performance, with EGR and VGT gain-scheduled controllers, on four points vicinity mapping, on aggressive test sequence, see 5.14

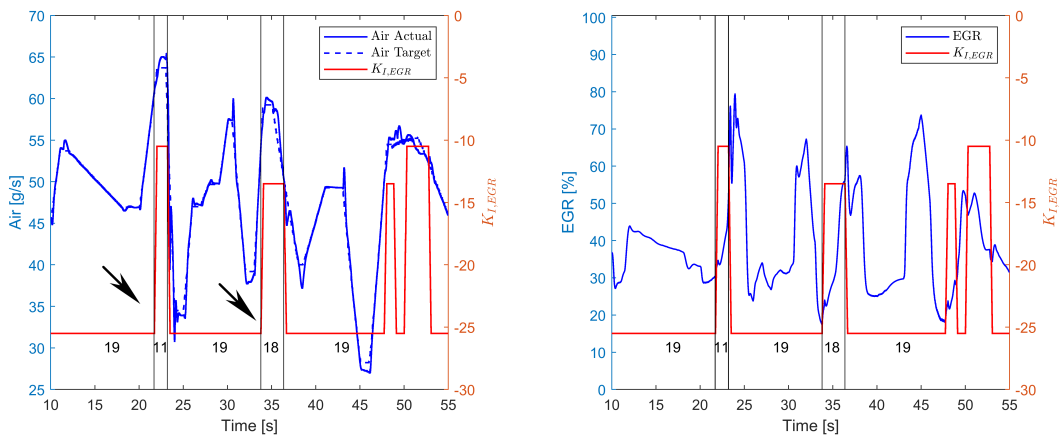


Figure 7.7: Scheduled EGR gains variation on four points vicinity mapping, in parallel with target and actual air (left) and EGR command (right), on aggressive sequence, see 5.14

the visual representation; indeed, in the last part of the transient, the controller cyclically re-visits CEOPs n. 18, 19 and 11. It is necessary to mention that, at this step, control gains are varied abruptly, hence generating spikes in the output signals and, possibly, unstable behaviours.

Same results are now proposed in Figures 7.8 and 7.9 when using *affinity mapping* to select the controllers gains, and averaging the scheduled gains change over a range of 2 s. Noticeable is the absence of spikes caused by gain changes: specifically, previously circled spike in Figure 7.7 at $t = 23.5$ s, has now disappeared.

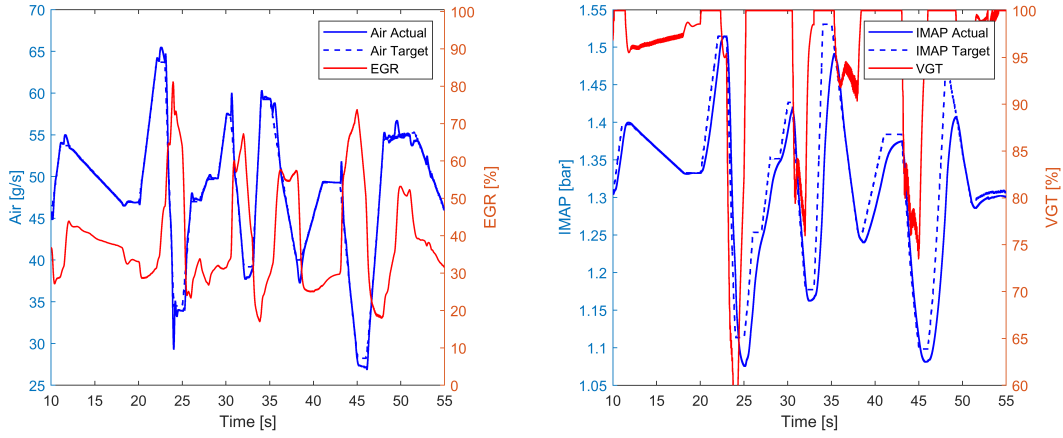


Figure 7.8: Control performance, with EGR and VGT gain-scheduled controllers, on four points affinity mapping, on aggressive test sequence, see 5.14

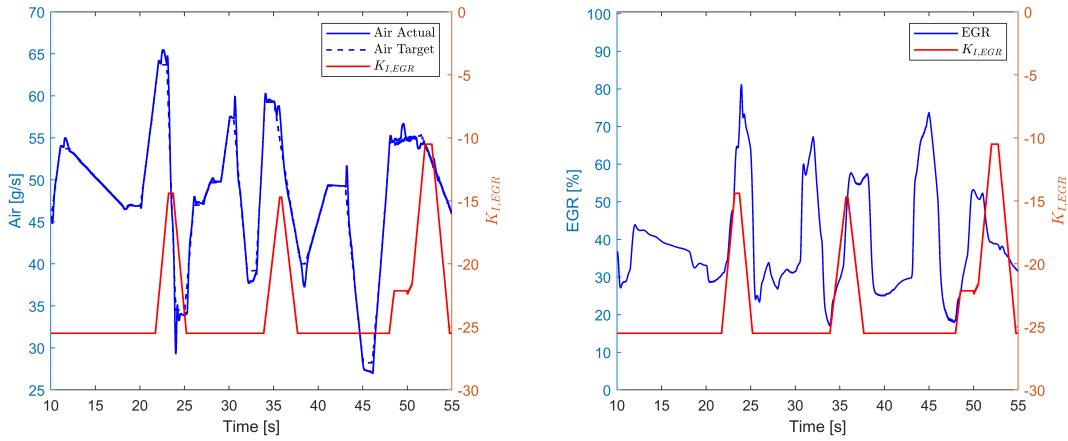


Figure 7.9: Scheduled EGR gains variation on four points affinity mapping, in parallel with target and actual air (left) and EGR command (right), on aggressive test sequence, see 5.14

7.1.1 Affinity vs vicinity mapping: performance comparison

The choice of the most adequate engine mapping to properly select gain-scheduling controller gains plays a crucial role to guarantee control performance. Even though the presented principles are here limited to target variables tracking in aggressive test sequence, results already shed light on the overall benefits of using one method instead of the other. A comparison, in terms of air mass flow rate tracking performance, is now given between benchmark CEOP n. 15 control, *vicinity* four points control and *affinity mapping* four points control. Results can be seen in Figure 7.10; an enlargement on a ramp sequence is given in Figure 7.11.

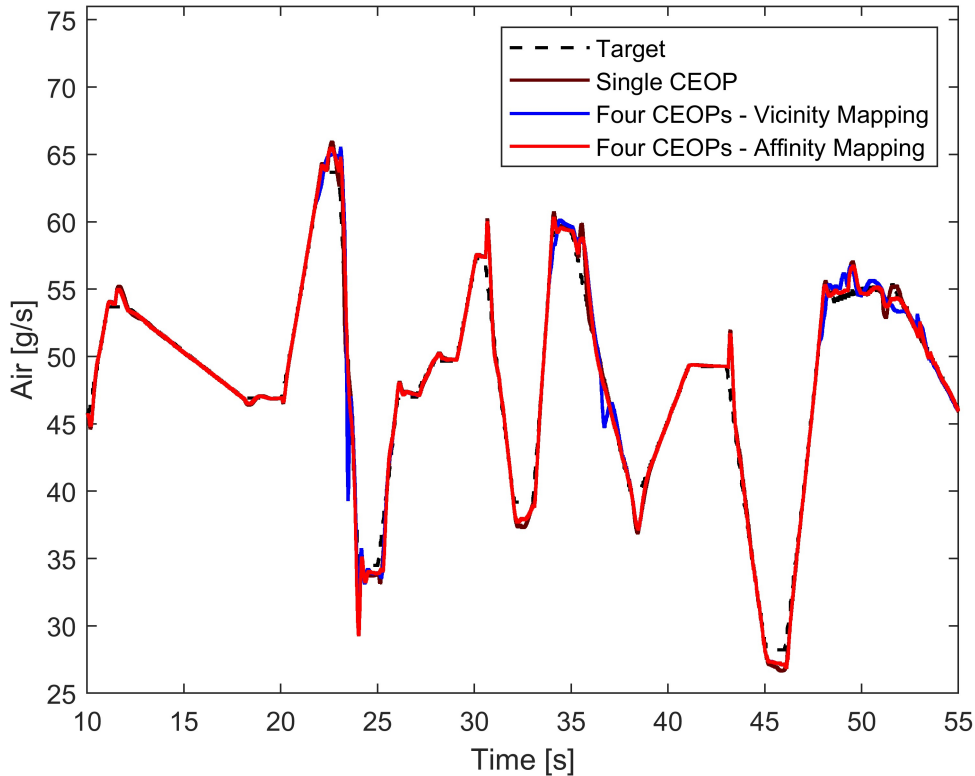


Figure 7.10: Tracking performance on EGR valve; target air flow is compared to benchmark control on EOP n. 15 and to four CEOPs controller, with *standard* and *affinity* mapping, on aggressive test sequence, see 5.14

The tracking performance reveals positive sides, however still leaving room for improvement. First noticeable point is that *affinity mapping* brings improved performance over its counterparts, suggesting that a rapid switch to the most representative control model is key to attain a better signal tracking; this is noticeable not just in terms of overshoots, but also considering the absence of spikes, such as at time $t = 24$ s or $t = 38$ s in the *affinity mapping* control compared to the *vicinity mapping* one, due to a time-shifted transition from a CEOP to the other, that enables, from a theoretical point of view, the most fitting controller model to be applied for a wider engine map span. This thesis is further justified by the identical behaviour that *vicinity* and *affinity mapping* show in the first time instants of the test sequence, when the effect of a timely switch does not play any role, not having changed gain yet. However promising, a thorough validation of this comparison has to be carried on, considering, *e.g.*, more than four controllers transitions, or both switch directions from one CEOP to the other.

In addition to that, four points controllers, either with *vicinity* or *affinity mapping*, are less prone to unexpected spikes, that may be caused by both the destructive interaction between EGR and VGT commands, from which non-linearities may originate, as well as

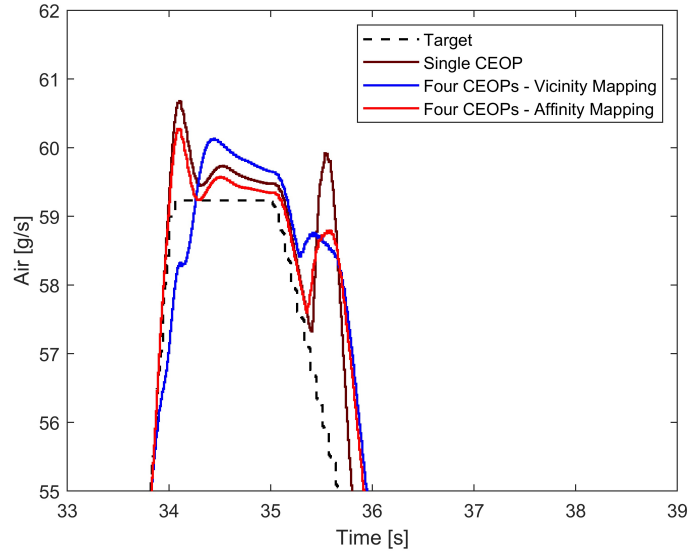


Figure 7.11: Enlargement - Tracking performance on EGR valve; target air flow *vs* benchmark control on EOP n.15 *vs* four CEOPs controller, *standard* and *affinity* mapping, on aggressive test sequence, see 5.14

the non-perfect adequacy of the reference signal, being largely affected by chattering, this being a path for supplemental research on the topic.

A third and last point to bring on is the presence of undershoots, mostly when deviating from the engine speed - *BMEP* range on which the controllers are tailored. This is once more an expected outcome of the interaction between the two valves, having at times contrasting tasks and therefore causing such behaviours. The presence of such spikes, partially attributable to non-minimum phase behaviours, is further validated from the presence of EGR identified models featuring positive zeros, that induce such an outcome.

To overcome the difficulties connected to this last point, a filter on the VGT actuation signal is performed. The filtering transfer function is chosen among a set of the form $\frac{a_0}{b_0+s}$, where a_0 is set to 1 and b_0 is manually tuned so as to set the passband frequency of the designed lowpass filter. Filter, at this stage, significantly reduces the participation range of the actuator. This is intentionally done so as to macroscopically feel the effect of a much milder VGT control action. Ensuring for the moment that the EGR tracking is fully achieved is specifically important, as the VGT action is, because of physical and safety limitations, constrained not to attain the same performance quality of the other valve. An advantageous side effect is the possibility to retrieve valuable and clearer information on the performance of different engine mappings. Eventually, the transfer function in Equation 7.1 has been used.

$$F(s) = \frac{1}{20s + 1} \quad (7.1)$$

Figures 7.12 and 7.13 show tracking performance of the post-filtering scheme, applied

to the *affinity mapping* four CEOPs. As it is noticeable, the isolated air flow undershoots disappear, to the detriment of the VGT speed of response. No major changes in terms of overshoots or tracking performance in general occur.

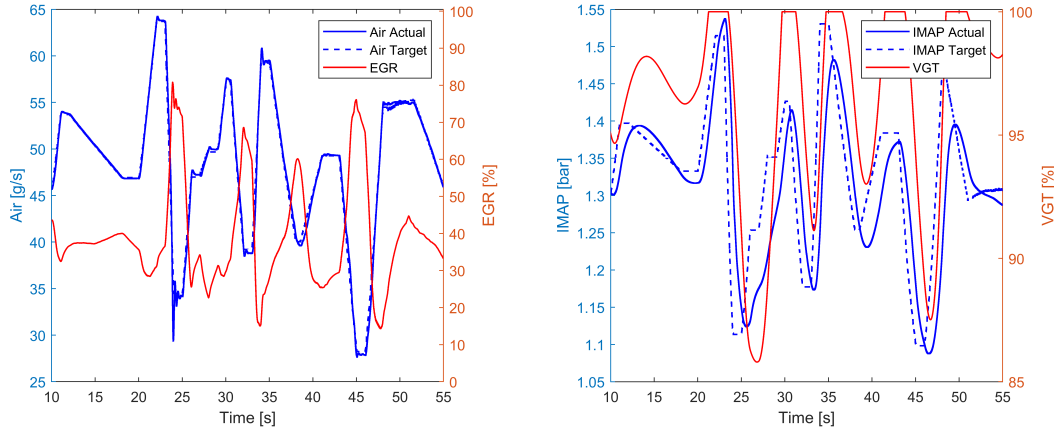


Figure 7.12: Control performance, with EGR and VGT gain-scheduled controllers, on four points affinity mapping, VGT command is post-filtered, on aggressive test sequence, see 5.14

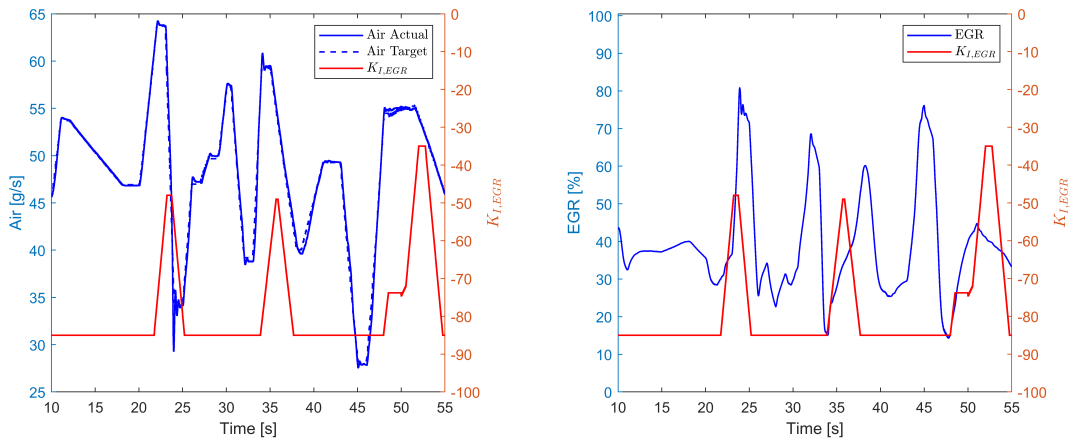


Figure 7.13: Scheduled EGR gains variation on four points affinity mapping, VGT command is filtered, in parallel with target and actual air (left) and EGR command (right), on aggressive test sequence, see 5.14

One last set of Figures, 7.14 and 7.15, aim at comparing the performance of the filtered VGT controller to the ones not adopting this latter block, testifying the smoother and more reliable tracking on the EGR side, at the partial damage of slowing down the *IMAP* boost pressure tracking.

Especially from Figure 7.15, the improved smoothness provided by the filtering of VGT control action, in accord with the physical limitations of the rack, is visible. No bump can

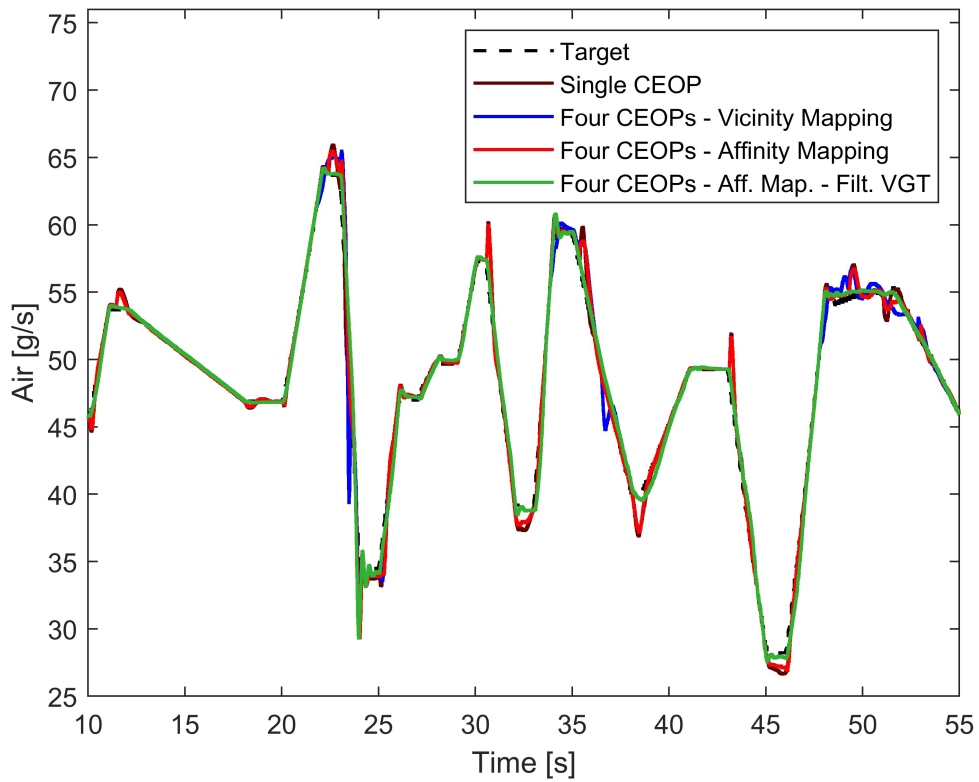


Figure 7.14: Tracking performance on EGR valve; target air flow is compared to benchmark control on EOP n. 15 and to four CEOPs controller, with *standard* and *affinity* mapping and VGT post-filtering on *affinity* mapping, on aggressive test sequence, see 5.14

be seen at $t = 35.4$ s, as VGT action is modulated over a longer time range. Overshoot is practically unchanged and, most importantly, settling to the tracked value once the ramp signal ends is better than in previous cases, though presenting a small ripple.

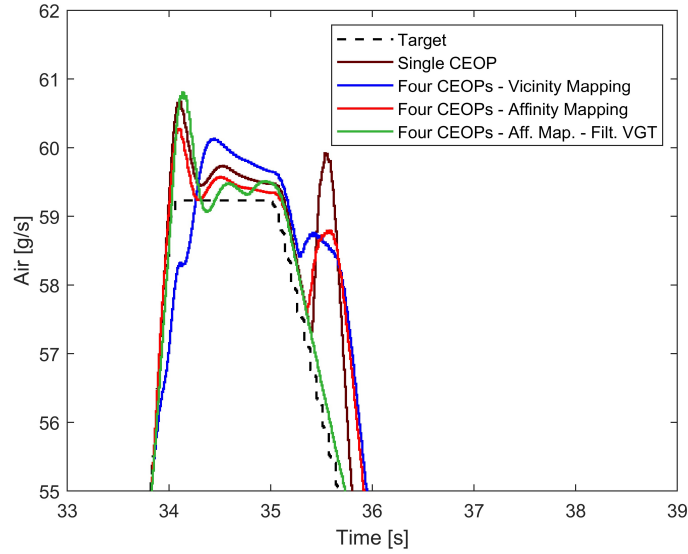


Figure 7.15: Enlargement - Tracking performance on EGR valve; target air flow *vs* benchmark control on EOP n. 15 *vs* four CEOPs controller, *standard* and *affinity* mapping and VGT post-filtering on *affinity* mapping, on aggressive test sequence, see 5.14

7.2 Whole engine map gain-scheduling

In this section, final control outcome of the actuators is presented. The control takes now place over twelve different CEOPs, variably displaced across the engine map. Integration of injected fuel quantity into the control action takes place so as to improve control performance and speed of response.

Adopted controllers are of *PI* form for all the VGT controllers; conversely, out of the twelve EGR CEOPs, proportional term is less used: nine CEOPs have a relatively small baseline $K_{P,EGR} = -1.5$ and two of them require a slightly larger *P* contribution, to achieve better performance. EGR CEOP n. 16 deserves a separate mention, due to the peculiar physical state of its engine area. Indeed, in point 16, featuring low engine speed as well as low *BMEP* (1800 *rpm*, 3.95 *bar*), actuators have limited influence over the air flow due to its slow velocity.

For this reason, a conventionally designed controller based on the case n. 16 identified model does not yield satisfying results when assessed on the simulated plant in GT-Suite environment. The controller, built on a non-minimum phase behaviour model of the form in Equation 7.2 is therefore unreliable.

$$G_{P,EGR} = \frac{-0.32993(s - 0.638)}{(s + 10.96)(s + 0.5036)} \quad (7.2)$$

Compensator design of identified model n. 16 is not parallel to that of the other ones: more specifically, the design has been founded on different assumptions with respect to the

others. Design has been directly based on the empirical response of the GT-Power plant, in order to avoid the high sensitivity implied by a non-minimum phase project. Reasons for the design misalignment are found in the highly delayed target tracking as well as in the afore-mentioned non-minimum phase behaviour, that are both typical of low engine speed ($< 1500 \text{ rpm}$), low $BMEP$ ($< 5 \text{ bar}$) engine area.

Such situation occurs only in this very specific engine area, since low engine speed and load imply a small pressure delta between upstream exhaust pipes and downstream intake manifold. Pressure delta is therefore almost zeroed, resulting in a low air mass flow rate. Final control transfer function, based on the GT-Power simulated engine true dynamics and on the knowledge gained on previous controllers, entails an integral term of the form $-\frac{5}{s}$ and a lead network, with $z_d = 0.5$ and $m_d = 2.5$. Controller is shown in Equation 7.3. Sign of the integral gain multiplier, $K_{I,EGR}$, has been set negative as in the remaining CEOPs, for stability reasons.

$$G_{C,EGR} = \frac{-5(1 + \frac{s}{0.5})}{s(1 + \frac{s}{2.5 \cdot 0.5})} \quad (7.3)$$

Adopted gains maps are finally shown in Figures 7.16 and 7.17, respectively for EGR and VGT compensators. EGR case 16 gains are set to zero, for the sake of simplicity, having this case a tailored, separated control logic.

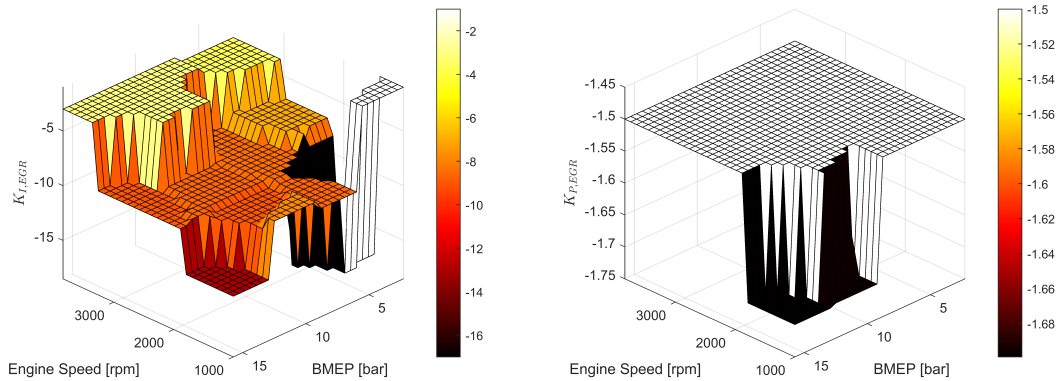


Figure 7.16: $K_{I,EGR}$ and $K_{P,EGR}$ gain-scheduling maps, through *affinity* mapping

It is worth to mention that, in Figure 7.16, showing EGR gains mapping, point n. 12 features a high integral gain. This is due, again, to the low engine speed characterising this engine state. This, in turn, requires either a high gain, when possible, to attain an adequate control action, or the slowing down of the tracking response, as preferred on case 16.

Proposed test sequences are, in this last Section, the aggressive sequence and the pedal-given sequence, already seen in Figure 5.14, to which other two, more demanding, engine cycles are added. The four sequences are here listed and reported in Figure 7.18.

The four fed test sequences are catalogued as here described.

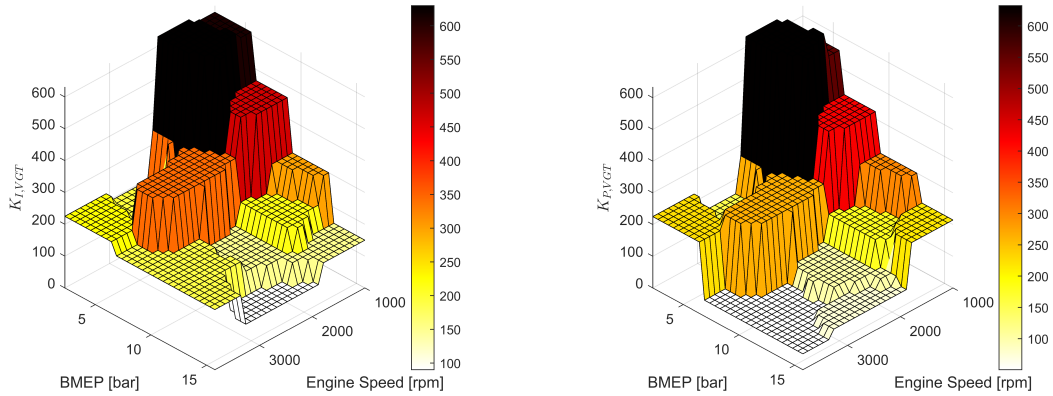


Figure 7.17: $K_{I,VGT}$, to the left, and $K_{P,VGT}$, to the right, gain-scheduling maps, through *affinity* mapping

- Aggressive test sequence: $BMEP$ and engine speed vary contemporarily, ramps are more aggressive, values do not get far from linearity range of EOP n. 15. Sequence is 55 s long.
- Pedal-driven test sequence: sequence is given directly acting on accelerator pedal and is affected from noise, already simulating a realistic input signal. Sequence length is 402 s
- Actuators limits test sequence: it tests the physical limits of the actuators by feeding them with variable slope and height ramps, along the full engine map; it is 1200 s long.
- WHTC (World Harmonized Transient Cycle) test sequence [45]; WHTC test is a transient engine dynamometer schedule, defined by the Global Technical Regulation (GTR) No. 4, developed by the UNECE GRPE group [46][47]. The sequence reaches 1863 s, thus over thirty minutes and is used for vehicle homologation purposes. Required engine speed and load are directly derived from pedal position and vehicle speed of a real driving cycle.

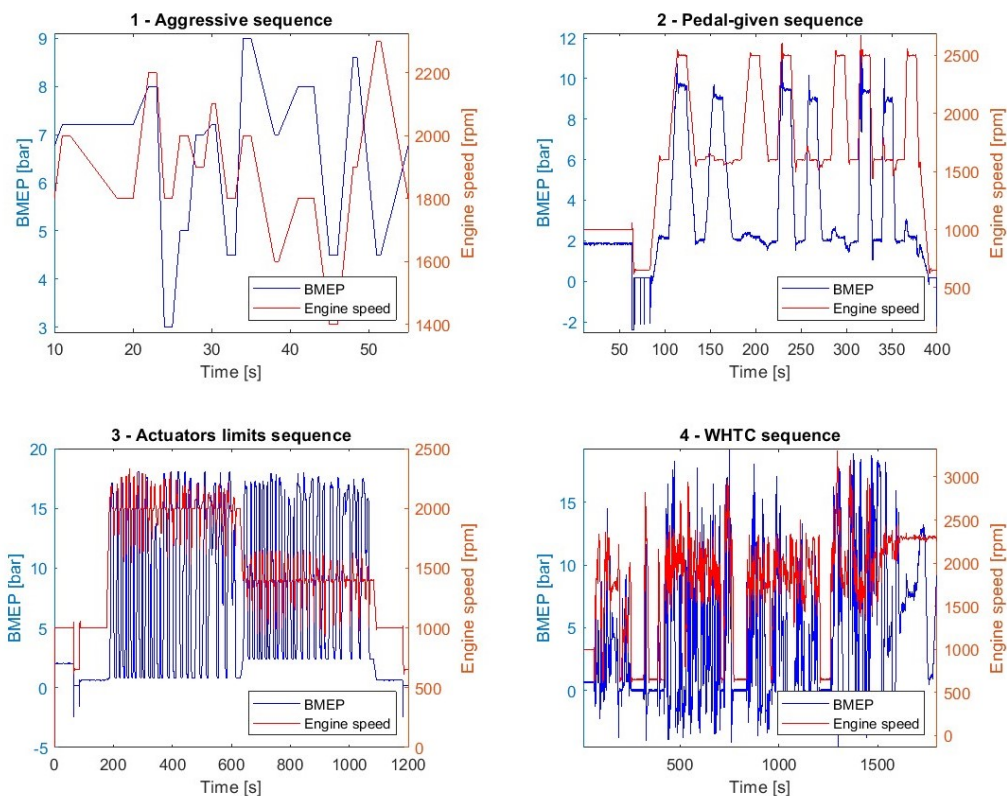


Figure 7.18: Assessment test sequences: from left to right and from top to bottom, in order, aggressive test sequence, moderate pedal-given engine cycle, actuator limits pedal-given engine cycle and WHTC engine cycle

In Figure 7.18, aggressive test sequence is presented. The sequence is only used in four-points gain-scheduling phase, to compare performances of *vicinity* and *affinity mapping* in a controlled environment, where no significant or extreme variables fluctuations occur.

7.3 Preliminary testing

A first series of results is given, adopting WHTC testing sequence, to highlight limitations that the control has when facing more demanding transients. This testing is essential to correctly assess the limits of the compensator, so as to design a tailored, definitive control logic, that can satisfy the set requirements in realistic engine usage scenarios. Figures 7.19 and 7.20 show the target tracking performance of air mass flow rate and boost pressure and corresponding actuators positions, compared to benchmark ones, set by the ECU on experimental test-bank engine testing.

Tracking performance, assessed using WHTC, that totally lasts 1863 s, is split in four smaller time spans, being

- from 125 to 150 s;
- from 645 to 675 s;
- from 840 to 920 s;
- from 1620 to 1760 s.

First and second transients present an enlargement of tracking performance over smaller time horizons; third one is characterised by frequent spikes; eventually, last transient is milder and corresponds to cycle end.

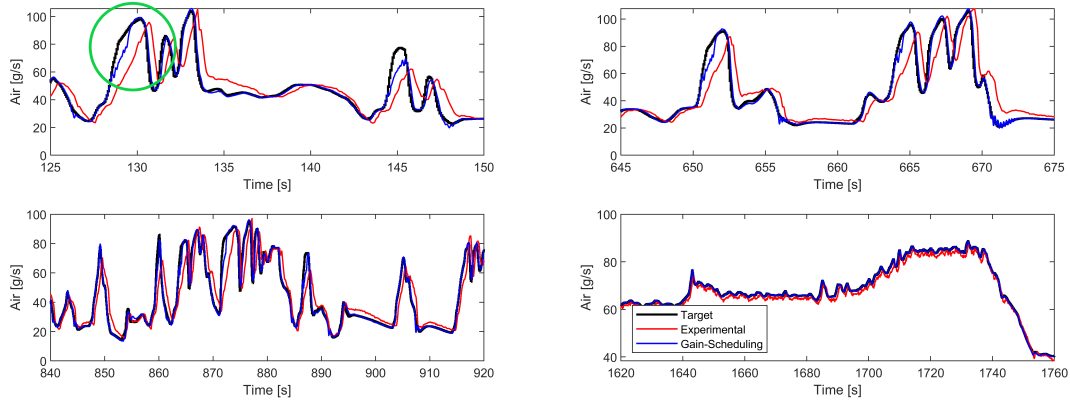


Figure 7.19: Air mass flow rate tracking performance, with EGR and VGT gain-scheduled controllers, on whole map affinity mapping, VGT command is post-filtered, on WHTC test sequence, see 7.18 for reference

From Figure 7.19, still a non-perfect matching between target value and controlled variable emerges. This is particularly visible at $t = 128$ s (circled in Figure 7.19), where even though tracking is much better than benchmark milder action, still peak air mass flow rate is not perfectly reached. A significant delay is, additionally, present in boost pressure tracking in Figure 7.20.

Figure 7.21 and 7.22 outline the behaviour of the two actuators when controlled by the gain-scheduling controller, opposed to the same values coming from benchmark ECU control.

Figure 7.21 shows a comprehensively adequate behaviour of EGR valve. Interestingly, control action does not reach saturation, opposedly to experimental benchmark control. Reaching lower valve opening values is key to correctly track air target. Occasional actuator chattering is visible, especially in two regions: one of them, circled in green, corresponds to actuator settling to a given position. The ripple is fairly low ($\sim 10\%$) and can be further lowered applying a low-pass filter to the EGR action, to better simulate its physical behaviour. A second oscillatory effect, circled in red, is present at very low EGR opening

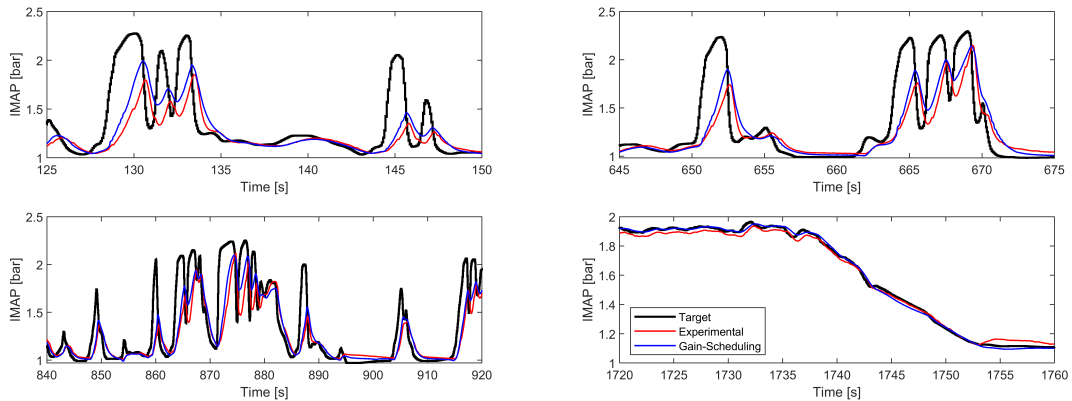


Figure 7.20: Boost pressure tracking performance, with EGR and VGT gain-scheduled controllers, on whole map affinity mapping, VGT command is post-filtered, on WHTC test sequence, see 7.18 for reference

values and corresponds to tracking of demanding air mass flow rate ramps. This essentially owes to both a non-filtered target signal and to the specifically required actuator position, that is close to lower saturation.

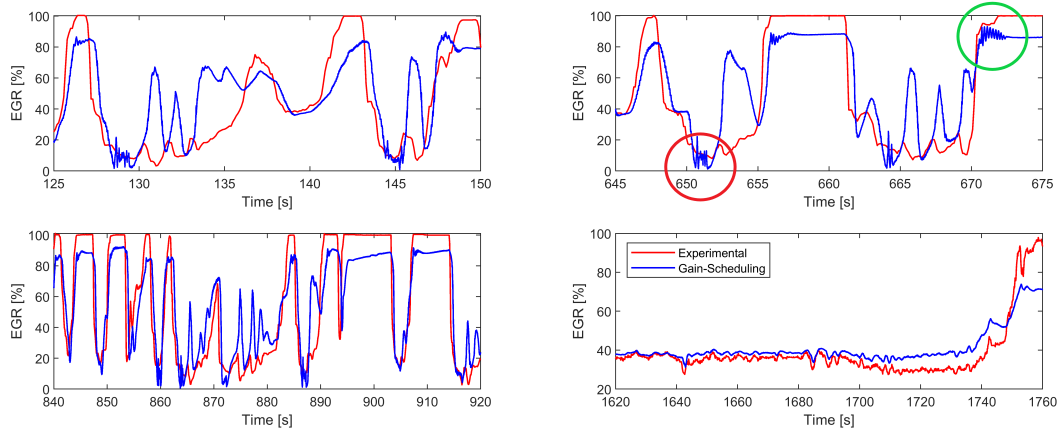


Figure 7.21: EGR valve position command with EGR and VGT gain-scheduled controllers, on whole map affinity mapping, VGT command is filtered, on WHTC test sequence, see 7.18 for reference

The overview of VGT control action is shown in Figure 7.22: here, the contribution of the VGT valve is almost absent due to actuation filtering: the pass-band is indeed low and this only leaves room for brief detachments from saturation region, as in bottom-right graph. Behaviour of the valve is largely improved thanks to the adoption of a less restrictive filter, in Section 7.4.

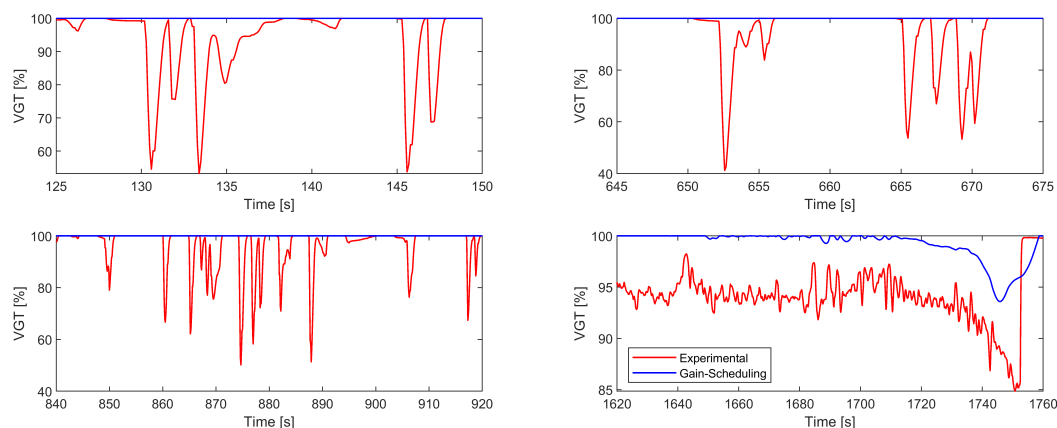


Figure 7.22: VGT rack position command, with EGR and VGT gain-scheduled controllers, on whole map affinity mapping, VGT command is filtered, on WHTC test sequence, see 7.18 for reference

7.4 Fuel injected quantity correction and filters refinement

The evaluation of target *vs* actual value graphs, in each of the four cycles, has revealed a small delay, ca. 0.1 s, when tracking target variable. Such delay is expected to increase when building an actual ECU control, due to physical and electronic limitations of the system. The insertion of refinements that can prevent an excessively long delay in the tracking action is therefore deemed as essential, thus fuel injected quantity in the cylinders is considered, as an additional control variable.

Derivative of fuel injected quantity is consequentially inserted in the control scheme and multiplied by a constant gain. This term is given as a correction to the controller output, the procedure being common in several engine airpath controllers. Scheme of the following is given in Figure 7.23.

Control action now entails three different components:

- A. Mapped control, depending on engine speed and load;
- B. Injected fuel derivative correction;
- C. Gain-scheduling PI controller.

Control branches are labelled in Figure 7.23, showing full EGR adopted control architecture. In the same picture, also case 16 dedicated control logic is highlighted, with letter *D*. For control purposes, the filtering of VGT control action is revised and moved to higher band-pass frequencies, to promote participation of the VGT rack position within the overall control action. Filtering yields a however slow control action, to account for the well-known actuation limitations. Eventual designed filter is presented in Equation 7.4 and achieves the targeted scope. VGT control gain has been eventually reduced to 30% of the initial one, as presented in Section 7.1, having seen how the effect of a milder VGT gain has

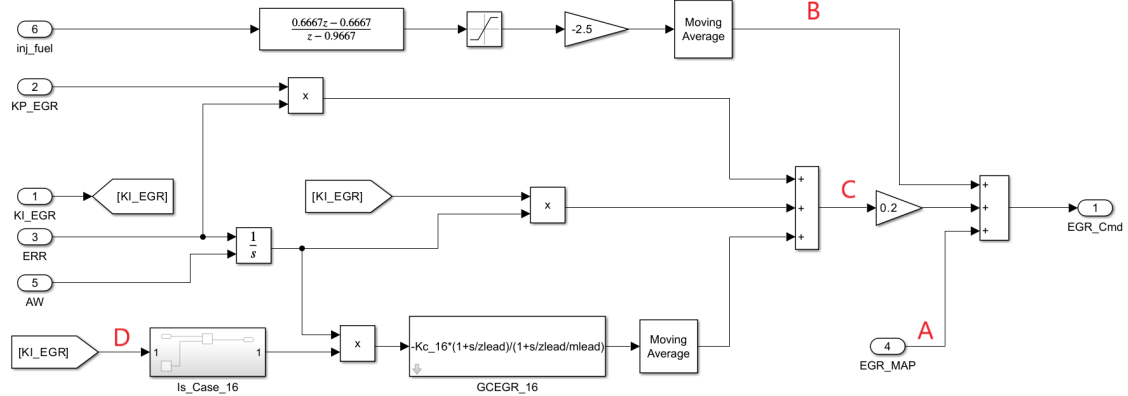


Figure 7.23: Derivative of fuel injected quantity, marked by letter B , is used as a correcting term in EGR control action

a positive influence on the two actuations coupling. The gains are anyway an order of magnitude higher than the EGR ones, thus being physically realistic.

$$F(s) = \frac{1}{2.5s + 1} \quad (7.4)$$

Used gain for the derivative of the injected fuel quantity is $K_{f.inj} = -2.5$ and derivative is performed in the discrete domain; equation is given in 7.5. Gain is negative owing to physical reasons: a positive gain would mean an opposite contribution to the control action and a consequential slowing down of the former. Numerical gain value is a compromise between obtaining a noticeable control performance enhancement and avoiding chattering risks caused by an excessive contribution of the derivative of the injected fuel quantity. Derivative is, indeed, characterised by frequent spikes. Additionally, the pole is added to guarantee the physical feasibility of the filtering action as well as to close the pass-band beyond $f_c \sim 0.6 \text{ Hz}$, where f_c is the cut-off frequency. This in turn avoids the derivation of the higher frequency components of the signal, that are mainly caused by noise corruption.

$$F(z) = 0.6667 \frac{z - 1}{z - 0.9667} \quad (7.5)$$

Altogether, derivative quantity helps reaching the correct control command faster, as it enriches the information already given by the mapped actuation value. Base command to which the PI controller further adds a corrective term is much more consistent with the desired target tracking; in addition to that, PI controller intervention is this way milder, minimising the risk of any possible instability or controller misbehaviour. Comparison between current control logic and previous one, not adopting fuel injected quantity derivative branch is given in Figure 7.24: the better tracking of ramps, such as that at $t = 128 \text{ s}$, is given by the contribution of the derivative of injected fuel quantity.

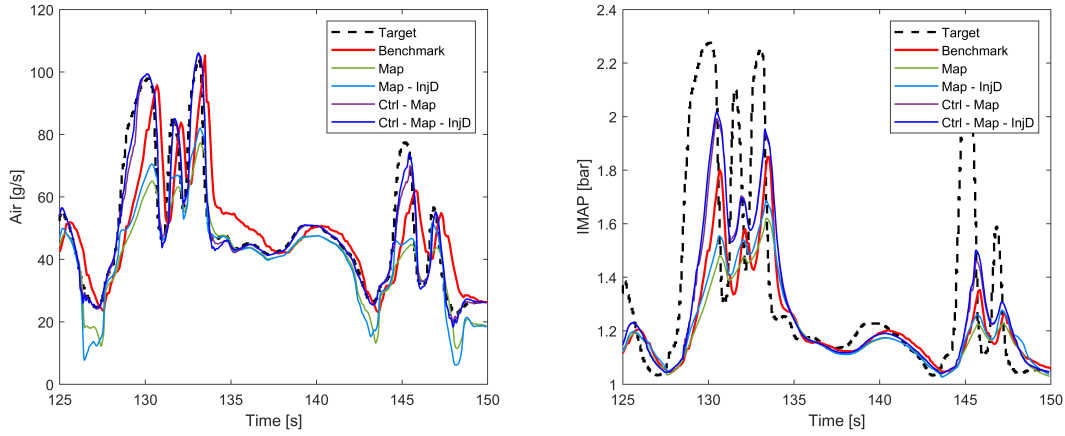


Figure 7.24: Comparison between control architectures equipped with A, A-B, A-C and A-B-C; A, B, C standing for mapped control, injected fuel derivative contribution and PI controller, respectively. Target air and $IMAP$ values are highlighted with dotted line and ECU experimental values are marked in red

From Figure 7.24 it is possible to notice how the derivative contribution of the injected fuel quantity strongly enhances the tracking speed, anticipating the control action. The derivative may introduce spikes, due to its high variability, however this has been prevented through the addition of a moving average low pass filter, weighing together 120 samples, to avoid such occurrence and a further ± 10 saturation block has been set on the derivative output. Scheme of the architecture has been introduced in Figure 7.23. An enlargement of Figure 7.24 is now given in Figure 7.25, with a view to more specifically comparing the control architecture when adopting the derivative of injected fuel or not. Scaling up is given in timespan $t = [128; 131]$ s. Figure 7.25 further highlights how the tracking performance is relatively poor when not adding the controller, as it substantially is a feedforward action only. On the contrary, gain-scheduling compensator is able to faster track the target signal and the derivative contribution emphasizes the response speed even more, gaining further decimals of second with respect to control action not equipped with the derivative of injected fuel quantity. Improvement of response time is achieved when derivative is non-null. It is thus, for the sake of completeness, noteworthy to consider that derivative contribution takes place only when *varying* the fuel injected quantity. The former is the reason why this action has noticeable effects on big ramps, such as that at $t = 128$ s in Figure 7.24. The same contribution is much lighter in slow-varying engine cycles.

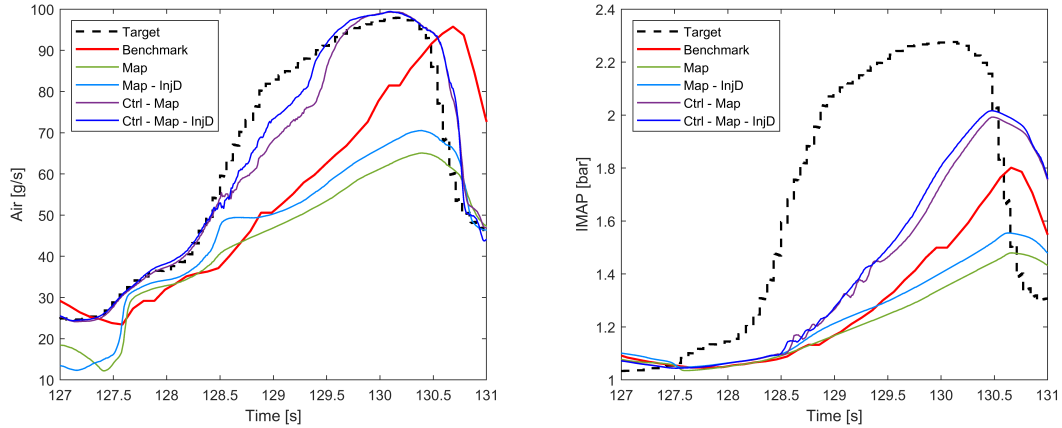


Figure 7.25: Enlargement: comparison between control architectures equipped with A, A-B, A-C and A-B-C; A, B, C standing for mapped control, injected fuel derivative contribution and PI controller, respectively. Target air and *IMAP* values are highlighted with dotted line and ECU experimental values are marked in red

7.4.1 Tracking - Pedal-given test sequence

Tests performed on pedal-given test sequence are listed in Figure 7.26, showing tracking performance of air mass flow rate and boost pressure, and 7.27, featuring EGR and VGT control actions.

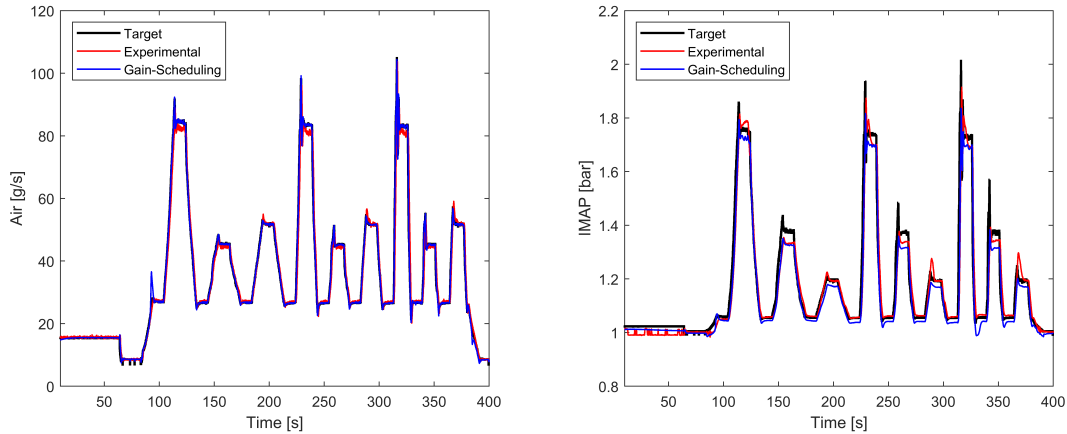


Figure 7.26: Air tracking performance, to the left, followed by *IMAP* tracking, to the right. Gain-scheduling controllers are based on whole map affinity mapping and performance is assessed on pedal-given test sequence, for $t = 10 - 400$ s, see 7.18 for reference

Left graph of Figure 7.26 shows a distinction between experimental ECU tracking performance and simulated one through gain-scheduling controller. Tracking performance is more consistent in gain-scheduling case, thanks to the adaptivity of the controller. Gains

are effectively changed when switching from one CEOP to the other and tracking is achieved throughout the engine cycle. The spike occurring at time $t = 94$ s in air tracking is due to the switch between control logic of CEOP n. 16 and that of the other map points: this irregularity owes to the later insertion of dedicated control logic characterising low engine speed - low load (< 1500 rpm), (< 7.5 bar). The issue can be easily solved modulating the entrance/exit into this specific engine area by progressively varying the involved control gains and changing the structure of the compensator, as with the other CEOPs. A last remark on air tracking takes place in terms of tracking maintenance: visibly, higher tracked air flow rate peaks are correctly reached by both experimental and gain-scheduling control, however the latter is able to stick to the required value for the needed time. Experimental control, conversely, tends to face a slight performance decay, progressively getting further from the target. This same situation does not occur with smaller peaks.

Boost pressure (*IMAP*) tracking is essentially similar to that of experimental benchmark, however the delay being largely reduced. Tracking is in gain-scheduling case more regular and overshoots are reduced. Initial drive-cycle instants show how control logic has the upper hand on that of ECU, being both closer to target boost pressure and much more regular.

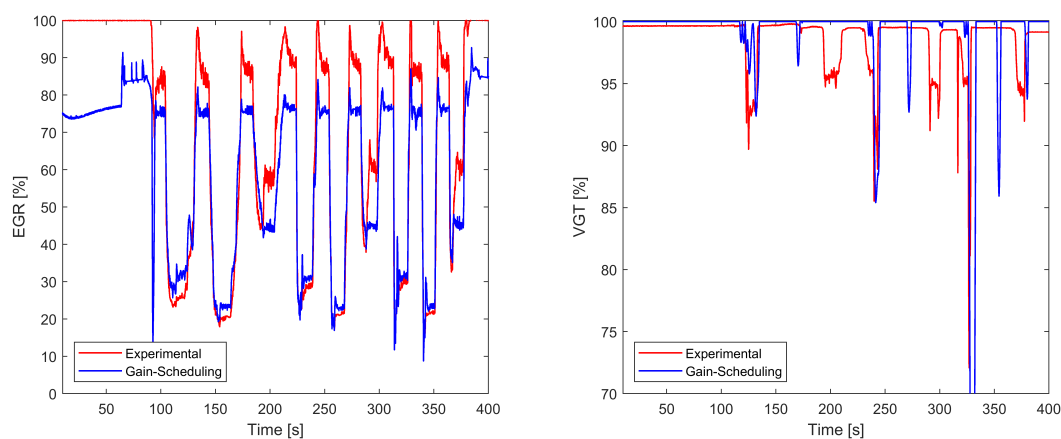


Figure 7.27: EGR control action, to the left, followed by VGT one, to the right. Gain-scheduling controllers are based on whole map affinity mapping and performance is assessed on pedal-given test sequence, for $t = 10 - 400$ s, see 7.18 for reference

Figure 7.27 offers the chance to notice the different intensity of the two control actions: that of the experimental ECU control and that of the gain-scheduling controller. Control action provided by ECU is almost always stronger than its counterpart, the cause for this being mostly the difference between the designs of the two compensators. EGR action, additionally, features overall more marked oscillations: this is imputable to higher control gains or to a moderately worse filtering action on signal noise in benchmark ECU control. It must be further noticed that VGT actuation is almost never below 70%, similarly to what happens in ECU benchmark control.

7.4.2 Tracking - Actuators limits test sequence

This drive-cycle is specifically designed to test the ability of the actuators to track fast-varying references and can be consulted in Figure 7.18. The cycle is built basing on two different areas, one featuring an average engine speed of 2000 *rpm* and an average *BMEP* of 9 *bar*, the other 1400 *rpm* and 10 *bar*. Engine speeds vary on a 600 *rpm* range and *BMEP* values oscillate on an 18 *bar* window.

Test sequence control outcomes are shown in Figures 7.28 and 7.29.

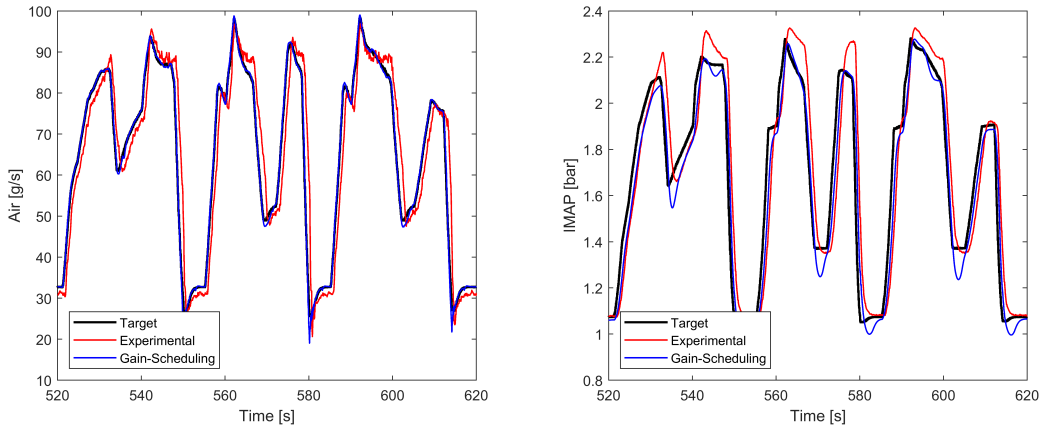


Figure 7.28: Air tracking performance, to the left, followed by *IMAP* tracking, to the right. Gain-scheduling controllers are based on whole map affinity mapping and performance is assessed on actuators limits test sequence, for $t = 520 - 620$ s, see 7.18 for reference

Figure 7.28 outlines a generally good quality of air mass flow rate tracking, that is almost always superimposed with target value. Experimental sequence, the other way round, shows a constant delay of ca. 0.5 s. Moreover, air control action does not feature sudden spikes or similar irregularities. The counterpart, boost pressure tracking, that can be seen to the right of Figure 7.28, is characterised by the presence of undershoots in the gain-scheduling control action. Undershoots reach a maximum of -16% at $t \sim 605$ s. The corresponding right graph in Figure 7.29 shows indeed that overshoots are caused by the repentine actuation of the VGT rack. This is consequential to the increase of the pass-band of the low pass filter that is placed at the controller output. Opposedly to this, overshoots are almost absent: the given details reveal that VGT control gains tuning, however consistent, may still leave room for small improvements, that can further improve tracking performance.

A focus on Figure 7.29 reveals EGR control action is milder using PI gain-scheduling controller and fluctuations in the control do indeed improve overall tracking performance. The same key point is brought on in 7.4.3, through a detailed cross-assessment. EGR action is, additionally, less extreme than in benchmark experimental control: this encourages a slower wearing of actuators, as well as providing a wider air mass flow rate region that can be efficiently tracked by the control architecture.

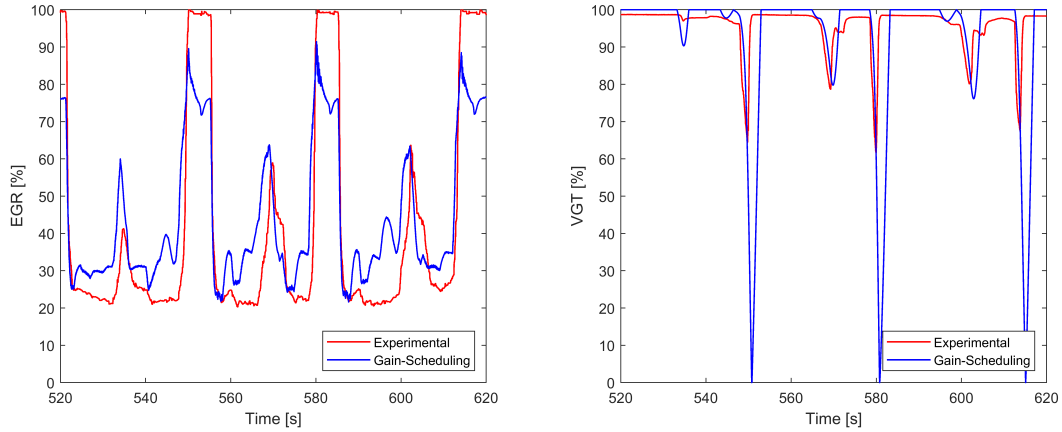


Figure 7.29: EGR control action, to the left, followed by VGT one, to the right. Gain-scheduling controllers are based on whole map affinity mapping and performance is assessed on actuators limits test sequence, for $t = 520 - 620$ s, see 7.18 for reference

7.4.3 Tracking - WHTC test sequence

Tracking performance with control gains spanning over the whole engine map is also represented for the target WHTC engine cycle, as described before. Here, results are given on smaller time spans, being

- from 125 to 150 s;
- from 645 to 675 s;
- from 840 to 920 s;
- from 1620 to 1760 s.

Smaller time intervals are preferred, with a view to providing a sharper look into the compensators performance. Control performance is shown in Figures 7.30 and 7.31.

EGR tracking is satisfying and delay from target signal is noticeably small, being in the order of 0.1 s. Same cannot be said for boost pressure tracking, operated acting on VGT valve. Here, a delay of ca. 0.5 s occurs before variable is tracked, with consequent difficulty in fully tracking target pressure values. In spite of the tracking speed, designed control action is visibly more sensitive to target variations, compared to benchmark control logic. Additionally, tracking is more accurate, remaining closer to the target value, again compared to benchmark.

Figure 7.31 shows an insight on boost pressure tracking: VGT slow dynamics and the usage of controller output filtering, to pursue a realistic actuator behaviour, make the response slower than the EGR valve. An improvement with respect to benchmark control is however visible and a faster tracking is achieved. The delta between reference boost pressure curve and that obtained via gain scheduling is significant, however this is mostly due to physical limitations of the system. VGT actuation, consisting of a rod pulling the inner rim of the turbine stator, is bound to be slow, this is turn causing the visible

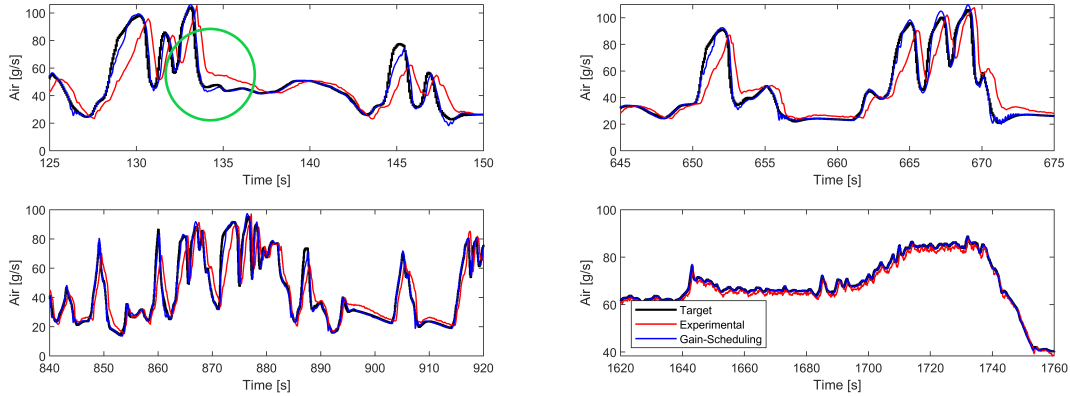


Figure 7.30: Air mass flow rate tracking performance, with EGR and VGT gain-scheduled controllers, on whole map affinity mapping, VGT command is post-filtered, on WHTC test sequence, see 7.18 for reference

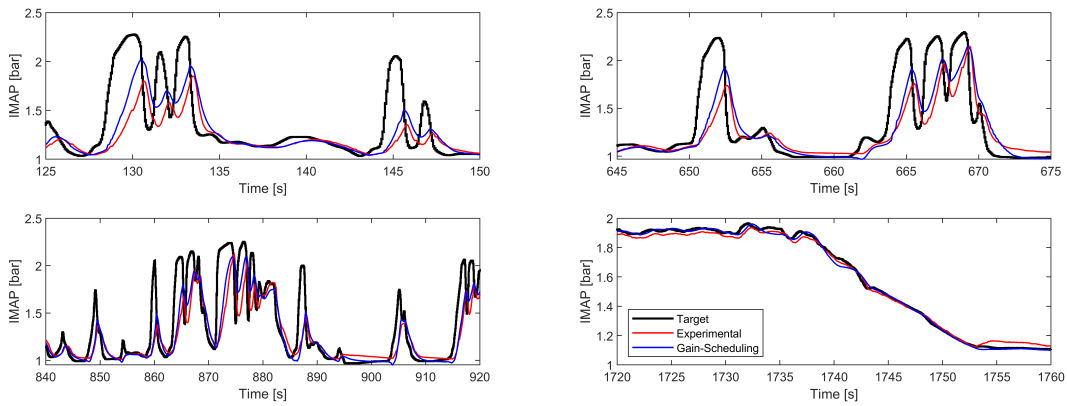


Figure 7.31: Boost pressure tracking performance, with EGR and VGT gain-scheduled controllers, on whole map affinity mapping, VGT command is post-filtered and derivative of injected fuel correction is inserted, on WHTC test sequence, see 7.18 for reference

tracking delay. The mentioned delay decreases when reaching the mildest section of the test sequence, visible in bottom right graph of Figure 7.31; here, tracking is accurate and only marginally lagging with respect to the reference signal, thanks to the smaller oscillations of the *IMAP*.

Graph analysis of Figures 7.32 and 7.33, showing given control action of the two actuators, here reveals a more frequent participation of VGT actuation in the control action. It is crucial to mention that, at fast-varying engine speed and load, VGT valve is not able to physically track the variations, thus being its rod at full actuation for time spans. This is particularly affected by the filter that has been set at the actuation in the control algorithm, to account for the slow actuation dynamics. The issue has been here in part addressed increasing the pass-band frequency of the low pass filter that simulates the

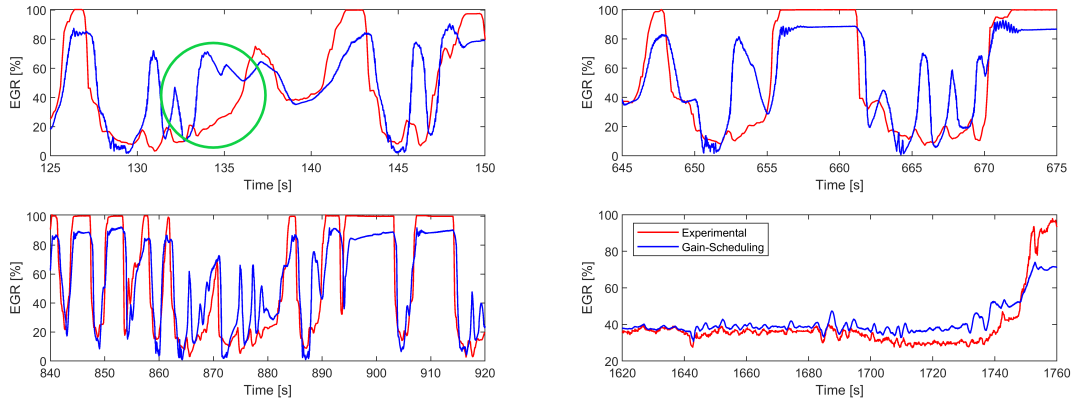


Figure 7.32: EGR valve position command with EGR and VGT gain-scheduled controllers, on whole map affinity mapping, VGT command is filtered and derivative of injected fuel correction is inserted, on WHTC test sequence, see 7.18 for reference

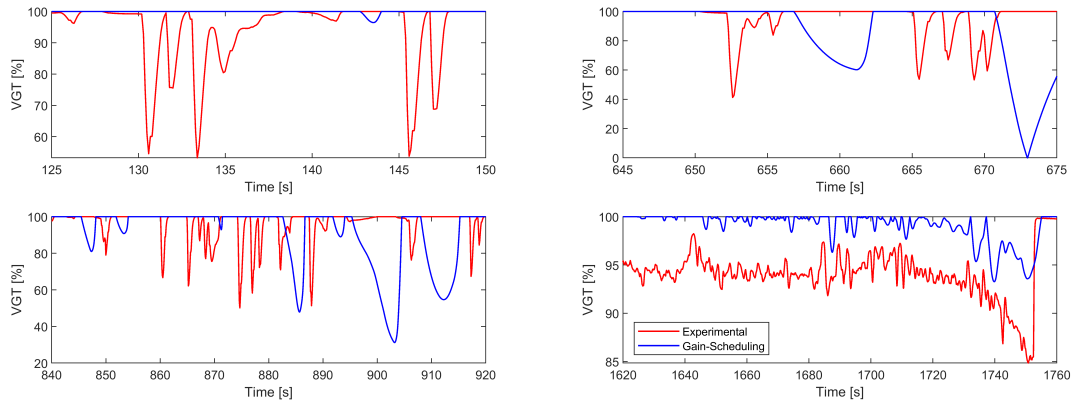


Figure 7.33: VGT rack position command, with EGR and VGT gain-scheduled controllers, on whole map affinity mapping, VGT command is filtered, on WHTC test sequence, see 7.18 for reference

physics of the VGT actuation, though maintaining a value that is reasonable with the physical peculiarities of the actuator. Conversely, Figure 7.32 shows a fully adequate EGR involvement in the control process; to this regard, in time span $t = [134; 135] s$, EGR controller-commanded action is far more consistent with the tracked variable: indeed, no major control action takes place in ECU experimental control. Result of this can be seen in terms of tracking accuracy, that is definitely consistent with the designed controller and far less with test-bank experimental data. The behaviour is emphasized marking the specific time horizons with circles, in Figures 7.32 and 7.30. Both EGR and VGT tracking show a good performance, with the well-known delay in the VGT actuation and a conversely very fast air mass flow rate tracking by the EGR valve, limited only by some particularly fast transient that are not fully caught. No potentially harmful undershoots occur, with the

exception of a spike when crossing from the lead compensator of point 16, to the classical gain-scheduling of the remaining larger part of the map; however mitigated by a bumpless moving average filter, averaging on a 2 s time span, the effect is still felt, due to the high requested integral gain K_I variation, when exiting region n. 16.

The slower tracking of air mass flow rate and boost pressure in low engine speed ($< 1500 \text{ rpm}$) - low $BMEP$ ($< 7.5 \text{ bar}$) areas, as at cycle beginning has to be remarked. This phenomenon is due to the low gain of the control action when inside CEOP n. 16 region and is therefore fully expected. A dedicated figure is not given, being the first simulation instants affected by the need, for the software, to reach the desired reference values starting from an arbitrary initial variables state. Dedicated control technologies should be tailored to better meet this area requirements, that essentially represents an example of *idle management*.

7.5 Results overview and assessment

A thorough evaluation of the obtained control performances and a comparison with the benchmark control directly provided by the engine ECU manufacturer is done, highlighting the tracking improvement that has been achieved via the designed control architecture. Tracking of step and ramp signals is correctly performed, with minor overshoots well within the set control requirements.

On WHTC and most aggressive sequences, tracking delay of designed control solution is noticeably lower than in ECU experimental benchmark and target air mass flow and boost pressure are still duly tracked. Especially in most aggressive situations, designed gain-scheduling control has the upper hand over ECU control, the former being able to reach desired target values more consistently than its competitor. EGR control actions reach saturation less frequently than in ECU controller, however presenting a small actuation ripple in some specific occurrences. VGT control actions are milder than in ECU control, this being a further advantage, as this prevents mechanical wearing of the component.

Controller design and validation has been performed following an iterative and comparative roadmap, that has enriched the range of operativity of the control action, assessing its strength and limitations. Several techniques are compared throughout the design, so as to chose, from time to time, the most adequate one to address each control issue. The final adopted controller consists of three branches, namely the mapped EGR and VGT opening percentages, the correction given by the injected fuel quantity and the PI gain-scheduling controller contribution. The progressive insertion of these three elements gradually improves the control performance, both in terms of response tracking accuracy and in response speed. The two feedforward terms, namely map correction and derivative of injected fuel quantity correction, are essential so that the feedback control action is already based on a non-null input signal; this branches represent the core part of the ECU benchmark control. This decreases the risk of large overshoots or ripples in the control action, enhancing the overall tracking performance of the architecture. *Affinity mapping* has been chosen as reference to set the proportional and integral gains K_P and K_I of both

the actuation systems controllers. Choice has been made considering the slightly improved target tracking with respect to *vicinity mapping*.

In-depth analyses are brought on for what concerns the topics of anti-windup mechanisms, CEOPs recognition and engine mapping. Chosen anti-windup mechanism is that of *conditional integration*, ensuring a fast zeroing of the integrator block and well-suited for the PI gain-scheduling controller, as it is based on an integral component, independently of the engine state.

Some research areas are still to be enlightened, namely the performance assessment of the control logics when relying on *k-means clustering mapping*, as well as the insertion of median-averaged CEOPs to attain a better-fitting controller model for each engine state. These further studies leave room for successive future developments and exploration of the work.

Conclusions

The chapter concludes the comprehensive exploration of identification and control techniques and methodologies aimed at the improvement of a benchmark control logic. A cohesive summary of the key findings, insights and contributions presented throughout the previous chapters is provided. Along with this, the main research questions and hypotheses are revisited, focusing on how the study has addressed them.

The introductory Chapter 1 defines what the aim of the dissertation is, within the identification and control theory framework: the enhancement of the performance obtained by benchmark EGR and VGT controllers, equipped on a four cylinders, 2998 cc diesel engine. This is performed by entirely re-designing the control architecture of the two actuation systems, from the mathematical models upon which control logic is based, to the actual control scheme and its directly related subsystems.

In Chapter 2, studied engine model from which the testing is derived is presented. Engine specifications and behaviour are illustrated and a detailed airpath description is provided. Chapter is closed presenting the simulation computerised environment, GT-Power, whereon experiments are run.

Chapter 3 is propedeutic to the development of the core dissertation matter. The chapter introduces the concept of engine *mapping* and aims at dividing the non-linear engine operating range in subregions, where the valve actuators behaviour is approximated as linear. For each subregion, a specific control logic is going to be tailored. Three different *mapping* procedures are presented; among these, *affinity mapping* and *k-means clustering* follow a nonstandard development technique. Outcome of this is positive and is presented in the successive chapters.

The identification process, by which different model families are identified for each engine map subregions, is carried on in Chapter 4. Considered model families are ARX, ARMAX, OE and state-space. Key performance indicators are extracted, state-space models family being eventually chosen, as the most descriptive and flexible for the target issue.

In Chapter 5 the matter is brought on. In the first part of the chapter, screening of a given number of models, one per each engine area, is performed and discussed; a direct model selection approach and an averaging technique are investigated for this scope and

eventually the former is preferred. Once the control models are chosen, a prototype controller based on a *single* state-space model is designed; intermediate results are presented. PI controllers with actuation signal post-filtering are chosen for this stage: obtained compensators are then compared with controller relying only on mapped data.

The need for an effective anti-windup system, avoiding the actuators remaining stuck in a saturation position for too long a time is reflected in Chapter 6. Here, several anti-windup architectures are outlined and their performance is compared. Ultimate aim of the chapter is the application of the most adequate anti-windup scheme to the airpath actuators control. Integral anti-windup has demonstrated to have the best performance, in terms of response speed and accuracy.

Final Chapter, 7, presents the gain scheduling controller. Following a gradual procedure, first a gain scheduling control based on four control engine operating points is designed and tested. Bumpless filters are applied to smooth switching between control gains. Then, a whole-map spanning gain scheduling control system is developed and results are validated on test engine cycles, including a World Harmonized Transient Cycle. Control performance is further enhanced enriching the architecture with an additional branch, yielding the contribution of the derivative of the fuel injected quantity. The insertion of this further block allows for a faster and more accurate target tracking and gives consistent results especially in case of long ramps on mass air flow rate or boost pressure. The comparison between the obtained tracking performance and that of the set benchmark controller, namely the one implemented in the ECU by the engine manufacturer, yields satisfying results, as output target tracking is both faster and more accurate, in terms of steady state tracking. Tracking of steepest transients is neatly improved and overall response is not affected by chattering.

Bibliography

- [1] S.A. Malan, L. Ventura, *A Systematic Procedure for Engine Air-Path Identification*, International Journal of Mechanics and Control, Turin, Italy, 2020
- [2] L. Ventura, R. Finesso, S.A. Malan, R. d'Ambrosio, A. Manelli, *Model-based design of closed loop controllers of the air-path in a heavy duty diesel engine*, AIP Conference Proceedings 2191, Turin, Italy, 2019
- [3] T. Alger, J. Gingrich, I. Khalek, B. Mangold, *The Role of EGR in PM Emissions from Gasoline Engines*, SAE Int. J. Fuels Lubr., pp. 85-98, 2010
- [4] A. G. Stefanopoulou, I. Kolmanovsky, J. S. Freudenberg, *Control of variable geometry turbocharged diesel engines for reduced emissions*, IEEE Transactions on Control Systems Technology, vol. 8, no. 4, pp. 733-745, July, 2000
- [5] A. Ulsoy, H. Peng, M. Çakmakci, *Automotive control systems*, Cambridge University Press, 2012
- [6] A' Bárdos, H. Neimeth, *Control oriented air path model for compressed air boosted Diesel engines*, Periodica Polytechnica, Budapest, Hungary, 2012
- [7] Seungwoo H., Inseok P., Jaesung C., Myoungcho S., *Gain Scheduled Controller of EGR and VGT Systems with a Model-Based Gain Scheduling Strategy for Diesel Engines*, International Federation of Automatic Control, Elsevier, Seoul, 2015
- [8] M. Jankovic, M. Jankovic, I. Kolmanovsky, *Constructive Lyapunov Control Design for Turbocharged Diesel Engines*, IEEE Transactions on Control Systems Technology, vol. 8, n. 2, March, 2000
- [9] Lianhao Y., G. Turesson, P. Tunestal, R. Johansson, *Model Predictive Control of an Advanced Multiple Cylinder Engine With Partially Premixed Combustion Concept*, IEEE/ASME Transactions on Mechatronics, vol. XXV, n. 2, April, 2020
- [10] Hui X., Kang S., Sheng Y., J. Tatsumi, Qinling Z., Han Z., Zhiqiang G., *On Decoupling Control of the VGT-EGR System in Diesel Engines: A New Framework*, IEEE Transactions on Control Systems Technology, vol. XXIV, n. 5, September, 2016
- [11] Tianpu D., Fujun Z., Bolan L., Xiaohui A., *Model-Based State Feedback Controller Design for a Turbocharged Diesel Engine with an EGR System*, Energies Journal, May, 2015
- [12] Oh, B., Lee, M., Park, Y., Sohn, J., Won, J. and Sunwoo, M., *VGT and EGR Control of Common-Rail Diesel Engines Using an Artificial Neural Network*, ASME. J. Eng. Gas Turbines Power. January, 2013
- [13] T. Soderstrom, *On model structure testing in system identification*, International Journal of Control, vol. 26, no. 1, 1977
- [14] *System analysis of a diesel engine with VGT and EGR*, Linköping University Post

- Print, October, 2005
- [15] T. Zeng, G. G. Zhu, *Control-oriented turbine power model for a variable-geometry turbocharger*, Journal of Automobile Engineering, 2018
 - [16] K. Nikzadfar, A. H. Shamekhi, *Developing a state space model for a turbocharged diesel engine using the subspace identification method*, Proceedings of the Institution of Mechanical Engineers, Part D, Journal of Automobile Engineering, 2011
 - [17] J. Wahlström, L. Eriksson, *Modeling of a Diesel Engine with VGT and EGR including Oxygen Mass Fraction*, Linköping University Post Print, Department of Electrical Engineering, 2006
 - [18] J. Wahlström, L. Eriksson, *Modelling diesel engines with a variable geometry turbocharger and exhaust gas recirculation by optimization of model parameters for capturing non-linear system dynamics*, Linköping University Post Print, Department of Electrical Engineering, 2011
 - [19] H. Andersson, M. Hedvall, *Model Based Control of Air and EGR into a Diesel Engine*, Department of Signals and Systems, Division of Automatic Control, Automation and Mechatronics, Chalmers University of Technology, 2008
 - [20] R. V. Koli, *Model Predictive Control of Modern High Degree-of-Freedom Turbocharged Spark Ignited Engines with External Cooled EGR*, All Dissertations. 2211, 2018
 - [21] Sun H., *Design and Simulation of Engine Control System*, Politecnico di Torino, 2018
 - [22] M. U. Yavas, *Model Predictive Control of a Turbocharged Diesel Engine with Exhaust Gas Recirculation*, Istanbul Technical University, Department of Control and Automation, January, 2015
 - [23] D. Liao-McPherson, M. Huang, Shinhoon K., Masanori S., K. Butts, I. Kolmanovsky, *Model predictive emissions control of a diesel engine airpath: Design and experimental evaluation*, International Journal of Robust and Nonlinear Control, September, 2020
 - [24] S. Di Cairano, I. Kolmanovsky, *Automotive Applications of Model Predictive Control*, Mitsubishi Electric Research Laboratories, Cambridge, Massachusetts, December, 2019
 - [25] M. Karlsson, K. Ekholm, P. Strandh, R. Johansson, P. Tunestål, *Multiple-Input Multiple-Output Model Predictive Control of a Diesel Engine*, IFAC Proceedings Volumes, Volume 43, Issue 7, 2010
 - [26] L. Guzzella, A. Amstutz, *Control of diesel engines*, IEEE Control Systems Magazine, vol. 18, no. 5, pp. 53-71, October, 1998
 - [27] J. Zhou, L. Fiorentini, M. Canova, Y. -Y. Wang, *Coordinated Performance Optimization of a Variable Geometry Compressor With Model Predictive Control for a Turbocharged Diesel Engine*, IEEE Transactions on Control Systems Technology, vol. 24, no. 3, pp. 804-816, May, 2016
 - [28] J.D. Powell, *A Review of IC Engine Models for Control system Design*, IFAC Proceedings Volumes, vol. 20, is. 5, p. 3, pp. 235-240, 1987
 - [29] Peng Q., Huo D., Hall CM., *Neural Network-based Air Handling Control for Modern Diesel Engines*, Proceedings of the Institution of Mechanical Engineers, Part D: Journal of Automobile Engineering, vol. 237, no. 5, pp. 1113-1130, 2023
 - [30] L. Ventura, *Development and assessment of model-based and sensor-based algorithms for combustion and emission control in diesel engines*, Politecnico di Torino, pp. 1-149, September 2022

-
- [31] Lennart Ljung *System Identification - Theory For the User*, Appendix 4A, pp 132-134, 2nd ed, PTR Prentice Hall, Upper Saddle River, N.J., 1999
- [32] G. E. P. Box, G. M. Jenkins, *Time Series Analysis: Forecasting and Control*, Holden-Day, 1979
- [33] S. Bittanti, *Teoria della Predizione e del Filtraggio*, Pitagora, 2000
- [34] M. Taragna, *Estimation, Filtering and System Identification*, Polytechnic University of Turin, 2022
- [35] K. J. Åström, L. Rundqwist, *Integrator windup and how to avoid it*, 1989 American Control Conference, 1989
- [36] K. J. Åström, T. Hägglund, *Advanced PID Control*, International Society of Automation, Triangle Park, NC, 2006
- [37] P. Bolzern, R. Scattolini, N. Schiavoni, *Fondamenti di controlli automatici*, Mc Graw-Hill, 2008
- [38] A. Pisano, *PID regulators*, p.45, University of Cagliari, Cagliari, 2022
- [39] *MISRA C:2012 Amendment 2*, , Updates for ISO/IEC 9899:2011 Core functionality February 2020
- [40] Y. Shi and X. -M. Sun, *Bumpless Transfer Control for Switched Linear Systems and its Application to Aero-Engines*, IEEE Transactions on Circuits and Systems I: Regular Papers, vol. 68, no. 5, pp. 2171-2182, May 2021
- [41] S. -Y. Cheong, M. G. Safonov, *Bumpless Transfer for Adaptive Switching Controls*, IFAC Proceedings Volumes, vol. 41, iss. 2, pp. 14415-14420, 2008
- [42] J. J. Slotine, W. Li., *Applied Nonlinear Control*, Prentice Hall, 1991
- [43] W. J. Rugh, J. S. Shamma, *Research on Gain Scheduling*, Automatica, vol. 36, pp. 1401-1425, 2000
- [44] D. J. Leith, W. E. Leithead, *Survey of gain-scheduling analysis and design*, International journal of control, vol. 73, iss. 11, pp. 1001-1025, 2000
- [45] *World Harmonized Transient Cycle (WHTC)*, DieselNet, 2007, <https://dieselnet.com/standards/cycles/whtc.php>
- [46] UNECE-WP.29 GRPE, WHDC Working Group, *Worldwide Harmonized Heavy Duty Emissions Certification Procedure*, GRPE 50th session, June 2005
- [47] ECE-GRPE, WHDC Working Group, H. Steven, *Development of a Worldwide Harmonised Heavy-duty Engine Emissions Test Cycle* , GRPE 42th session, April 2001